Numerical and Experimental Investigations of Boersch Phase Plate equipped Condenser Apertures for Use in Electron Magnetic Circular Dichroism Experiments in a Transmission Electron Microscope

Dissertation zur Erlangung des Doktorgrades
der Naturwissenschaften (Dr. rer. nat.)
der Fakultät Physik
der Universität Regensburg

vorgelegt von
Andreas Pritschet
(geb. Hasenkopf)
aus Lappersdorf

Juni 2013

Promotionsgesuch eingereicht am:	25.06.2013
Die Arbeit wurde angeleitet von:	Prof. Dr. J. Zweck
Prüfungsausschuß:	Prof. Dr. T. Wettig Prof. Dr. J. Zweck Prof. Dr. F. Gießibl Prof. Dr. Ch. Strunk

Results? Why, man, I have gotten lots of results! If I find 10,000 ways something won't work, I haven't failed. I am not discouraged, because every wrong attempt discarded is often a step forward....

– Thomas A. Edison (1847 – 1931)

List of Abbreviations

Abbreviation	Full expression
ASCII	American Standard Code for Information Interchange
BFP	Back Focal Plane
CAD	Computer Aided Design software
CAIBE	Chemically Assisted Ion Beam Etching
CBED	Convergent-Beam Electron Diffraction
CCD	Charge-Coupled Device
DPC	Differential Phase Contrast
EBL	Electron Beam Lithography
EDX	Energy Dispersive X-ray spectroscopy
EELS	Electron Energy-Loss Spectroscopy
EFTEM	Energy-Filtered Transmission Electron Microscopy
EMCD	Electron Magnetic Circular Dichroism
(F)EBID	(Focused) Electron Beam Induced Deposition
(F)EBIE	(Focused) Electron Beam Induced Etching
FEG	Field Emission Gun
FEM	Finite Element Method
FFP	Front Focal Plane
FIB	Focused Ion Beam
FWHM	Full Width at Half Maximum
HWHM	Half Width at Half Maximum
LM-STEM	Low Magnification STEM
MC	Mini Condenser lens
OAM	Orbital Angular Momentum
PCB	Printed Circuit Board
PCM	Phase Contrast Microscopy
PDE	Partial Differential Equation
PECVD	Plasma-Enhanced Chemical Vapor Deposition
ROI	Region Of Interest
SDD	Silicon Drift Detector
SEM	Scanning Electron Microscope
SNR	Signal to Noise Ratio
STEM	Scanning Transmission Electron Microscope
TEM	Transmission Electron Microscope
XMCD	X-ray Magnetic Circular Dichroism

Contents

1. Introduction **1**

2. Electron Magnetic Chiral Dichroism **2**
2.1. Magnetic Circular Dichroism 2
2.2. The Techniques 3
2.2.1. Intrinsic 3
2.2.2. Vortex Beam 5
2.2.3. Twin Aperture 6

3. Phase Plates **9**
3.1. State of the Technology 9
3.1.1. Thin Film Phase Plates 10
3.1.2. Obstacle-free Phase Plates 10
3.1.3. Application 11
3.2. Design Adaptations 13

4. Finite Element Method Calculations **16**
4.1. Fundamentals of the Finite Element Method 16
4.1.1. Principle 16
4.1.2. Tessellation 16
4.1.3. Numerical solution 18
4.2. Solving Laplace's equation 21
4.3. Modelling Phase Shift 23
4.3.1. Electron Optical Background 23
4.3.2. Boersch Phase Plate 25
4.3.3. Twin Aperture 29
4.3.4. Twin Aperture Variations 32
4.4. Summary 37

5. Electron optical numerical calculations **38**
5.1. Fundamentals of Electron Optics 38
5.2. Wave Function of Electron Probe in Scanning Mode 40
5.2.1. First Approximation — Constant Phase Shift 43
5.2.2. Second Approximation — Hyperbolic Cosine 45
5.3. Electron Penetration Depth 58
5.4. Dynamical Diffraction Simulations 60
5.5. Summary 65

6. Experimental setup **66**
6.1. Microscope & Equipment . . . 66
6.1.1. Microscope . . . 66
6.1.2. Energy Filter . . . 66
6.1.3. Energy-dispersive X-ray Spectroscope . . . 68
6.1.4. DPC Detector . . . 69
6.1.5. Shadow Image . . . 70
6.2. Manufacturing of Twin Aperture . . . 73
6.2.1. Substrate: Commercial Si_3N_4 Membrane . . . 73
6.2.2. Substrate: Commercial Pt Foil . . . 75
6.3. Manufacturing of Customized C2 Aperture Holder . . . 76

7. Experiments **79**
7.1. Convergence Angle . . . 79
7.2. Thin Twin Aperture . . . 82
7.2.1. Differential Phase Contrast Measurements . . . 82
7.2.2. Resistance Measurements . . . 86
7.3. Energy Dispersive X-Ray Investigations . . . 88
7.4. Spot Size Analysis . . . 93
7.4.1. Acquisition with CCD Camera . . . 93
7.4.2. Acquisition of Contamination Spots . . . 97
7.5. Summary . . . 101

8. Conclusion **103**

A. Appendix **104**
A.1. Aperture Holder Schematics . . . 104
A.2. Software . . . 106
A.3. FEM Results . . . 106
A.4. Electron Optical Numerical Calculations . . . 108
A.5. Dynamical Diffraction Simulations by J. Rusz . . . 112
A.6. DPC Measurements . . . 113
A.7. EDX Mappings . . . 114
A.8. Focal Series . . . 115
A.9. Theory of Aberrations . . . 121

Publications **122**

Bibliography **123**

Acknowledgment **138**

1. Introduction

For more than 10 years material scientists have been trying to establish new techniques that allow the investigation of magnetic samples in a transmission electron microscope by means of an effect called *electron magnetic chiral dichroism*[1]. So far the established technique has high demands on the skills of the microscope operator and the sample quality. Thus the technique has only been applied in a few investigations of magnetic compounds[2] and biological[3] specimens.

Despite advances in the development of electron vortex beams[4] for such investigations in recent years the subject of this thesis is to utilize electron optical elements — namely phase plates — known from life sciences in a new way to reduce the difficulties in the execution of electron magnetic chiral dichroism measurements. Thus the focus of this work lies in the theoretical and experimental investigation of the optical properties of electrostatic phase plates[5] for the usage in a different experimental setup.

We will start out with an overview of the techniques for measuring electron magnetic chiral dichroism in Chapter 2 and introduce a setup comprising phase plates to ease measurements. Chapter 3 gives an introduction to different phase plate designs and their working principles. Furthermore design adaptations to phase plates for use in electron magnetic chiral dichroism experiments are introduced.

Chapters 4 and 5 are the theoretical parts of this work. First the phase shifting behavior of the newly suggested aperture design including phase plates is investigated. Based on these results the electron probe formed by such a device in the specimen plane and the dichroic signal that are to be expected in such a setup are investigated.

After description of the experimental setup and techniques in Chapter 6 the theoretical predictions regarding the electron probe of Chapter 5 are to be evaluated experimentally in Chapter 7. Hereby a highlight is given to deficiencies of the new aperture device due to issues during the fabrication process.

2. Electron Magnetic Chiral Dichroism

Electron magnetic circular dichroism[6] (EMCD) is an analogue of the x-ray magnetic circular dichroism (XMCD). To emphasize the principal difference between the techniques — e.g. the electrons are not required to be polarized[a] — EMCD is also referred to as *electron magnetic chiral dichroism*. The main issue in the initial development of the EMCD technique was thought to be the requirement of spin polarized electrons, which turned out to be not necessary. Instead of photons of different polarization helicities the effect embodying electrons relies on different momentum transfer vectors as will be explained in more detail in Sec. 2.2.1.

Both methods are based on the excitation of a core electron into unoccupied valence states, therefore both EMCD and XMCD allow element-selective investigations of magnetic properties. Contrary to the x-ray case, EMCD is done using a transmission electron microscope, which allows a small electron optical resolution (sub-Ångström range).[7]

Since the discovery of EMCD[6,8], there were substantial improvements in spatial resolution[9–11], advances in theoretical understanding[12–17], first quantitative measurements[15,18–20] and even early applications[3,21–25]. Nevertheless, EMCD measurements remain tedious due to high demands on sample quality and a low signal to noise ratio (SNR).

While the SNR issue is subject to research of theoretical physicists[26,27] this work will present an overview of established and currently investigated techniques (see Sec. 2.2), which intend to overcome the experimental requirements to the specimen; thereby the focus will be put on the method investigated in this work, namely the *twin aperture with Boersch phase plates* (see Sec. 2.2.3).

In the following an overview of EMCD techniques will be given. As the main focus of this work does not lie within the EMCD framework an in-depth treatment of the effect will not be given. The interested reader may consult Ref. [28] for a detailed approach and treatment of the EMCD effect. After a brief description of the established EMCD techniques we will propose a new setup for measuring EMCD effects based on a twin aperture.

2.1. Magnetic Circular Dichroism

In the field of light optics, there are a series of magneto-optic effects in which the way an electromagnetic wave is transmitted or reflected by a magnetic sample is altered. The most prominent of these effects are the Faraday effect and the magneto-optic Kerr effect[29,30]. The latter describes the changes to light reflected from a magnetized surface (in transmission this is referred to as Faraday effect); the polarization direction of linearly polarized light becomes rotated during reflection depending on the orientation of the wave vector relative to the magnetic

[a] Experiments with spin polarized electrons have not been reported, yet.

field. The magneto-optic Kerr effect is commonly used in material science to investigate the magnetization structure of materials.

Working with circularly polarized light one can encounter magnetic circular dichroism — the differential absorption of left and right circularly polarized light, induced in a sample by a strong magnetic field. Looking at a ferromagnetic 3d transition metal sample — e.g. Fe, Ni or Co — the transition of an electron from a 2p to a 3d orbital shows the strongest dichroic signal[31]. According to quantum mechanics[32] the transition 2p $\rightarrow$ 3d has to fulfill the selection rule $\Delta m = \pm 1$ as the absorption of a circularly polarized photon, whose helicity is parallel to the magnetization, transfers an angular momentum to the electron.

Due to the Zeeman splitting[32] the 2p states and the 3d band are split depending on the allowed m values, e.g. $2p \rightarrow 2p_{1/2} + 2p_{3/2}$; in other words the degeneracy of the nl state is lifted[8]. The observation of different transition probabilities in the dichroic signal is basically defined by the energy differences between these split states[33].

2.2. The Techniques

In order to observe a dichroic signal in a transmission electron microscope primary electrons inelastically scattered at 2p electrons have to perform a similar momentum transfer as did photons in the previous case. So far two different groups of techniques have emerged that intend to supply such a momentum transfer.

These two groups are in principle defined by the different source for the momentum transfer; in the first case a change in the primary electron's momentum is transferred while in the latter an orbital angular momentum carried by the primary electron is transferred to a 2p electron.

In the following we will give a short overview of those two different approaches: the *intrinsic method* and the *vortex beam method*. Based on the intrinsic method we will propose a new setup comprising a twin aperture.

2.2.1. Intrinsic

The established technique is called the *intrinsic method*, which was proposed in 2003[1] and has been subject to further developments[9–17]. This technique is inspired by a formal analogy[1,8,31,34] between the absorption cross section in X-ray absorption spectrometry[1,8,31] and the double differential scattering cross section in inelastic electron scattering[1,8,35] according to which the momentum transfer $\hbar\vec{q}$ in inelastic scattering of a fast electron leads to a dichroic signal just like the polarization $\vec{\epsilon}$ of an absorbed photon.

A circular polarization of a photon can be written as a superposition of two linear polarizations with a phase difference between those two of $\pm\pi/2$ — depending on the helicity that is to be described. Following the analogy the momentum transfer required for EMCD is considered — like a circular polarization — as a superposition of two orthogonal (linear) momentum transfers ($\vec{q}_1$ and $\vec{q}_2$ in Fig. 2.1) with a phase difference of $\pm\pi/2$. As these momentum transfers affect electrons of different beams the phase difference is required between those beams.

In practice these two coherent waves are the unscattered beam and a scattered Bragg beam (red circles in Figs. 2.1 and 2.3), commonly referred to as $\vec{0}$ and $\vec{G}$, where $\vec{G}$ is a low order Bragg beam, e.g. 110[20,36]. Due to dynamical diffraction effects the phase difference of $\pi/2$ can be

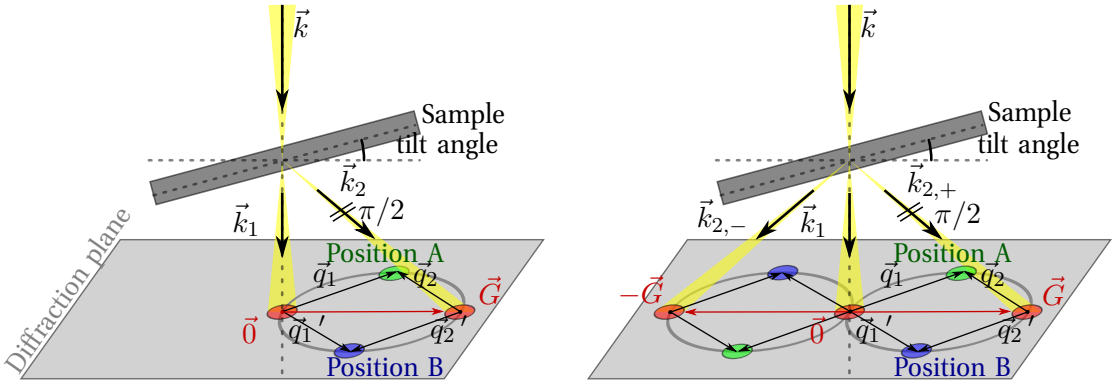

Figure 2.1.: Schematic setup for the intrinsic method — two beam case (left), three beam case (right). By dotted lines the optical axis and sample tilt are indicated. For sake of simplicity a convergent beam is assumed in the figure. By tilting the specimen the intensity in the diffraction pattern is tuned such that two (or three; right) Bragg beams (red dots) $\vec{k}_1 = \vec{k}_{\text{II}} + \vec{0}$ and $\vec{k}_{2,\pm} = \vec{k}_{\text{II}} \pm \vec{G}$ ($\pm\vec{G} \perp \vec{k}$, $\vec{k}_{\text{II}}$) are strongly excited, where $\vec{k}$ is the wave vector of the incident wave, $\vec{k}_{\text{II}}$ is the component of the wave vector parallel to the optical axis after scattering and the component perpendicular to the optical axis $\vec{G}$ is determined by the corresponding Bragg spot. By means of dynamic diffraction effects and a suitable sample thickness a phase difference between the beams of $\pi/2$ is introduced. The orthogonal superposition of two momentum transfers $\vec{q}_1 + \vec{q}_2$ leads to the definition of two measurement positions **A** (green circle) and **B** (blue circle) on a Thales circle. Annotations have been omitted on the left hand side of the three beam case illustration.

adjusted by choosing a suitable sample thickness and sample tilt[8,33,35,37]. As the Bragg angles are determined by the atomic lattice the phase difference is adjusted at all atomic positions such that all atoms will contribute to the EMCD signal with the same sign, if the diffraction condition is chosen correctly.

These diffraction conditions are two strongly excited Bragg spots, while the remaining spots in the diffraction pattern are suppressed; this is referred to as *2 beam case*[6,8,33]. Alternatively a *3 beam case*[3,33,38] can be excited, where the unscattered beam is accompanied by two scattered beams (see Fig. 2.1).

Having met the diffraction condition for the *2 beam case* one defines a Thales circle with diameter equal to the distance $|\vec{G}|$ between the Bragg spots. Following the analogy of a circularly polarized wave one can identify two specific points **A** and **B** (see green and blue circle in Fig. 2.1 and 2.3) on this Thales circle, which fulfill the conditions $\vec{q}_1 \perp \vec{q}_2$, $|\vec{q}_1| = |\vec{q}_2|$. The obtainable dichroic signal is proportional to — among other parameters — the vector product of the momentum transfers at these points[10,13,39]. Due to the different sign of the vector product at the positions **A** and **B** the superpositions of the momentum transfers at these points are equivalent to the desired opposite helicities — indicated by differently colored spots for positions **A** and **B**. The difference of electron energy-loss spectra acquired at these points yields the desired dichroic signal.

Working in the 3 beam case one can define two Thales circles due to symmetry reasons[33] as shown on the right hand side of Fig. 2.1. This allows for the acquisition of two pairs of spectra. Alternatively to acquiring single spectra one can acquire energy filtered diffraction patterns[33]. In combination with a 3 beam case these energy filtered diffraction patterns allow the extraction of real space maps[3,9,40,41] of the dichroic signal and treatment with sophisticated noise reduction algorithms[26,27].

A downside of the intrinsic method are the requirements for dynamical diffraction, which is known to modulate the intensity of diffraction spots in a TEM[42]. Dynamical diffraction calculations[8,12,31] conducted by Jan Rusz showed what influence dynamical diffraction effects have on the achievable dichroic signal. From these calculations it was concluded that one needed to accurately tilt a crystalline sample of the correct thickness, which is material specific, in order to obtain a phase difference of $\pi/2$ between the excited beams. Therefore we introduce a new setup in Sec. 2.2.3 with the aim to overcome these requirements.

2.2.2. Vortex Beam

A different approach to EMCD experiments has emerged thanks to the recently discovered possibility of free electrons to carry an orbital angular momentum[4,43] (OAM). Like the discovery of the intrinsic EMCD effect itself this was inspired by an analogy; in this case to optical vortex beams[44,45] carrying an OAM[46]. These vortex beams are mathematically described by Laguerre-Gaussian beams, which are solutions of the Helmholtz equation describing the propagation of light as well as of the Schrödinger equation describing the evolution of free-particle wave functions[47].

For the generation of electron vortex beams two different techniques — graphene based phase plates with helical thickness profile[43] and a binary mask aperture[4] — have been suggested. The latter should be the most promising technique as thin film phase plates can suffer serious problems (compare to Secs. 3.1 and 7.2). The structure for the binary mask was derived by Verbeeck et al. from an intensity distribution resulting from a superposition of a tilted plane wave with a vortex beam with OAM $l\hbar$[4,48,49]; due to this approach the mask is occasionally also referred to as holographic binary mask. Fig. 2.2 shows on its right hand side the proposed structure of the binary mask that was milled into a thin Pt foil by means of focused ion beam milling. As a binary mask cannot resemble a continuous intensity distribution the binary mask will generate more than one order of vortex beams.

When an electron beam is diffracted by such a holographic binary mask it obtains a singularity in the phase front at the center of the beam; this singularity is handled by interference effects that cause the intensity to vanish at this point. Thus a vortex of twisted beams spiraling around this node is created[50].

In EMCD experiments using vortex beams the magnetic sample is simply considered as a *chiral filter*[4]. As we have seen in Sec. 2.2.1 EMCD is an effect observed in inelastic scattering. Regarding a generalized reciprocity theorem[51] one finds that the order of a *polarizer* — here the binary mask — and sample can be interchanged[4,48] when regarding inelastic scattering. Thus the vortex beam method allows for two distinctive setups.

The binary mask can be inserted in front of a condenser aperture[49] (polarizer in front of sample) allowing the use of vortex beams with a selected OAM in STEM, where the condenser

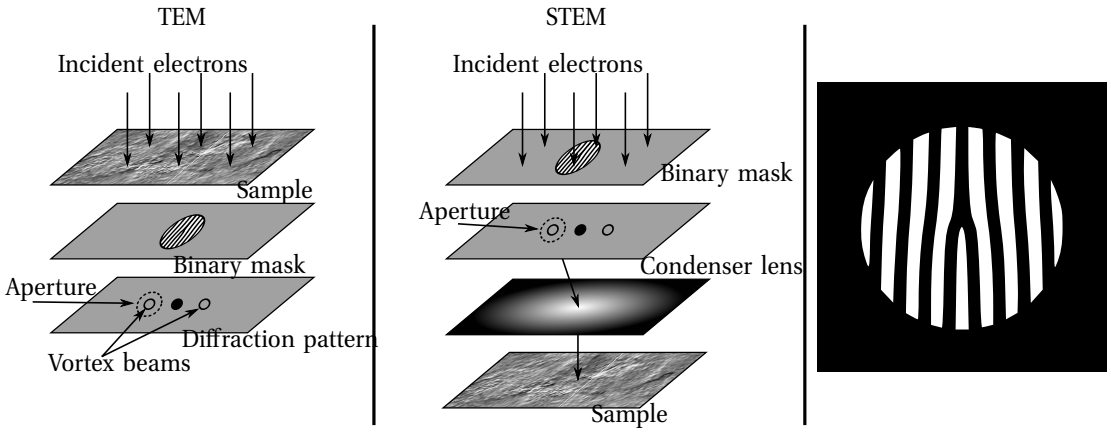

Figure 2.2.: Simplified schematics of microscope setups using a binary mask aperture for TEM (left) and STEM (center) mode. On the right hand side the pattern of the binary "fork" mask (black parts are not transparent) is shown. Reconstruction from Ref. [48].

aperture is used to select one vortex beam (sketch in the center of Fig. 2.2). Alternatively it is inserted into a plane behind the sample[4] allowing usage as an analyzer in TEM diffraction mode (sketch on the left hand side of Fig. 2.2), where the spectrometer entrance aperture would be used to select a vortex beam.

2.2.3. Twin Aperture

The method described in Sec. 2.2.1 utilizes a crystalline sample as a beam splitter that imposes by means of dynamic diffraction effects a phase difference between Bragg beams, which is dominated by phase jumps due to scattering and path length difference. The new setup investigated in this thesis assumes the principles of the intrinsic method but is designed to achieve a phase shift with other means — namely a new condenser aperture design equipped with electrostatic Boersch phase plates. The new aperture design contains two aperture holes and will be referred to as *twin aperture* in this work. By means of the Boersch phase plates one of the waves travelling through the aperture plane is to be shifted in phase.

Even if the intrinsic method was initially developed for use with a "parallel" beam it was shown in Ref. [10] that a dichroic signal is recordable for a strongly convergent beam as well. To emphasize the similarities of the two methods in a schematic comparison we will assume the convergent beam to be focused into the sample plan. Fig. 2.3 shows schematic setups for the intrinsic method (compare Sec. 2.2.1 and Fig. 2.1) using a default condenser aperture (left) and our suggested twin aperture (right; phase plates are indicated by red filled rectangles with black contour). In both cases the beam is focused into the sample plane, where the wave function of the focused beam is described by an Airy disk or a superposition thereof, respectively.

On the left hand side the optical axis has been tilted in order to allow a better comparison of the techniques. In the intrinsic setup the incoming beam (along the optical axis) hits the tilted sample[18] in which dynamical diffraction effects impose a phase shift of $\pi/2$ on scattered Bragg beams. Choosing the right tilt angle relative to the propagation direction of the beam $2-3$

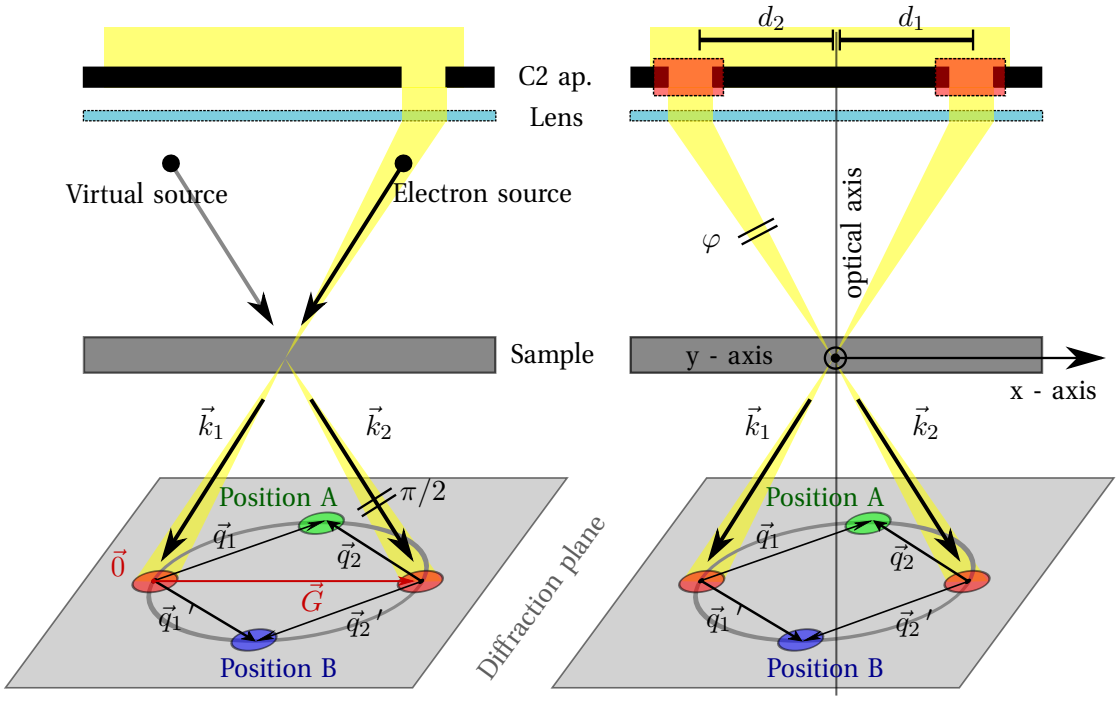

Figure 2.3.: Schematic setup for an intrinsic EMCD experiment (left, compare to Fig. 2.1) and for an EMCD experiment using a twin aperture with Boersch phase plate (right). While in the intrinsic method the phase shift ($\pi/2$) is obtained by orientation and thickness dependent dynamic diffraction effects our goal is to apply a phase shift $\varphi = \pi/2$ by a phase plate to overcome those restrictions. The z-axis points downward the optical axis of the system, the x-axis lies in the paper plane and points to the right, the y-axis points out of the paper plane.

Bragg spots become primly excited in the diffraction pattern.

Our goal is a setup that provides the required beam properties before the beam is passing through the sample by means of a phase plate shifting one wave in phase by $\varphi = \pi/2$. This is realized by application of an electrostatic potential to the Boersch phase plate[52]. A second phase plate around the second aperture remains on a grounded potential to make sure that the phase of the wave traveling through this aperture is not shifted. Thus we hope to reduce the dependence of the dichroic signal on dynamic diffraction effects, which were utilized in the intrinsic method to generate the phase shift.

In Chap. 5 we will calculate the effects of two apertures and a phase shift φ on the wave function of the electron probe in the sample plane. Having set the required wave properties the beam electrons should be able to interact with the sample and produce an EMCD signal presumably independent of the dynamical diffraction effects. The actual dependence of the signal on dynamical diffraction effects will be investigated in Sec. 5.4. The two transmitted beams in this new setup are treated like the Bragg spots in the intrinsic method.

A practical issue that might arise in the use of a twin aperture for EMCD experiments is the

fact that the incidence angles of the two beams are now defined by the twin aperture geometry and condenser focal length of the microscope and not by the lattice of the sample. This might lead to unfavorable conditions, e.g. the interference pattern due to the superposition of two incident waves could form different regions[b] on the specimen, which contribute with different signs to the EMCD signal, if the periodicity of the phase difference differs too much from the periodicity of the lattice. This could result in a strong reduction of the achievable dichroic signal or in the worst case in mutual annihilation of contributions and lack of a dichroic signal at all.

[b] or even neighboring atoms, if one would use a double-corrected TEM.

3. Phase Plates

In light optics a wave plate, retarder or phase plate is an optical device that alters the polarization state of a light wave travelling through it. Two common types of wave plates are the half-wave plate, which shifts the polarization direction of linearly polarized light, and the quarter-wave plate, which converts linearly polarized light into circularly polarized light and vice versa[53,54]. Thus phase plates are useful optical accessories for enhancing the contrast in images of so called *weak phase objects*.

In electron optics a phase plate cannot affect a polarization. Instead the quantum mechanical phenomenon of the potential well[32] is utilized to achieve the phase shift. In presence of a potential the electron's energy is altered and thus the wavelength. An electron wave traveling through a potential gets shifted in phase relative to a wave that has not traveled through the potential due to different wave lengths in regions with and without potential. This effect is not exclusively used for phase plates in transmission electron microscopy — it is omnipresent.

Any sample interacts with primary beam electrons and thus influences the amplitude and phase of the electron wave. Here one can distinguish between amplitude and phase contrast. *Amplitude contrast* is caused by scattering and diffraction effects[55], while *phase contrast* basically is caused by the inner potentials of the sample. Lightweight samples — e.g. biological specimens, which consist basically of carbon — of thicknesses $\lesssim 50\,\mathrm{nm}$ are considered as pure phase objects. In case of *weak phase objects*, which cause little or no amplitude contrast at all, one can increase the defocus, which will cause edge diffraction patterns to be imaged. In life sciences this is considered as a way to increase contrast in the image. Alternatively one can insert a phase plate into the diffraction plane of the TEM, which will not require a defocus leading to diffraction patterns in the image. Using the latter option one speaks of phase contrast microscopy (PCM)[56–59].

The objective for phase plates in PCM is to introduce a phase difference between the Bragg scattered beams and the non-scattered beam in the diffraction plane ($\equiv$ back focal plane of objective lens). So far most designs in practical use are based on electrostatic potentials to realize the phase shift[59]. But proposals for magnetic phase plates do exist[60].

In the following a quick overview of the most common phase plate designs shall be given in Sec. 3.1. Afterwards — in Sec. 3.2 — we will focus on the adaptation of electrostatic phase plates for the proposed experimental setup from Sec. 2.2.3; here different adaptations will be featured in order to take into account more realistic circumstances during fabrication.

3.1. State of the Technology

Phase plates for electron microscopy can basically be divided into two groups: *thin film phase plates* and *obstacle-free phase plates* that introduce no — or a required minimum of — material

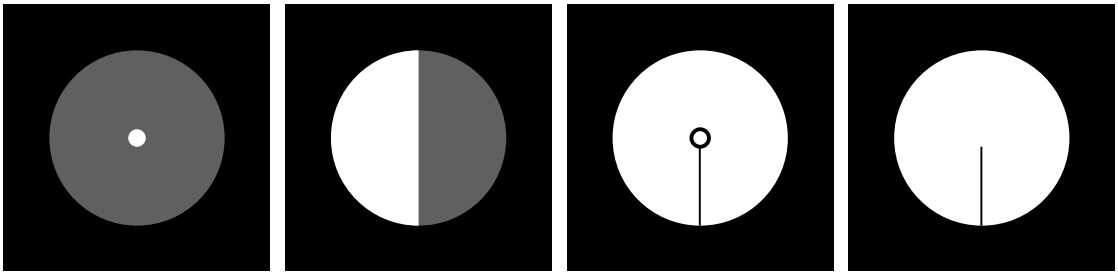

(a) Zernike Phase Plate (b) Hilbert Phase Plate (c) Boersch Phase Plate (d) Zach Phase Plate

Figure 3.1.: Schematic drawings of the most prominent phase plate designs except the anamorphotic one. **Black** are all parts of the phase plates that are intended to be opaque for electrons. Thin films are painted in **gray**. **White** indicates the absence of matter.

into the electron beam. In this section we will follow the compositions in Refs. [61, 62]. The interested reader will find more detailed information on the different phase plate designs in those publications. Fig. 3.1 gives an overview of the most common phase plate designs, which are listed with short explanations of their working principles below.

3.1.1. Thin Film Phase Plates

Zernike Phase Plates are made of a thin film of amorphous carbon into which a small hole is milled. Bragg scattered beams travel through the amorphous film and become shifted in phase by the inner mean potential of the carbon, while the non-scattered beam passes through said hole[61].

A non-centrosymmetric approach, denoted as *Hilbert Phase Plate*, provides contrast enhancement at low and intermediate spatial frequencies[63]. A Hilbert phase plate consists — like the Zernike phase plate — of thin film; but in this case the film only covers one half-plane of the aperture plane. Positioned close to the zero-order beam, Hilbert phase plates impose a phase shift on the electrons in one half of the diffraction pattern with the exception of the zero-order beam itself.[61,64].

The interested reader can find in Ref. [65] an experimental study of the different behavior of Zernike and Hilbert phase plates in PCM. As one can imagine thin film phase plates suffer from a serious disadvantage. Electron irradiation can damage the film or grow contaminations[42]. Either way the behavior of a thin film phase plate will be altered. Thus the development of obstacle-free phase plates is in the focus of recent research.

3.1.2. Obstacle-free Phase Plates

Electrostatic Boersch Phase Plates[5,52,62,66,67] are small electronic devices. A ring electrode is placed in the center of an aperture hole and coated with an insulator on the outside. To prevent the propagation of an applied potential into the microscope column the insulator is coated with a metallic layer that is connected to the microscope ground terminal. The non-scattered beam is passing through the ring electrode and shifted in phase while the scattered Bragg beams

pass through the aperture outside of the ring electrode. Due to this material inserted into the diffraction pattern one looses some spatial information. For small ring electrode diameters the phase shift can be approximated as constant[5] (see Sec. 4.3.2).

A phase plate design based on the assumption that no constant phase shifts are required in the aperture plane for PCM is called *Zach Phase Plate*[61,68–70]. The Zach phase plate is similar in design to the Boersch phase plate; it simply omits the ring electrode and consists of simply one rod. This rod causes an electrostatic potential with a strong radial gradient, the maximum of which is intended to be close to the unscattered beam. Thus the Zach phase plate allows more spatial frequencies to contribute to the image.

Even if the phase plate material introduced to the electron beam is reduced to an absolute minimum high-energy electrons (200 – 300 keV) still can penetrate thick materials (up to 20 µm and more, see Sec. 5.3). As illustrated in Chap. 7 electrons penetrating insulating layers in the phase plate material can — by means of charging effects — introduce strong aberrations to the beam transmitted by the phase plate and thus cause a degradation of image quality and resolution.

Therefore a completely different approach of phase plates referred to as *anamorphotic phase plates* is inspired by the working principle of corrector devices for astigmatism — called stigmators. To avoid the problems of charging in the phase plate material (see Sec. 7.2) and cut-off of spatial information by the field-forming electrodes, these devices are designed to expose no phase plate material to the electron beam at all.

A phase shift is applied to a strongly anamorphotic[a] image of the diffraction plane[71,72]. By means of a highly anisotropic field distribution (see Fig. 3.2 for electrode arrangement), which is placed at an anamorphotic image of the diffraction plane — a plane where the diffraction image is compressed in one direction by means of multipole elements[72] — the phase is shifted in a thin stripe-shaped region[71]. To get a symmetric phase shift for PCM applications one requires two phase plates, each of which is positioned at one of two crossed anamorphotic diffraction planes. Thus such a pair of anamorphotic phase plates is installed in an astigmatism corrector.

Fig. 3.2 illustrates the design of an anamorphotic phase plate. The anamorphotic image is compressed to fit inside the slit of the phase plate. At the central electrodes a potential U_0 is applied. Depending on the chosen potentials U_1 and U_2 the phase shifting behavior of a Zernike ($U_1 = U_2,\ U_1 \neq U_0$) or Hilbert ($U_1 = U_0,\ U_2 \neq U_0$) phase plate can be reproduced. The interested reader can refer to Refs. [59, 61, 72, 73] for more detailed treatment of the working principles of anamorphotic phase plates.

3.1.3. Application

Phase plates are commonly used in phase contrast microscopy during the investigation of transparent samples or *phase objects* — e.g. living cells or microorganisms — in a light or electron microscope. Especially biological specimens, which predominantly consist of carbon, are considered as phase objects, which change the phase of incident (electron) waves rather than their amplitude[59]. As pointed out in Sec. 3.1 phase plates introduce a phase shift, which in most

[a] compressed

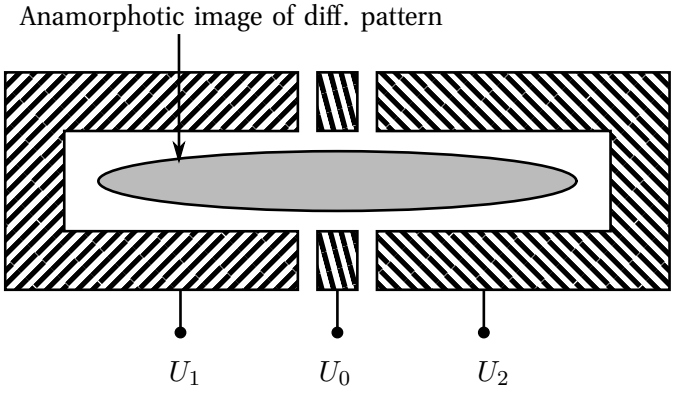

Figure 3.2.: Schematic electrode arrangement in anamorphotic phase plate. The ellipse inside this arrangement indicates where the anamorphotic image of the diffraction pattern is to be expected. Depending on the choice of the U_is the behavior of a Zernike or Hilbert phase plate can be reproduced.

cases has a value of $\pi/2$[5,59,61], onto some beams in the diffraction plane. In the image plane the superposition of these beams can show a maximized contrast in the intensity distribution, if the phase information is *rotated by* $\pi/2$.

The underlying principle can be understood by looking at the complex valued representation ψ of amplitude A and phase ϕ information $\psi = A \cdot \exp(-i\phi)$. A rotation of the phase information by $\pi/2$ means that an initial pure phase information is transformed into a pure amplitude information, which is observable in the intensity distribution $|\psi|^2$.

Fig. 3.3 shows a phase contrast x-ray image of a wasp. The image contrast is enhanced by a quarter-wave plate[75,76]. The combination of a high-brightness x-ray source and a quarter-wave plate brings low contrast features to good visibility.

Remaining in the realm of electron microscopy one can find only a few commercially offered phase plates, e.g. at Jeol one can obtain Zernike phase plates. The most promising electrostatic, anamorphotic phase plates have not found their way into (commercial) applications as they require a rather drastic modification of the optics of an electron microscope. As stated in Ref. [72] this kind of phase plates most conveniently would be installed between multipole elements of an astigmatism correcting device, e.g. a C_s corrector[b].

An alternative technique suitable for visualizing phase contrast is *differential phase contrast*[77–81] (DPC) which is preferably used in material science and which we will use for a different purpose in Sec. 7.2.1. A basic explanation of DPC will be given in Sec. 6.1.4.

[b] Corrector for spherical aberration.

Figure 3.3.: Phase contrast X-ray image of a wasp with good visibility of low contrast features acquired with the Excillum X-ray source[74]. Image published by “Excillium AB” under *Creative Commons Attribution* 3.0 (CC BY 3.0) license.

3.2. Design Adaptations

For the purposes of this work (see Chap. 2) most concerns of phase contrast microscopers regarding the loss of spatial information in the diffraction plane are irrelevant as the proposed setup for a new EMCD technique contains phase plates in the condenser plane of a transmission electron microscope (TEM; see Fig. 2.3). For this new technique the condenser aperture is required to shape two beams and allow the application of electrostatic potentials to shift the phase of single beams.

These tasks are performed by an adaptation of the electrostatic Boersch phase plate to which we will refer in this work as *twin aperture*. We will use as well a stack of metallic and insulating layers[5,66] with some deviations from the original design as pointed out in Sec. 6.2. At this point we will focus on the design considerations of the twin aperture as these are relevant for finite element method calculations in Chap. 4.

Fig. 3.4 shows schematic drawings, which are not drawn to scale, of cross sections (left hand side) and top views (right hand side) of different phase plate and twin aperture designs. The first one is the original Boersch phase plate, where the supporting rods of the ring electrode are omitted (compare Figs. 3.1 and 3.4a). As described above the Boersch phase plate consists of an encased ring electrode inside an aperture hole. The actual phase shifting potentials of such a Boersch phase plate are investigated in Sec. 4.3.2.

The twin aperture design consists of two adjacent aperture holes (see Fig. 3.4b-f). Ring electrodes at each hole are embedded in insulating material between a bottom and top metallic layer. Given the knowledge of Boersch phase plates Fig. 3.4b shows the most direct approach towards twin apertures. The geometrical arrangements have been changed as described while the layer thicknesses (see Table 6.1) remain approximately the same. As will be pointed out

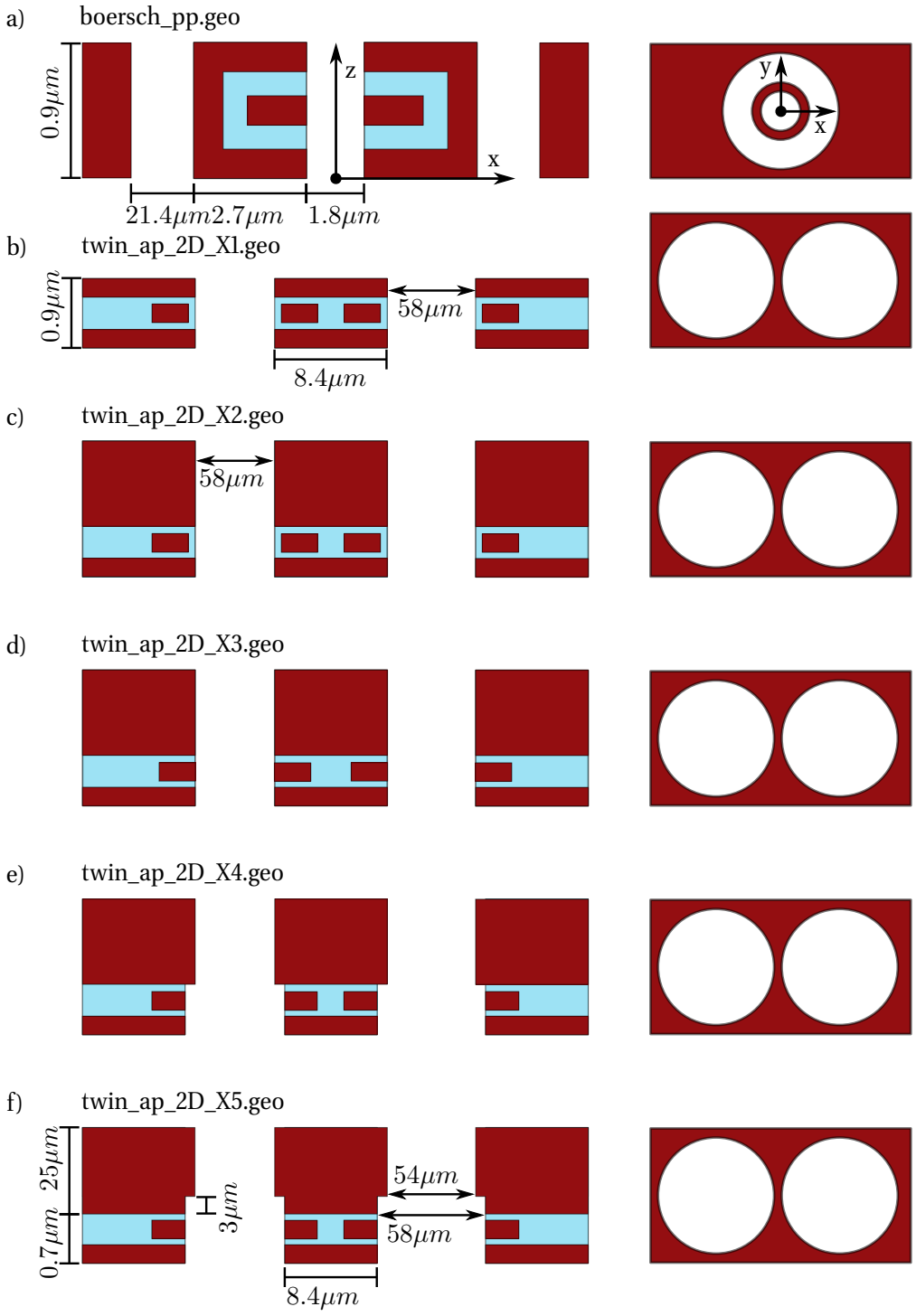

Figure 3.4.: Schematic drawings (not true to scale) of cross sections and top views of the different phase plate designs investigated in this work. In subfigure **a** the orientations of the coordinate axes are indicated. Metallic parts are indicated in **dark red**, insulating parts in **light blue**. Starting from the (**a**) Boersch phase plate we will continue with the (**b**) twin aperture design and conclude with (**c-f**) variations in top layer thickness and ring electrode diameters.

in Sec. 5.3 and Chap. 7 “thin” phase plates (thickness $\lesssim 20\,\mu m$) can be penetrated by primary beam electrons leading to serious problems (see Chap. 7).

Having encountered strong aberrations due to charging effects (see Sec. 7.2) and determined an approximate penetration depth for primary electrons (see Sec. 5.3) further design considerations (see Figs. 3.4c-f) have a “thick” metallic layer at the top.

Subfigures *c* and *d* assume different diameters for the ring electrode; in the first case the inner diameter of the ring is larger than the hole diameter. In the latter figure said diameters are equal. These designs take into account the deficiencies of the production process: During the milling through a layer of thickness $\gtrsim 20\,\mu m$ no sharp edges can be formed. Therefore a larger ring electrode diameter has been considered to prevent milling of parts of the ring electrode.

As the inclination of the cylindrical faces of the aperture holes might allow exposure of insulating material to the electron beam subfigures *e* and *f* suggest a design containing an additional milling step creating a cylindrical hole with slightly larger radius to prevent such exposure. As one would not expect to control such a milling process to nanometer precision subfigure *f* regards the possibility of a larger milling depth in the second process.

The physical and mathematical description of the phase shift caused by electrostatic potentials and phase plates will be subject in Sec. 4.3.

4. Finite Element Method Calculations

In this chapter we want to investigate the actual electrostatic potential — and thus the phase shift — caused by Boersch phase plates of the original design[5,52,66] and the adapted designs as described in section 3.2. Therefore the Laplace equation has to be solved while regarding the phase plate's geometry. This leads to the need for a numerical solution.

The finite element method (FEM) is a numerical technique for finding approximate solutions to partial differential equations (PDE) and their systems. In simple terms, FEM is a method for dividing up a very complicated problem into small elements that can be solved in relation to each other. The solution approach is based on eliminating the spatial derivatives from the PDE. This approximates the PDE with a system of ordinary differential equations for transient problems[82].

These ordinary differential equations that arise in transient problems are then numerically integrated using standard techniques such as Euler's method or the Runge-Kutta method[82].

Before presenting results in section 4.3 the principal ideas of FEM will be pointed out in section 4.1. The interested reader may find more detailed information on FEM e.g. in Ref. [83].

4.1. Fundamentals of the Finite Element Method

4.1.1. Principle

Analytic solutions to physical or mathematical systems are often limited to simple shapes and straightforward boundaries that are rarely the objects of interest. In electrostatics, the electric potential inside a uniformly-charged ring or disk can be determined by solving Laplace's equation using a pencil and paper. Change the domain of the physical system just slightly — say, to that of a uniformly-charged letter R; see Fig. 4.1 — and the calculations become much more complicated[84].

The Finite Element Method (FEM) is a numerical tool that is highly effective at solving partial and nonlinear equations over complicated domains. It is an application of the Ritz method, where the exact PDE is replaced by a discrete approximation which is then solved exactly. FEM approximates the exact PDE as a matrix equation. The size of the matrix is dependent on the size of the the domain over which the PDE exists and the desired accuracy of the approximation[84].

4.1.2. Tessellation

Tessellation is a technique of dividing complex polygons into sets of more simple shapes like triangles or squares. This is commonly used in the rendering of textured polygons (CAD applications, computer games, . . .) or for solving PDEs using finite element methods.

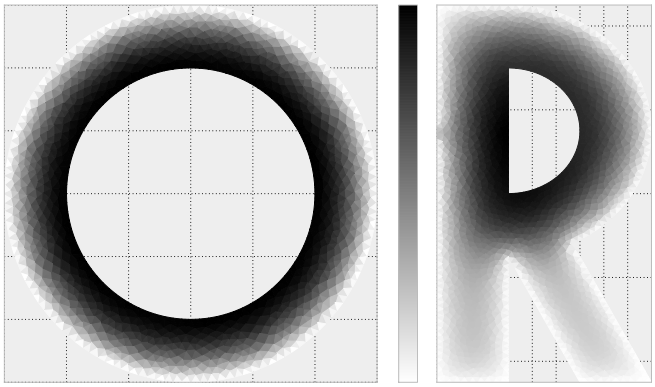

(a) Letter O, ring (b) Letter R

Figure 4.1.: Simple geometries on which a differential equation is to be solved. For the letter *O* an analytical solution can be determined rather quickly, but for the letter *R*, which is a slightly more complicated geometry, a solution cannot be given just as easy. In both cases similar boundary conditions have been applied: $f(x, y) = 0$ at the outer boundary of the lesser and $f(x, y) = 1$ at the inner boundary.

The finite element method approximates a variational problem as a solvable numerical problem by reducing the degrees of freedom of the system to a finite number as will be pointed out it section 4.1.3. While FEM can involve tessellation of both space and time dimensions, we will treat only space-dimension tessellation[84,85]. Regarding nomenclature we will follow the conventions used by the creators of the mesh generator *gmsh*[86] used in this work.

A finite element *mesh* is a tessellation of a given subset of the three-dimensional space domain by elementary geometrical elements of various shapes (see Fig. 4.2) arranged in such a way that if two of them intersect, they do so along a face, an edge or a node, and never otherwise. All the finite element meshes produced by Gmsh are considered as "unstructured". This implies that the elementary geometrical elements are defined only by an ordered list of their nodes but that no predefined order relation is assumed between any two elements.

The mesh generation is performed in a bottom-up manner: lines of a defined geometrical entity are discretized first; the mesh of the lines is then used to mesh the surfaces; then the

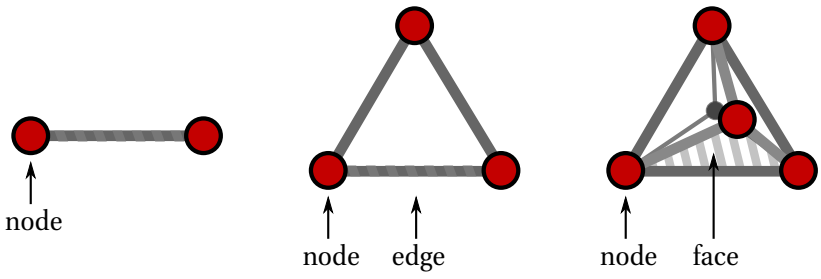

Figure 4.2.: Basic shape of a cell in one (left), two (center) and three (right) dimensions.

mesh of the surfaces is used to mesh the volumes.

In this process, the mesh of an entity is only constrained by the mesh of its boundary. For example, in three dimensions, the triangles discretizing a surface will be forced to be faces of tetrahedra in the final 3D mesh only if the surface is part of the boundary of a volume; the line elements discretizing a curve will be forced to be edges of tetrahedra in the final 3D mesh only if the curve is part of the boundary of a surface, itself part of the boundary of a volume; a single node discretizing a point in the middle of a volume will be forced to be a vertex of one of the tetrahedra in the final 3D mesh only if this point is connected to a curve, itself part of the boundary of a surface, itself part of the boundary of a volume. This automatically assures the conformity of the mesh when, for example, two surfaces share a common line[86].

4.1.3. Numerical solution

To give an impression how the FEM works[87] we will have a look at a PDE in one dimension

$$\frac{\partial^2 y(x)}{\partial x^2} = c(x), \tag{4.1}$$

where $y(x)$ is the function to be determined on the domain $x \in [x_1, \ldots, x_n]$ and $c(x)$ is a known function, e.g. a charge distribution in Poisson's equation. Additionally we regard some boundary conditions $y(x_1) = a$ and $y(x_n) = b$.

The first step of FEM is to rewrite the PDE as a volume integral by multiplying an arbitrary trial function $v(x)$, which fulfills the condition $v(x_1) = v(x_n) = 0$, and integrating over the domain

$$\begin{aligned} \int_{x_1}^{x_n} v(x) \left(\frac{\partial^2 y(x)}{\partial x^2} - c(x) \right) \, dx = \\ \int_{x_1}^{x_n} \underbrace{v(x)}_{g(x)} \underbrace{\frac{\partial^2 y(x)}{\partial x^2}}_{f'(x)} \, dx - \int_{x_1}^{x_n} v(x)c(x) \, dx = 0. \end{aligned} \tag{4.2}$$

By partially integrating (see Eq. 4.3) the first term in equation 4.2 the equation is transformed into the so called *weak form*[87]

$$[f(x) \cdot g(x)]_{x_1}^{x_n} - \int_{x_1}^{x_n} f(x) \cdot g'(x) \, dx = \int_{x_1}^{x_n} f'(x) \cdot g(x) \, dx \tag{4.3}$$

$$\left[v(x) \frac{\partial y(x)}{\partial x} \right]_{x_1}^{x_n} - \int_{x_1}^{x_n} \frac{\partial v(x)}{\partial x} \frac{\partial y(x)}{\partial x} \, dx - \int_{x_1}^{x_n} v(x)c(x) \, dx = 0 \tag{4.4}$$

$$\int_{x_1}^{x_n} \frac{\partial v(x)}{\partial x} \frac{\partial y(x)}{\partial x} \, dx + \int_{x_1}^{x_n} v(x)c(x) \, dx = 0, \tag{4.5}$$

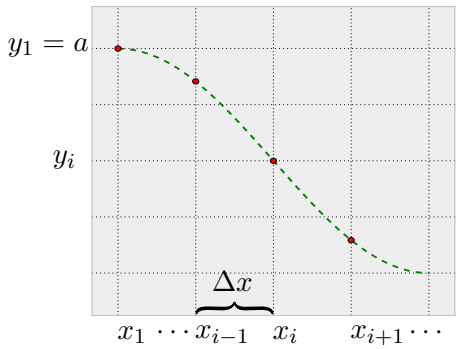

(a) To be determined by FEM: function $y(x)$.

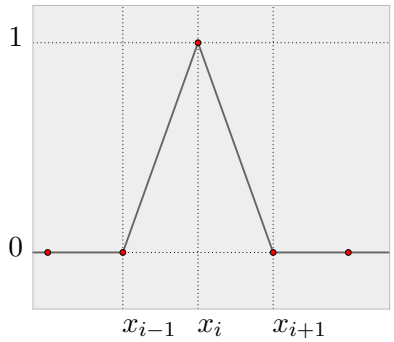

(b) (Global) Shape function $N_i(x)$.

Figure 4.3.: Function $y(x)$ that is to be approximated on the domain $[x_1, x_n]$ in terms of the shape functions $N_i(x)$ (see Eq. 4.11).

where $f'(x)$ is the first derivative of $f(x)$ and $g'(x)$ is the first derivative of $g(x)$, respectively. Due to the proclaimed property $v(x_1) = v(x_n) = 0$ of the trial function the first term in Eq. 4.4 vanishes

$$\left[v(x) \frac{\partial y(x)}{\partial x} \right]_{x_1}^{x_n} = 0. \tag{4.6}$$

Whereas $y(x)$ needs to be twice continuously differentiable in Eq. 4.2 — the so called *strong form* — $y(x)$ only needs to be only continuously differentiable in the weak form (Eq. 4.5). Using the FEM one does not obtain the solution $y(x)$ but computes an approximation $\tilde{y}(x)$

$$y(x) \approx \tilde{y}(x) = \sum_{i=1}^{n} N_i(x) \hat{y}_i(x) \tag{4.7}$$

$$= [N_1(x), \ldots, N_n(x)] \begin{bmatrix} \hat{y}_1(x) \\ \vdots \\ \hat{y}_n(x) \end{bmatrix} = \mathbf{N}\hat{y}(x), \tag{4.8}$$

where the continuous function $y(x)$ has been broken up into a set of n discrete values $(\hat{y}_i(x), x)$ which are combined and interpolated by the global weight functions $N_i(x)$ with the following properties

$$N_i(x) = \begin{cases} 1 & x = x_i \\ 0 & x \neq x_i \end{cases} \tag{4.9}$$

$$\sum_i N_i(x) = 1 \tag{4.10}$$

Eq. 4.9 defines the properties an actual weight function $N_i(x)$ has to fulfill on elements x_i

of the domain x. For a linear interpolation between these nodes the hat function (Eq. 4.11) can be chosen conveniently

$$N_i(x) = \begin{cases} 1 - \frac{x_i - x}{\Delta x} & x_{i-1} \leq x \leq x_i \\ 1 - \frac{x - x_i}{\Delta x} & x_i < x \leq x_{i+1} \\ 0 & \text{else} \end{cases}, \tag{4.11}$$

where Δx is the distance between elements of the domain $\Delta x = x_i - x_{i-1}$. Thus the weak form in equation 4.5 becomes

$$0 = \int_{x_1}^{x_n} \frac{\partial v(x)}{\partial x} \frac{\partial \mathbf{N}(x)}{\partial x} \hat{y}(x)\ dx + \int_{x_1}^{x_n} v(x)c(x). \tag{4.12}$$

By choosing a test function $v(x)$ and inserting this test function into equation 4.12 this equation transforms to a system of linear equations that can be solved numerically or analytically

$$v(x) = \mathbf{N}(x)\delta\mathbf{y} \tag{4.13}$$

$$\delta\mathbf{y} = [\delta y_1, \ldots, \delta y_n]^T \tag{4.14}$$

$$0 = \delta\mathbf{y}^T \left(\left(\int_{x_1}^{x_n} \frac{\partial \mathbf{N}^T(x)}{\partial x} \frac{\partial \mathbf{N}(x)}{\partial x}\ dx \right) \hat{y} + \int_{x_1}^{x_n} \mathbf{N}^T(x)c(x)\ dx \right), \tag{4.15}$$

where $\mathbf{N}(x)$ is the array of shape functions and $\delta\mathbf{y}$ is an array of arbitrary values. $\mathbf{N}^T$ is the transposed of $\mathbf{N}$. As equation 4.15 has to be fulfilled for any $\delta\mathbf{y}$ the equation can be written as

$$\mathbf{K}\hat{y} = \mathbf{f} \tag{4.16}$$

$$\mathbf{K} = \int_{x_1}^{x_n} \frac{\partial \mathbf{N}^T(x)}{\partial x} \frac{\partial \mathbf{N}(x)}{\partial x}\ dx \tag{4.17}$$

$$\mathbf{f} = -\int_{x_1}^{x_n} \mathbf{N}^T(x)c(x)\ dx \tag{4.18}$$

In order to regard boundary conditions one has to modify the values of $\mathbf{K}$ and $\mathbf{f}$ prior to solving the equation system 4.16. Boundary conditions in this one dimensional example are applied to the first and last node of the domain

$$f_i = f_i - \mathbf{K}_{i1}a - \mathbf{K}_{in}b \tag{4.19}$$

$$\mathbf{K}_{ij} = \begin{cases} 1 & \text{if } (i = 1 \vee i = n) \wedge i = j \\ 0 & \text{if } (i = 1 \vee i = n) \wedge i \neq j \\ \mathbf{K}_{ij} & \text{else} \end{cases}. \tag{4.20}$$

In this rather simple FEM algorithm we have only regarded Dirichlet boundary conditions and neglected the possibility of Neumann boundary conditions. As pointed out previously the interested reader might want to take a closer look at references [87] and [83] for a more detailed description of FEM.

After transforming the initial PDE (Eq. 4.2) into a matrix equation (Eq. 4.16) containing one $n \times n$ matrix solving this equation might become difficult regarding that n is the number of nodes. This problem can be circumvented when switching from a global to a local setting. As the shape functions N_i (Eq. 4.9) are defined to be zero at all nodes except for x_i one can solve equation 4.16 for each element e in the domain

$$\sum_e \left(\int_{x_i}^{x_j} \frac{\partial (\mathbf{N}^e)^T}{\partial t} \frac{\partial \mathbf{N}^e}{\partial x} \hat{y}^e(x)\, dx - \int_{x_i}^{x_j} (\mathbf{N}^e)^T c(x)\, dx \right) = 0 \tag{4.21}$$

$$\Rightarrow \sum_e \mathbf{K}^e \hat{y}^e(x) = \sum_e \mathbf{f}^e, \tag{4.22}$$

where e is the element between two consecutive nodes x_i and x_j. Instead of an equation with one $n \times n$ matrix we now simply have to solve $n - 1$ equations containing 2×2 matrices.

At this point we will not continue in the discussion of numerically solving a PDE but continue in the course of investigating the electrostatic potential of a phase plate using the afore mentioned techniques.

4.2. Solving Laplace's equation

One of the cornerstones of electrostatics is Poisson's equation, which allows to determine the potential ϕ for some given charge distribution ρ and well known boundary conditions. In this case we want to investigate the phase shift applied to an electron wave caused by — generally speaking — an electrostatic ring electrode. Due to the absence of free charges the equation simplifies to Laplace's equation

$$\nabla^2 \phi = \frac{\rho}{\epsilon} = 0, \tag{4.23}$$

where ∇^2 is the Laplace operator and ϵ is the permittivity.

Due to the complex boundary conditions given by the phase plate designs an analytical solution would be not possible. Therefore we use the numerical PDE solver FiPy[88] to solve Eq. 4.23 on a mesh generated by the mesh generator gmsh[86]. Figure 4.4 shows such a mesh for the default Boersch phase plate (compare Fig. 3.4a) and the solution (more to this later) on a logarithmic, periodic colorbar.

In order to get realistic results we have to investigate the potential ϕ to some extent in free space. On the other hand the dimensions of the phase plates (about 60 – 130 µm in x and y direction, about 1 µm in z direction) differ by about two orders of magnitude. Generation of a suitably large mesh with suitably small elements is a limiting factor in the following calculations. Therefore we have chosen to limit the investigation to the xz plane, which contains the optical axis and the centers of the apertures. The orientation of the coordinate system (x, y, z) with respect to the phase plates is indicated in figures 2.3 and 3.4. Note that Fig. 3.4 is not drawn to scale in order to better visualize the structure of the phase plate designs.

The boundary conditions are derived from the common three-electrode design of the phase plates (compare Fig. 3.4). In case of the classical Boersch phase plate (see Fig. 3.4a) all metallic

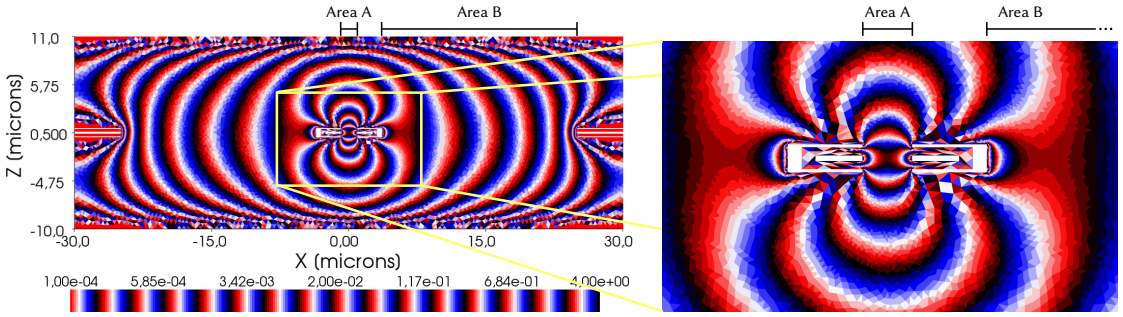

(a) Boersch Phase Plate (see Fig. 3.4a).

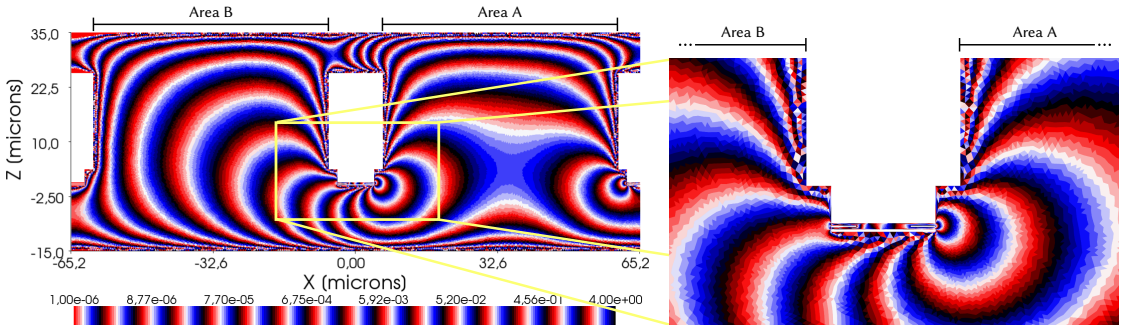

(b) Twin aperture (see Fig. 3.4f).

Figure 4.4.: Electrostatic potentials in free space caused by (**a**) Boersch phase plate or (**b**) twin aperture calculated using FiPy for a potential $U = 4\,\mathrm{V}$. To visualize the extent of the potentials a logarithmic, periodic color map has been chosen. Regions of interest for further evaluation are highlighted. Images on the right hand side show a close up on the phase plate structures in order to visualize the size of these structures.

surfaces, except those of the actual ring electrode, are set to a grounded potential $\phi = 0\,\mathrm{V}$, while the central ring electrode will be connected to a phase shifting potential $\phi = U$. Surfaces in the twin aperture designs (see Fig. 3.4b-f) are set to a grounded potential in an analogous way. Instead of a central ring the ring electrode in the $x > 0$ half plane will be set to a different potential U.

In order to determine a potential dependent model of the phase shift due to the phase plates we solve Eq. 4.5 for different boundary conditions $U \in [0.05\,\mathrm{V}, 10\,\mathrm{V}]$. As indicated in Fig. 4.4 we will treat the potential ϕ in different regions of the phase plates separately. With *Area A* we will denote a subset of the xz plane which is limited by the ring electrode on potential U. *Area B* will be the remainder of the xz plane that an electron traveling along the z direction can pass. In case of the Boersch phase plate (see Fig. 4.4a) we regard the radial symmetry of the aperture and limit *Area B* to its parts on the $x > 0$ half plane.

4.3. Modelling Phase Shift

In order to give an accurate expression for the electron wave function in the sample plane (see Fig. 2.3) in Chap. 5 one needs an analytical expression for the phase shift caused by the twin aperture in the C2 aperture plane. Therefore we will produce analytical models to reproduce the numerical results from the previous section 4.2.

Furthermore we need an expression that relates the electrostatic potential caused by the phase plates with an actual phase shift. In doing so we will utilize the weak lens approximation which states that the potential of the phase plate has to be much smaller than the total energy of the accelerated electron. Thus one can assume that the electron passes through the phase plate in a straight line without getting deflected.

4.3.1. Electron Optical Background

The principle of electrostatic phase plates is subject to every course in quantum mechanics (compare Ref. [32]). One of the most simplest cases is the potential barrier in one dimension, which is located in the path of an electron wave. The electron has in front of and after the barrier the same wave length, but inside the barrier the wave length has a different value depending on the magnitude of the potential (see Fig. 4.5). Thus an electron traversing such a barrier is shifted in phase relative to an electron that travels through free space.

Figure 4.5 illustrates a one dimensional potential barrier and the phase shift it causes to an electron wave passing through this barrier (green wave) relative to a wave travelling the same distance in absence of this barrier (red wave). The change in wave length and thus the phase difference between the two waves can simply be determined by solving the Schrödinger equation in case of non-relativistic electrons. The Schrödinger equation 4.24 and the wave length inside (Eq. 4.25) and outside (Eq. 4.26) of the barrier are given according to Ref. [32] as

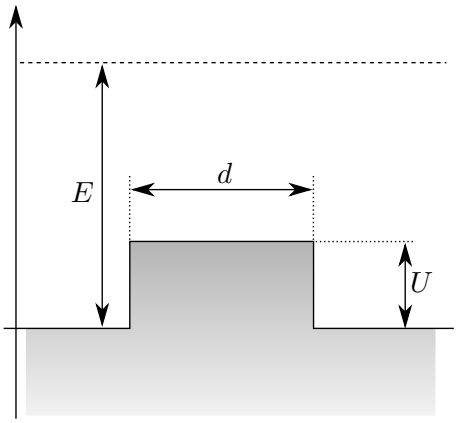

(a) Potential barrier.

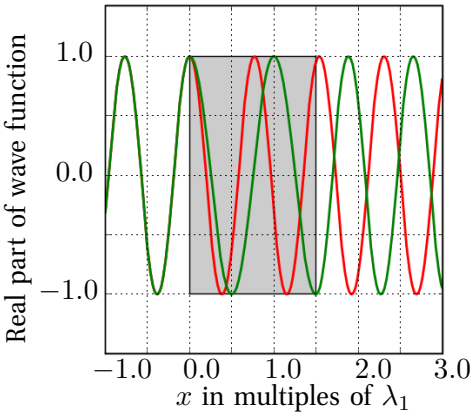

(b) Phase shift.

Figure 4.5.: One dimensional potential barrier of width d and height U (Fig. 4.5a). The incoming electron has energy E, where $E > U$. The real parts of the wave travelling through free space (red curve) and of the wave travelling through the potential barrier (green) are shown in Fig. 4.5b. The barrier is marked by a gray rectangle and has a width of $1.5\lambda_1$. The red wave has in the entire region a wave length of $\lambda_1 = 2\pi/k_1$ with $k_1 = 1$. The green wave has in front of and after the barrier also the wave length λ_1. In the region of the barrier the wave length is altered to $\lambda_2 = 2\pi/k_2$ with $k_2 = 1.3$.

$$\frac{d^2\psi}{dx^2} = -\frac{2m(E-V)}{\hbar^2}\psi \tag{4.24}$$

$$\lambda_2 = \hbar\pi\sqrt{\frac{2}{m(E-U)}} \tag{4.25}$$

$$\lambda_1 = \hbar\pi\sqrt{\frac{2}{mE}}, \tag{4.26}$$

where the potential is $V = U$ inside the barrier and $V = 0$ outside of the barrier, λ_1 and λ_2 are the wave length inside and outside of the barrier, m is the electron mass, E its kinetic energy and $\hbar$ is the reduced Planck constant.

As electrons are typically accelerated to energies of 200 – 300 keV in a TEM the expressions in equations 4.25 and 4.26 need to be determined from the relativistic equivalent to the Schrödinger equation, which is the Dirac equation. For sake of simplicity we will use the results as given in Refs. [5, 42]

$$\lambda_1 = \frac{hc}{\sqrt{2EE_0 + E^2}} \tag{4.27}$$

$$\lambda_2 = \frac{hc}{\sqrt{2(E-U)E_0 + (E-U)^2}}, \tag{4.28}$$

where h is the Planck constant, E_0 is the electron rest energy and c the speed of light in vacuum.

In analogy to light optics we introduce an electron-optical refractive index n, which is defined as the ratio of the wave length λ_1 in a vacuum (and absence of external potentials) to the wave length λ_2 in matter (or an external potential V), as given in Ref. [42]

$$n(x,\, y\, z) = \frac{\lambda_1}{\lambda_2} = \sqrt{\frac{2(E - V(x,\, y\, z))E_0 + (E - V(x,\, y\, z))^2}{2EE_0 + E^2}}, \tag{4.29}$$

where E is the kinetic energy of an electron, E_0 its rest energy and V is the Coulomb potential in matter or — in this case — the external electrostatic potential caused by a phase plate. This expression can be simplified by assuming $V \ll E$ and E_0 (weak lens approximation)

$$n(x,\, y\, z) = 1 - \frac{V(x,\, y\, z)}{E}\frac{E_0 + E}{2E_0 + E} + \dots \tag{4.30}$$

Thus an optical path difference Δs and phase shift φ can be calculated[42] by integrating along the path — which we define to be along the z axis — of the electron

$$\Delta s = \int_z (n(x,\, y,\, z) - 1)\, dz \tag{4.31}$$

$$\varphi(x,\, y) = \frac{2\pi}{\lambda}\Delta s = \frac{2\pi}{\lambda E}\frac{E_0 + E}{2E_0 + E}\int_z V(x,\, y,\, z)\, dz, \tag{4.32}$$

$$= \frac{\pi}{\lambda E}\frac{E_0 + E}{E_0 + E/2}\int_z \phi(x,\, y,\, z)\, dz, \tag{4.33}$$

where we have replaced a general potential V with the potential ϕ calculated in Sec. 4.2. In addition we have used a common convention for coordinate systems in electron microscopy. The z axis is oriented along the optical axis of the microscope and xy planes are orthogonal to the optical axis.

In the following we will present the results of the previous calculations for the two different phase plate designs (compare Fig. 3.4) separately. In all subsequent calculations we will assume a primary energy of 200 keV and micrometers as unit of length. Furthermore we will assume that the $z = 0$ plane coincides with the bottom surface of the bottom layer of each phase plate design.

4.3.2. Boersch Phase Plate

Using the results from the finite element method calculations we will derive an analytical expression f for the phase shift $\varphi(x)$ according to Eq. 4.33, as we have only investigated a two dimensional cut plane.

Fig. 4.4a shows the electrostatic potential caused by the Boersch phase plate, where we have investigated a z range of $[-10\,\mu\text{m},\, 11\,\mu\text{m}]$ in the FEM mesh. In the central region ($x = [-0.9\,\mu\text{m},\, 0.9\,\mu\text{m}]$, *Area A*), which is a cross section of the ring electrode, the potential reproduces the results of a constant phase shift from Ref. [5] on first sight. In the outer annular

aperture area the potential has a different shape; one might compare it with the potential between two thin capacitor plates[a]. As we will show subsequently this stray potential leads to a non-linear gradient in the phase shift (see Fig. 4.6).

Fig. 4.6 shows the phase shift φ in the regions of interest (ROI) for boundary conditions $U = 0.05\,\mathrm{V}$ and $U = 0.1\,\mathrm{V}$. The data obtained for *Area A* shows artifacts at the edge of the ROI. These artifacts will be ignored in the process of fitting functions to the data. All data obtained from numerical calculations is fitted with models. Fig. 4.6 also shows the used fit functions as red dashed lines.

4.3.2.1. Area A

The phase shift within the central ring electrode (*Area A*) of the Boersch phase plate (right hand side in Fig. 4.6) is in good agreement with previous results and can be approximated with a function only depending on U. Calculating mean value μ and standard deviation σ of the phase shift $\varphi(x)$ in *Area A* one gets for the ratio μ/σ a value of $8 \cdot 10^{-3}$ meaning that the mean deviation from the mean value μ of data points on the right hand side in Fig. 4.6 is negligible compared to the mean value μ. This justifies the approximation $\varphi_U(x, y) = \varphi_U(0, 0)$.

In order to find a quantitative basis for the above approximation we will model the phase shift within the central ring electrode with a fit function f that also takes into account non-constant contributions, which we choose to be a hyperbolic cosine as hyperbolic functions are typically part of solutions to differential equations like the Laplace equation,

$$f(x, U) = \alpha(U) + \cosh\left(\beta(U) \cdot x\right) - 1, \tag{4.34}$$

where α and β are fit parameters. The subtraction of 1 takes into account that the phase shift has to vanish in absence of the potential

$$\lim_{U \to 0} f(x, U) = 0. \tag{4.35}$$

As we have solved the Laplace equation for values of the boundary conditions potential U in the range $[0.05\,\mathrm{V},\ 10\,\mathrm{V}]$ the dependence of the fit parameters $\alpha(U)$ and $\beta(U)$ on the applied ring potential U can be determined.

Fig. 4.7 shows the fit parameters α and β in dependence of the potential U. According to the model (see Eq. 4.34) the parameter α describes the offset of the phase shift. The parameter shows a linear behavior. Regarding that the phase shift has to drop to zero for $U = 0$ the parameter itself cannot have a constant term.

The parameter β scales the hyperbolic cosine. β can be fitted with a square root function. The expression for β cannot have a constant term in order to ensure that the phase shift becomes homogeneously zero for $U = 0$. Thus the fit parameters can be written as

[a] Distance between plates larger than plate diameter.

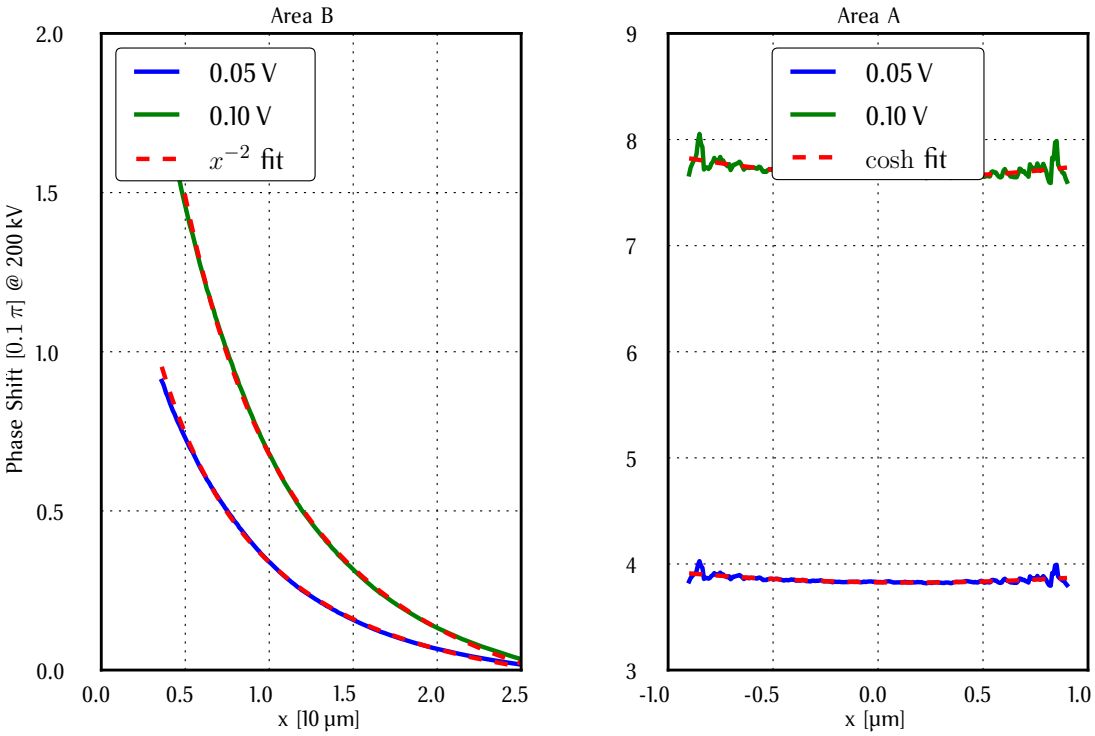

Figure 4.6.: Cross section along x axis of a Boersch phase plate showing phase shift for 200 keV electrons for potentials 0.05 V and 0.1 V applied to the phase plate. Note the different scaling factors (1, 10 and 0.1) given in the axis labels. **Right**: Phase shift for beams travelling through the ring electrode (*Area A*). **Left**: Phase shift for beams travelling through the aperture where commonly no potential is expected (*Area B*).

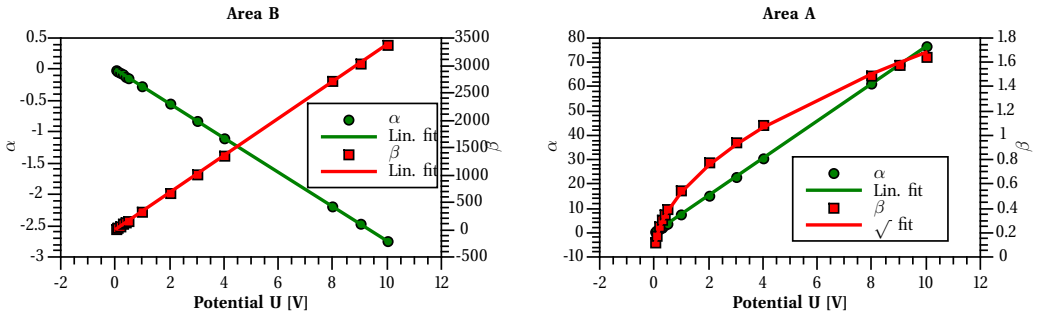

(a) *Area B* (b) *Area A*

Figure 4.7.: Fit parameters of the phase shift model in dependence of the potential in *Area A* and *Area B* for the Boersch Phase Plate.

$$\begin{aligned}\alpha(U) &\approx \left(7.65 \pm 8.59 \cdot 10^{-5}\right) U + \left(-9.16 \cdot 10^{-4} \pm 3.95 \cdot 10^{-4}\right) \\ &\approx 7.7\ U \end{aligned} \tag{4.36}$$

$$\begin{aligned}\beta(U) &\approx \left(5.32 \cdot 10^{-1} \pm 3.12 \cdot 10^{-3}\right) \sqrt{U} \\ &\approx 0.53\ \sqrt{U} \end{aligned} \tag{4.37}$$

Regarding the small diameter of the central ring electrode and that the hyperbolic cosine term in Eq. 4.34 contains a scaling factor proportional to the square root of the potential the entire hyperbolic cosine term changes only very slowly within the ring electrode. Thus it can be neglected with an error tolerance of $6 \cdot 10^{-3}\%$[b]. Therefore the phase shift exerted on an electron wave passing through this potential indeed can be assumed to be independent of x and y

$$\varphi(U) \approx f(U) = \alpha(U) = 7.7\ U. \tag{4.38}$$

4.3.2.2. Area B

Contrary thereto the potential leaping out of the ring electrode causes a gradient in phase shift (left hand side in Fig. 4.6) outside of the ring electrode. At the outer edge of the ring electrode's casing the effective potential and thus the phase shift has 24% of the mean value of the phase shift in *Area A*.

As electrostatic potentials, e.g. due to uniformly charged disks, tend to decrease with $1/r^2$ we choose a fit model of similar shape for the phase shift

$$f(x,\, U) = \alpha(U) + \frac{\beta(U)}{(x - \gamma(U))^2}, \tag{4.39}$$

where α and β are fit parameters describing the offset and scaling of the fit function as in *Area A*. γ replaces the constant d_i known from Eq. 4.34. As we are investigating the potential outside of the ring electrode we would expect a radial dependence relative to the center of the ring electrode. Furthermore we expect due to the metal casing some screening effects that will lead to a weaker potential. This screening will be regarded by the parameter γ, which can be thought of as a virtual, larger distance to the ring electrode's center.

Fig. 4.7a shows the fit parameters α and β in dependence of U. The parameter γ has been omitted in the plot as it is a constant independent of U. As before we derive expressions for the fit parameters

[b] Maximum of ratio between constant value and full expression for f.

$$\alpha(U) \approx \left(-2.74 \cdot 10^{-1} \pm 1.54 \cdot 10^{-7}\right) U + \left(1.67 \cdot 10^{-7} \pm 7.10 \cdot 10^{-7}\right)$$
$$\approx -2.74 \cdot 10^{-1} U \tag{4.40}$$
$$\beta(U) \approx \left(3.38 \cdot 10^{2} \pm 1.44 \cdot 10^{-4}\right) U + \left(1.45 \cdot 10^{-6} \pm 6.64 \cdot 10^{-4}\right)$$
$$\approx 3.38 \cdot 10^{2} U \tag{4.41}$$
$$\gamma = -8.86\,\mu\text{m} \tag{4.42}$$

where we again have assumed that the limit $U \to 0$ has to lead to $f = 0$. Thus the phase shift is given by

$$\varphi(x, U) \approx f(x, U) = \left(-2.74 \cdot 10^{-1} + \frac{3.38 \cdot 10^{2}}{(x + 8.86\,\mu\text{m})^2}\right) U. \tag{4.43}$$

4.3.3. Twin Aperture

As in Sec. 4.3.2 we will use the results from the FEM calculations in order to find an expression $f(x, U)$ to describe the phase shift $\varphi(x)$ obtained with Eq. 4.33 from the calculated potential, where we assume $E = 200\,\text{keV}$.

Fig. 4.4b shows the electrostatic potential calculated by FEM for the phase plate design called `twin_ap_2D_X5`, in which we investigated a z range of $[-15\,\mu\text{m}, 35\,\mu\text{m}]$ in the FEM mesh. Boundary condition U was applied to the ring cross sections on the $x > 0$ half plane. In the cross section of the aperture ($x = [4.2\,\mu\text{m}, 62.2\,\mu\text{m}]$, *Area A*) the potential shows a hyperbolic cosine behavior as one would expect from macroscopic electrostatics. In the other aperture ($x = [-62.2\,\mu\text{m}, -4.2\,\mu\text{m}]$, *Area B*) the potential has a similar shape as in *Area B* of the Boersch phase plate (compare Fig. 4.6), which resembles a hyperbolic decrease as one would expect outside of an unshielded ring electrode.

Fig. 4.8 shows the phase shift φ in the ROIs for boundary conditions $U = 0.05\,\text{V}$ and $U = 0.1\,\text{V}$. The data obtained for Area A shows an artifact at each edge of the ROI. These artifacts originate from the FEM calculations and will be ignored in the process of fitting functions to the data. The figure also shows the used fit functions as red dashed lines.

Due to the larger diameter of the ring electrodes in the twin aperture (see Fig. 4.4b) the phase shift can not be approximated as a constant without allowing an error of 48% [c]. Also the unshielded potential at the edge of the grounded aperture ($x = -4.2\,\mu\text{m}$) has 29% of the value of the potential at the center of the adjacent ring.

4.3.3.1. Area A

The phase shift within the ring aperture, to which the potential U is applied, cannot be approximated by a constant mainly due to the larger diameter of the aperture. Therefore we

[c] Ratio between standard deviation and mean value of data shown on the right hand side in Fig. 4.9b.

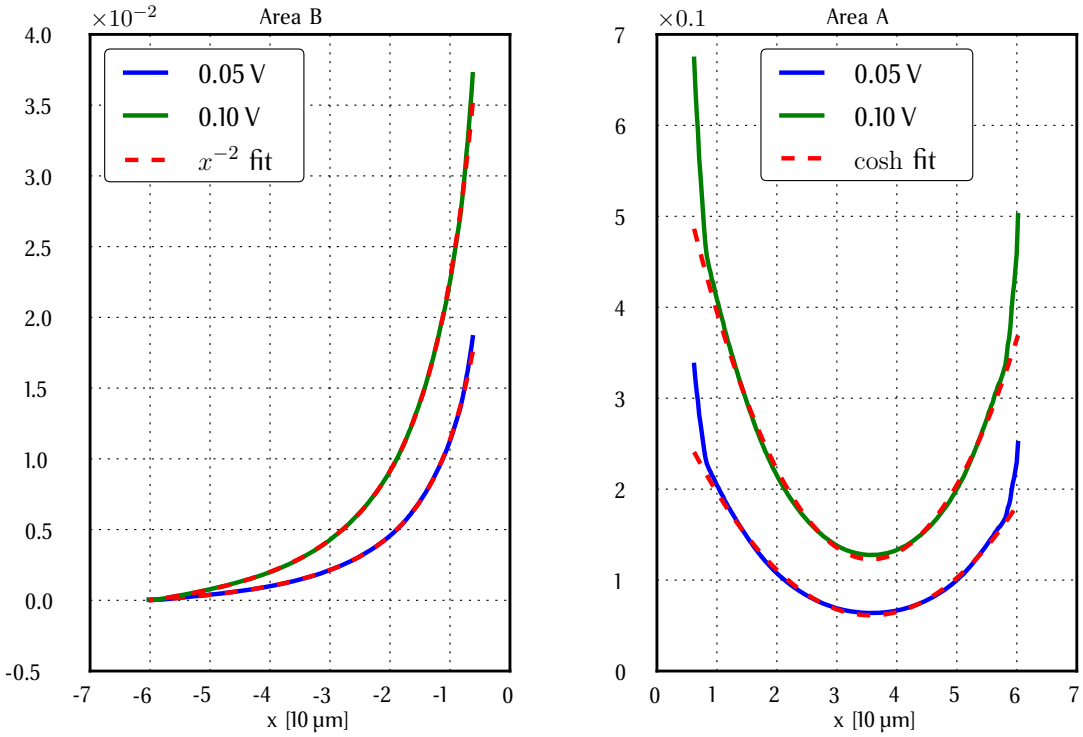

Figure 4.8.: Cross section along x axis of twin aperture showing phase shift for 200 keV electrons for potentials 0.05 V and 0.1 V applied to the phase plate. Note the different scaling factors on the phase shift axis. **Right**: Phase shift for beams travelling through the ring electrode (*Area A*). **Left**: Phase shift for beams travelling through the aperture where commonly no potential is expected (*Area B*).

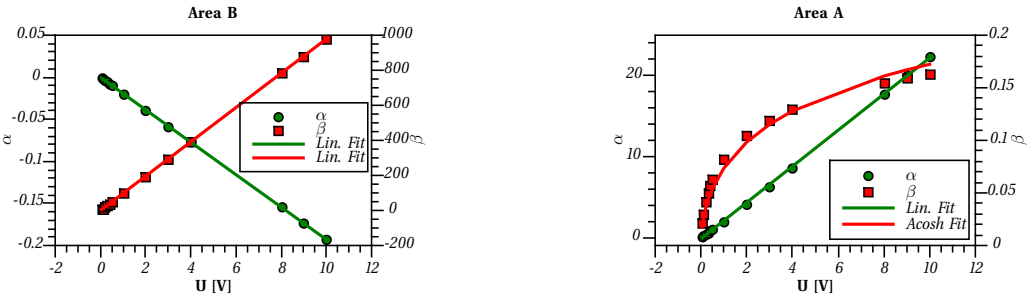

(a) *Area B*

(b) *Area A*

Figure 4.9.: Fit parameters of the phase shift model in dependence of the potential in *Area A* and *Area B* for the twin aperture.

will use a hyperbolic cosine to describe the phase shift. The model is identical to the one used for the Boersch phase plate and given by

$$f(x,\, U) = \alpha(U) + \cosh\left(\beta(U) \cdot (x - d_i)\right) - 1. \tag{4.44}$$

Fig. 4.9b shows the fit parameters α and β in dependence of the applied boundary condition potential U. As in Sec. 4.3.2.1 α describes an homogeneous offset and β is a scaling factor for the hyperbolic cosine. As previously α shows a linear dependence while β shows a hyperbolic arcus cosine dependence on U.

$$\begin{aligned}
\alpha \approx& \left(2.24 \pm 7.56 \cdot 10^{-3}\right) U + \left(-1.03 \cdot 10^{-1} \pm 3.48 \cdot 10^{-2}\right) \\
\approx& 2.24\ U && (4.45)\\
\beta \approx& \left(5.58 \cdot 10^{-2} \pm 6.76 \cdot 10^{-4}\right) \operatorname{acosh}(U+1) \\
\beta \approx& 5.58 \cdot 10^{-2}\ \operatorname{acosh}(U+1) && (4.46)\\
\varphi(x,U) \approx& f(x,U) = 2.24\ U + \cosh\left(5.58 \cdot 10^{-2}\ \operatorname{acosh}(U+1) \cdot (x - d_i)\right) - 1, && (4.47)
\end{aligned}$$

where d_i is the displacement of the aperture's center from the optical axis.

4.3.3.2. Area B

Area B is a cross section of the second annular aperture of the twin aperture. In the investigated cross section (see Fig. 4.4b) the potential due to the adjacent ring electrode on potential U is leaping into this area just as in the case of the Boersch phase plate. Therefore we will choose the same fit model Eq. 4.39

$$f(x,\, U) = \alpha(U) + \frac{\beta(U)}{(x - \gamma(U))^2}, \tag{4.48}$$

where α and β are fit parameters describing the offset and scaling of the fit function as in *Area A*. γ replaces the constant d_i known from Eq. 4.44. We are investigating the potential outside of the ring electrode, which is screened by a grounded metal casing. Despite the complexity of this screening the actual potential can mathematically be treated like a potential caused by an unshielded electrode at a larger distance, which accounts for the parameter γ in the fit function f in Eq. 4.48.

Fig. 4.9a shows the fit parameters α and β in dependence on U. The parameter γ has been omitted in the plot as it is a constant independent of U. As before we derive expressions for

the fit parameters

$$\begin{aligned}
\alpha(U) &\approx \left(-1.93 \cdot 10^{-2} \pm 1.27 \cdot 10^{-8}\right) U + \left(-3.32 \cdot 10^{-9} \pm 5.86 \cdot 10^{-8}\right) \\
&\approx -1.93 \cdot 10^{-2}\ U && (4.49) \\
\beta(U) &\approx \left(97.9 \pm 4.77 \cdot 10^{-5}\right) U + \left(1.81 \cdot 10^{-4} \pm 2.20 \cdot 10^{-4}\right) \\
&\approx 97.9\ U && (4.50) \\
\gamma &\approx 9.87\,\mu\text{m} && (4.51) \\
\varphi(x, U) &\approx f(x, U) = \left(-1.93 \cdot 10^{-2} + \frac{97.9}{(x - 9.87\,\mu\text{m})^2}\right) U. && (4.52)
\end{aligned}$$

4.3.4. Twin Aperture Variations

In the following subsection we will take a short look on the geometrical variations, mesh size dependencies and the influence of static negative charges in the twin aperture's insulating layers.

4.3.4.1. Geometry Variations

As having introduced five variations of the twin aperture in Chap. 3 (see Fig. 3.4) we also have to take a look on the remaining four designs. Using the same algorithms as in the previous sections the fit parameters have been determined. The interested reader can find the numerical values of the parameters α, β and γ in table A.1 in the appendix. In an additional column the z range of the mesh and the free space along the z axis above and below the phase plate, to which we will refer as δz, are shown.

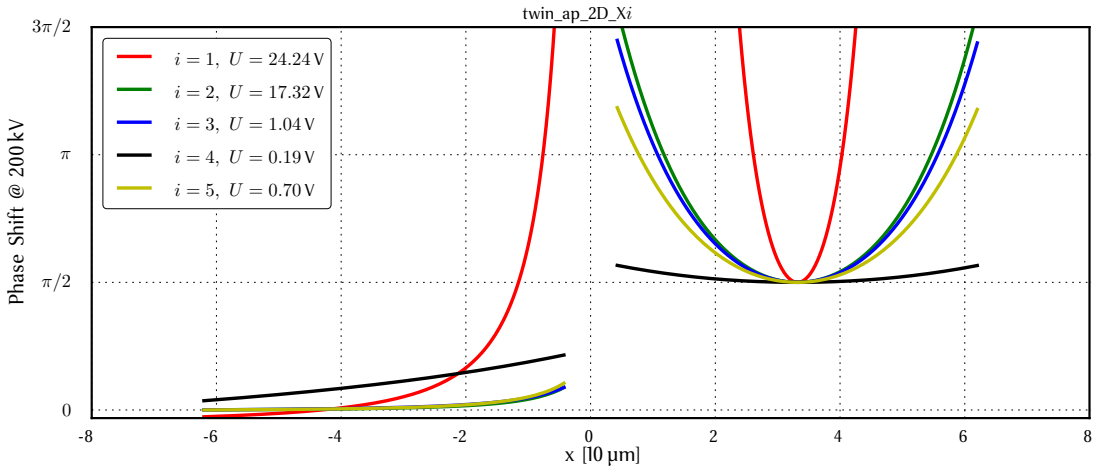

Figure 4.10.: Phase shift for the different designs `twin_ap_2D_Xi`, $i \in [1, 2, 3, 4, 5]$. In order to allow a comparison between designs for a desired phase shift of $\pi/2$ the potential U has been chosen such that the phase shift at the center of *Area A* is equal to $\pi/2$.

Fig. 4.10 shows the phase shifts for all the twin aperture variations introduced in Fig. 3.4, `twin_ap_2D_Xi` with $i = 1, 2, 3, 4, 5$. The applied voltages were chosen such that the hyperbolic cosine has the value $\pi/2$ at its minimum. Qualitatively the results (see table A.1) agree with those obtained in Sec. 4.3.3.

All parameters show the same functional dependence on U except for the thin twin aperture design `twin_ap_2D_X1`. This design shows in *Area A* an additional quadratic contribution in the fit parameter $\alpha(U)$. Furthermore the required voltage U is quite large compared to the other designs resulting in a very strong curvature of the phase shifts in both areas. Due to the problems related with *thin* twin apertures (see Secs. 5.3 and 7.2) we will not treat this design in our further investigations.

As the designs `twin_ap_2D_Xi` with $i \geq 2$ embody variations in the shape of the twin aperture one would not be surprised to get different quantitative results. The design `twin_ap_2D_X4` shows the most promising phase shifting behavior, but the production process (see Sec. 6.2) does not allow such an exact control of milling depth. Thus the design `twin_ap_2D_X5` is — regarding said limitation — the most promising candidate.

4.3.4.2. Mesh Variations

Additionally to the designs introduced in Chap. 3 calculations have also been performed for meshes called `twin_ap_2D_X5_i`, $i \in [2, 3, 4, 5]$, in which the twin aperture geometries are identical to `twin_ap_2D_X5` — the design investigated in Sec. 4.3.3. By investigating `twin_ap_2D_X5_i` (see Fig. 4.11) we want to assure that the previous results are representative and not excessively dependent on mesh size[d] and cell size. Therefore the free space along the z axis, which we will refer to as δz, has been increased with increasing i. For details see Table A.1.

Unfortunately deviations from the hyperbolic cosine shape of the phase shift in *Area A* rise to non-negligible levels for larger values of δz. Therefore the fit model f has to be adapted in order to produce reasonable results

$$f(x, U) = \alpha(U) + \cosh\left(\beta(U) \cdot (x - d_i)\right) + \gamma(U) \cdot x - 1. \tag{4.53}$$

By introducing a third parameter γ the hyperbolic cosine becomes tilted and the results from the fitting algorithm agree well with the FEM data.

As it is not possible to apply the physically relevant boundary condition $\lim_{z\to\pm\infty} \phi = 0$ in a numerical calculation it has been applied instead to the top and bottom face of the mesh. Thus the size of the mesh has quite an influence on the result of the calculations as shows Fig. 4.11a.

The larger the distance between the phase plate and the top and bottom faces of the mesh the shallower the phase shift across the aperture in *Area A*, which results in β converging towards a value for increasing δz (see Fig. 4.11b). As β appears to approach a limit value for $\delta z \to \infty$ α shows no such convergence in the investigated range, which illustrates the quantitative deficiencies of the found results.

Assuming that α does not converge for $\delta z \to \infty$ — as indicated in Fig. 4.11b — and keeps its linear dependence on U this would lead to a considerable phase shift even for a very small

[d] Especially in z direction.

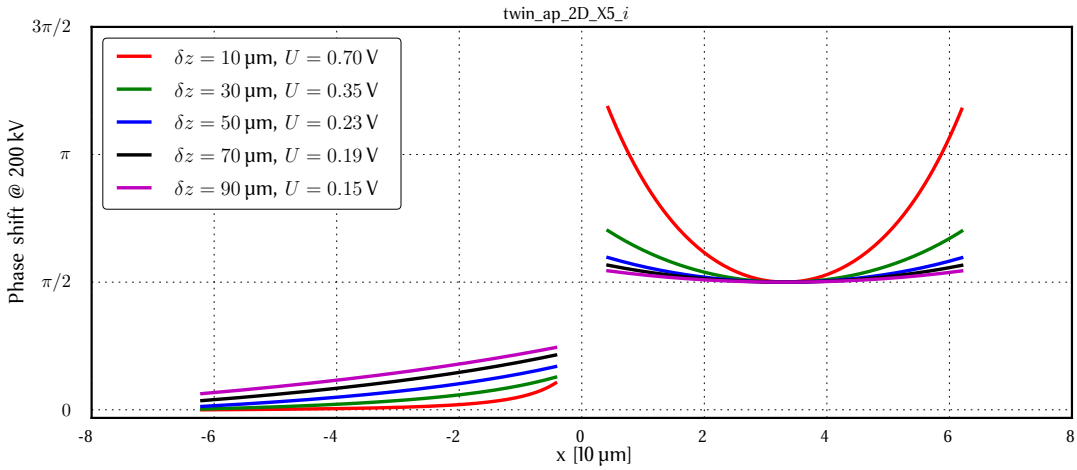

(a) Phase shift for the different designs `twin_ap_2D_X5` and `twin_ap_2D_X5_i`, $i \in [2, 3, 4, 5]$ (compare by δz with table A.1). In order to allow a comparison between designs for a desired phase shift of $\pi/2$ the potential U has been reduced with increasing i such that the minimum is approximately at the desired value.

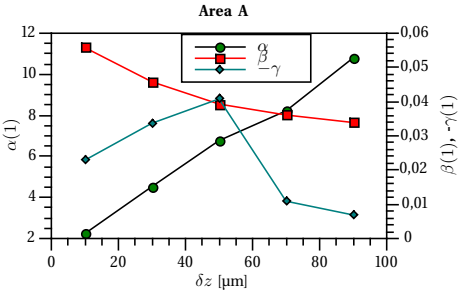

(b) Proportionality constants of the fit functions α and β for different δz in *Area A*.

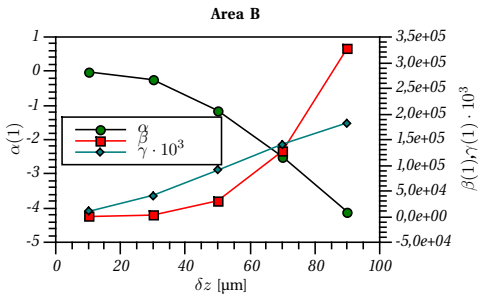

(c) Proportionality constants of the fit functions α and β for different δz in *Area B*.

Figure 4.11.: Phase shift for different meshes `twin_ap_2D_X5_i`, where δz increases with i, and fit parameters α and β.

voltage U. Thus one can argue that the actual geometry of the condenser lens and condenser aperture holder have to be regarded for an exact quantitative description of the phase shift.

On the other hand β in *Area B* increases with increasing δz. This leads to a gradient in phase shift that might be well approximated by a linear dependence for $\delta z \to \infty$ (see Fig. 4.11a). α again shows no signs of convergence, which also would lead to rather large phase shifts for small voltages U as in *Area A*.

In Eq. 4.53 a fit parameter γ has also been introduced for *Area A*, where it adds a linear dependence on x. γ shows some dependence on the mesh size, but as one would not expect such a dependence we will consider it as an artifact of the numerical evaluation of the FEM data and neglect it in further calculations in Chap. 5. In *Area B* γ represents a virtual radius of the ring electrode around *Area A* and increases with increasing mesh size. The increment of β and γ cause the phase shift in *Area B* to approach a linear behavior.

In order to regard potential effects caused by variations in cell size we have used the mesh generator's capabilities of switching to different algorithms and size parameters. In doing so we have chosen similar settings for $i \in [2, 3, 4]$, whereas we have used a different routine for $i = 5$, where the distribution of the size of the mesh elements has been modified such that in the vicinity of small features in the mesh boundary smaller mesh cells are generated compared to regions in the vicinity of large features in the boundary. From the evaluation of data (see Figs. 4.11b and 4.11c) no extraordinary influence is noticeable.

Therefore one can conclude that the shape of the phase shift can be qualitatively described by the fit models f (see Eq. 4.44 and 4.48), but the numerical values obtained for α, β and γ in Sec. 4.3.3 will not be verifiable experimentally.

4.3.4.3. Charging Effects

In Sec. 7.2 we will encounter strong deviations from the expected intensity distributions predicted in Chap. 5. As is pointed out in Sec. 7.2 these deviations are most likely caused by electrostatic charging in the twin aperture. Therefore we have decided to include static negative charges in the insulating layers between the metallic layers to which boundary conditions are applied.

As the determination of the actual charge density would be too much of an effort for a simple quantitative demonstration and due to the fact that we want to avoid charging at all we will simply assume a charge density of 10 electrons per mesh cell. This value was chosen rather arbitrarily; the sole intention of this subsection is to visualize the problem in the previously established mathematical framework.

In the FEM calculation of the phase shifting potential we assumed that the charge density was located in the layer between ring electrodes and top layer (indicated in Fig. 4.12; orientation of twin aperture identical to Figs. 4.4b and 3.4). These electrons are assumed to be stationary. Fig. 4.12 shows the calculated potential in free space in the range [-10 mV, 10 mV] for an applied potential $U = 10\,\mathrm{V}$. In *Area A* (right hand side) the potential follows approximately the behavior we have modeled in Sec. 4.3.3. In *Area B* (left hand side) the potential shows a noticeable influence due to the distribution of negative charges.

The influence of such a potential on the phase shift is shown in Fig. 4.13. For very low potentials $U \lesssim 0.2\,\mathrm{V}$ the phase shift has a negative sign and a hyperbolical shape in both areas.

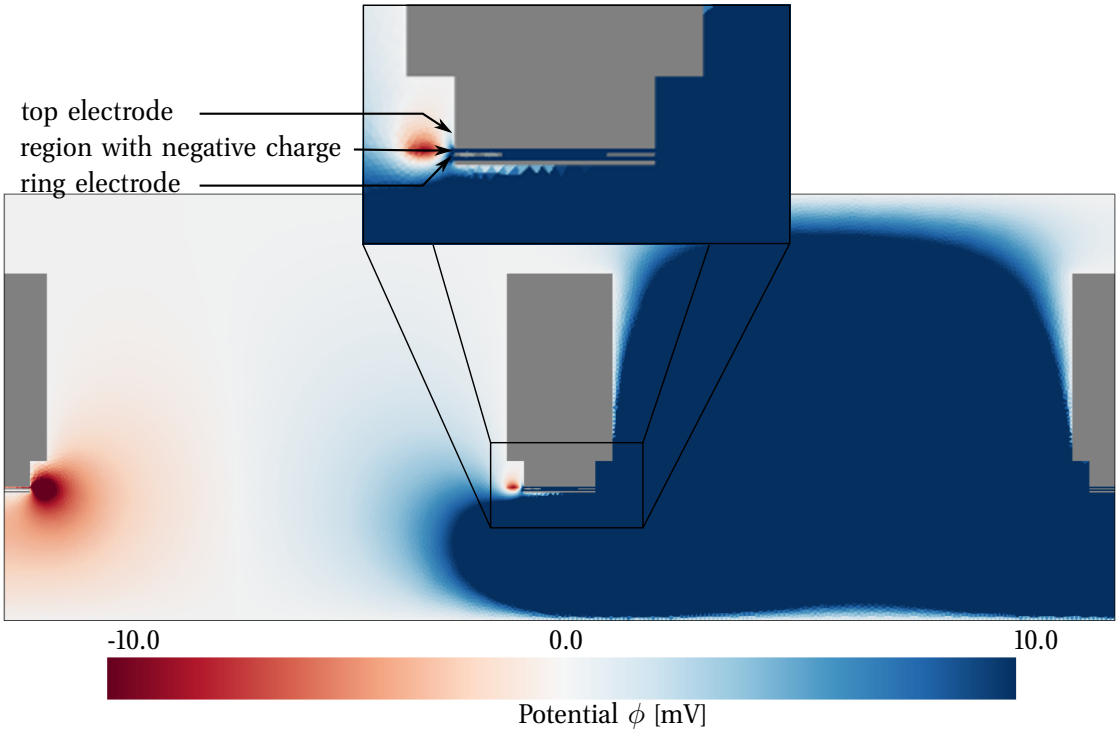

Figure 4.12.: Electrostatic potential in free space caused by Boersch phase plate and a layer of electrons pinned into the insulating layer between top electrode and ring electrodes. The applied potential to the right ring electrode is $U = 10\,\mathrm{V}$. The colormap has been clipped to show the potential only in the range [-10 mV, 10 mV].

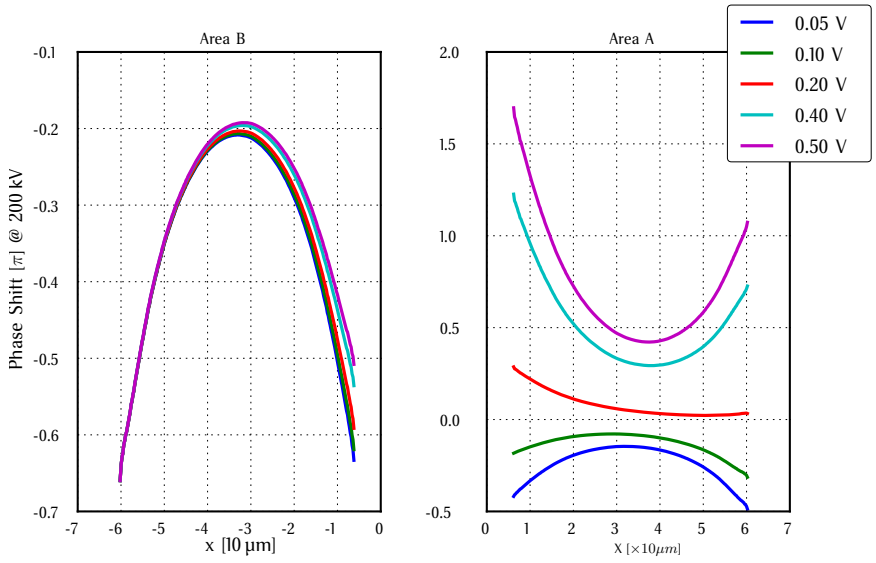

Figure 4.13.: Cross section along x axis showing phase shift for 200 keV electrons for different applied potentials. For a plot containing all potentials in the range [0.05 V, 10 V] see Fig. A.3. **Right**: Phase shift for beams travelling through the ring electrode (*Area A*). **Left**: Phase shift for beams travelling through the aperture where commonly no potential is expected (*Area B*).

In *Area A* the shape of the phase shift quickly approaches the known behavior encountered in Sec. 4.3.3. One might consider the effects due to the charge density as a negative offset to the applied potential. Due to the symmetry of the Laplace equation a change of sign of the voltage U simply causes a change of sign of the phase shift. Further effects on the phase shift due to the inhomogeneous distribution of charge are negligible — presumably due to the investigation of a two dimensional cut plane instead of a three dimensional volume.

For higher potentials the phase shift in *Area B* shows a more complex behavior. Due to the asymmetry of the applied voltage relative to the aperture hole of *Area B* the initial phase shift (shape of hyperbolical cosine) due to the charge distribution is superimposed with the hyperbolically decreasing phase shift known from previous calculations (see also Fig. A.3). This imprints a more complex phase shift on a transmitted wave.

As it is rather difficult to estimate the actual number of electrons contributing to a charging effect and deduce an accurate two dimensional model from the available simulated cross sections we will not pursuit this topic by this kind of simulation; instead we will focus on the attempt to avoid charging in an experimental setup (see Sec. 5.3).

4.4. Summary

In this chapter we have determined fit models for the phase shift of a Boersch phase plate and twin aperture.

The phase shift of the central ring electrode of the Boersch phase plate can easily be approximated as independent of the x and y coordinate, but the phase shift in the outer ring can hardly be neglected. As the Zach phase plate (see Sec. 3.1.2) explicitly relies on a strong gradient in the phase shift it seems likely that the discovered phase shift outside of the ring electrode has little distortive influence on phase contrast microscopy applications. An experimental evaluation of this influence shall not be subject to this work.

The phase shift of a twin aperture in *Area A* is described by a hyperbolic cosine which flattens with increasing free space above and below the twin aperture. The phase shift in *Area B* has considerable magnitude and will have to be regarded in calculations in Chap. 5.

5. Electron optical numerical calculations

After the description of the principal idea of the twin aperture setup in Chap. 2 and the theoretical investigation of the characteristics of Boersch phase plates in Chap. 4 this chapter presents numerical calculations based on Fourier optics and Monte Carlo simulations. With the help of these techniques the wave function of an electron probe and the penetration depth of primary electrons shall be determined.

5.1. Fundamentals of Electron Optics

Fourier optics is the study of classical optical systems using Fourier transforms and can be seen as the dual of the Huygens-Fresnel principle, in which waves are regarded as a superposition of expanding spherical waves which radiate outward from actual (physically identifiable) current sources via a Green's function[89] relationship.

A Green's function is an integral kernel that can be used to solve an inhomogeneous differential equation with boundary conditions. It serves roughly an analogous role in partial differential equations as do Fourier series in the solution of ordinary differential equations[89].

In Fourier optics on the other hand waves are regarded as plane waves or superpositions of such. A curved phase front may be synthesized from plane wave phase fronts oriented in different directions in space or — more conveniently — a phase term multiplied onto the wave. Far from its sources an expanding spherical wave is locally tangent to a planar phase front (a single plane wave out of the infinite spectrum), which is transverse to the radial direction of propagation[90].

For the calculations in Sec. 5.2 we are interested especially in the description of the focusing action of a lens in terms of Fourier optics. Given a plane wave ψ in the $z = z_0$ plane travelling a distance Δz along the z direction, then the wave in the plane $z = z_0 + \Delta z$ is given by[91]

$$\psi(x,\, y,\, z_0 + \Delta z) = \psi(x,\, y,\, z_0) \otimes \mathcal{P}_{\Delta z}(x,\, y) \tag{5.1}$$

$$\mathcal{P}_{\Delta z}(x,\, y) = \exp\left(-i\pi \frac{x^2 + y^2}{\lambda \Delta z}\right), \tag{5.2}$$

where λ is the electron wave length, $\mathcal{P}_{\Delta z}$ is the Fresnel propagator regarding the propagation of waves according to Huygens' principle and $\otimes$ is the convolution operator[92], which is given by

$$f(x) \otimes g(x) = \int_{-\infty}^{\infty} f(\tau) \cdot g(x - \tau)\, d\tau, \tag{5.3}$$

where f and g are functions of x.

To derive the Fourier optical formalism for the description of a lens action one would assume a point source at a distance Δf in front of a thin lens and propagate it into the lens plane

$$\psi(x,\, y\; z_0 + \Delta f) = \delta(x,\, y) \otimes \mathcal{P}_{\Delta f}(x,\, y) = \exp\left(-i\pi \frac{x^2 + y^2}{\lambda \Delta f}\right), \tag{5.4}$$

which is a quadratic approximation to the wave field of a spherical wave diverging from the object point[91]. From Eq. 5.4 we can see a convention used in the description of phase fronts; a *negative* valued exponential describes a *diverging* wave, whereas the opposite sign denotes a *converging* wave.

In analogy to light optics a focusing phase term is added to the wave function in the lens plane. Additionally we will regard the presence of an aperture by applying an aperture transmission function A to the lens plane. Thus the wave function ψ_1 in the lens plane is given by

$$\psi_1(x,\, y) = \exp\left(-i\pi \frac{x^2 + y^2}{\lambda \Delta f}\right) \cdot A \cdot \underbrace{\exp\left(i\pi \frac{x^2 + y^2}{\lambda f}\right)}_{\text{lens action}}. \tag{5.5}$$

As we are finally interested in the formation of an electron probe for STEM the wave function in the lens plane (see Eq. 5.5) is propagated to the back focal plane (BFP) at a distance f

$$\begin{aligned} \psi_2(x,\, y) =& \psi_1(x,\, y) \otimes \mathcal{P}_f(x,\, y) \\ =& A \cdot \exp\left(-i\pi \frac{x^2 + y^2}{\lambda \Delta f} + i\pi \frac{x^2 + y^2}{\lambda f}\right) \otimes \exp\left(-i\pi \frac{x^2 + y^2}{\lambda f}\right), \end{aligned} \tag{5.6}$$

where ψ_2 is the wave function in the BFP. Assuming that the source is approximately in the front focal plane of the lens ($\Delta f \approx f$) then Eq. 5.6 simplifies to

$$\psi_2(x,\, y) = \frac{i}{\lambda f} \mathcal{F}(\psi_1(x,\, y)), \tag{5.7}$$

where $\mathcal{F}$ is the Fourier transform operator. Thus regarding STEM we have the required formalism for the description of an electron probe in dependence of an aperture transmission function. The interested reader can find more information on Fourier optics and transforms e.g. in Refs. [42, 55, 91, 93–98].

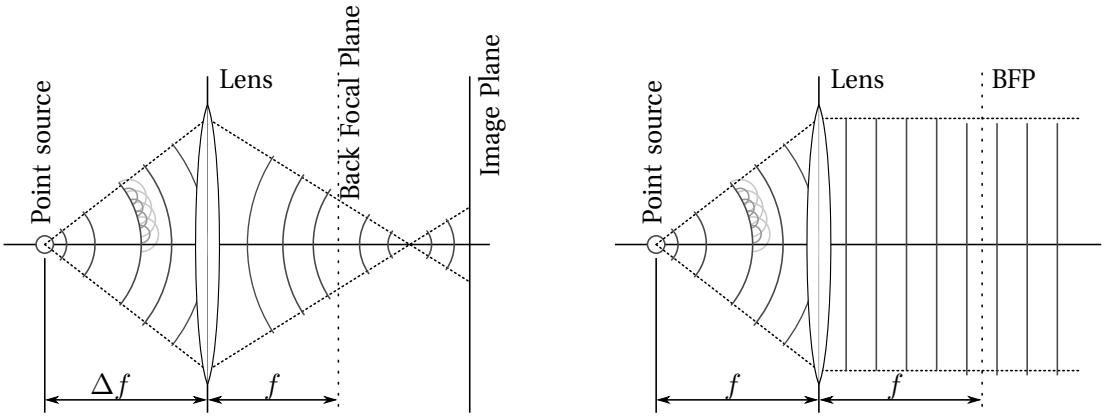

(a) $\Delta f > f$ (b) $\Delta f = f$

Figure 5.1.: Schematic ray and wave diagram for two different cases: $\Delta f \neq f$ and $\Delta f = f$. A point source (indicated by circle on the left) emits a spherical wave. The dark dotted lines denote the rays that pass at a distance equal to the aperture radius through the lens. Inside these rays the phase fronts have been indicated by arcs. At one section of a phase front the Huygens principle has been illustrated by some elemental spherical waves originating from adjacent points on the phase front.

5.2. Wave Function of Electron Probe in Scanning Mode

In case of a focused beam in the sample plane the sample plane coincides approximately with the back focal plane (BFP) of the condenser lens system assuming an incident plane wave. Thus the wave function of the electron probe in the sample plane is given by[94] the Fourier transform of the wave function in the front focal plane (FFP) of the condenser system multiplied with the transmission function of the twin aperture.

We assume for the calculations in this section an incident coherent plane wave. For the analytical approach we will also assume an ideal microscope neglecting any aberrations of the optical system. Lastly we apply the weak lens approximation onto the phase plate's ring electrodes, meaning that the potential applied to the ring electrode is so weak that it does not influence the path of an electron passing through the aperture.

In the previous chapter we have investigated the phase shifts φ_i caused by electrostatic ring electrodes onto electron waves travelling through the rings. Firstly we will use the common assumption[5] of constant phase shifts φ_i in the analytical approach in Sec. 5.2.1. Afterwards we will introduce non-constant phase shifts $\varphi_i(\vec{q})$ and aberrations in a numerical approach.

The wave function ψ_{ap} in the condenser aperture plane is given by

$$\psi_{ap}(\vec{x}) = \mathrm{A}\left(\vec{x} - \vec{d}_2\right) \cdot e^{-i\varphi_2} + \mathrm{A}\left(\vec{x} - \vec{d}_1\right) \cdot e^{-i\varphi_1} \tag{5.8}$$

$$\text{with } \mathrm{A}(\vec{x}) = \begin{cases} 1 & \text{for} \quad |\vec{x}| \leq R \\ 0 & \text{else} \end{cases}, \tag{5.9}$$

where $\vec{x}$ is a two dimensional vector in the aperture plane, A is the aperture function, $\vec{d}_i$ are displacements of the apertures away from the center of the plane, R is the aperture radius and

φ_i, $i = 1, 2$, are the phase shifts applied by the Boersch phase plates.

In the theoretical description of the electron probe in the sample plane we are following the convention of using Fourier space coordinates $\vec{q}$ in the condenser plane[42,91,94]. Therefore Eq. 5.8 needs to be rewritten by using the transformation

$$\vec{q} = \frac{\vec{x}}{\lambda f} \tag{5.10}$$

$$\tan(\alpha) = \frac{R}{f} \tag{5.11}$$

$$\Rightarrow \vec{q} = \frac{k \tan(\alpha)}{R} \vec{x}, \tag{5.12}$$

where λ is the electron wave length, $k = \lambda^{-1}$ the wave number, f is the focal length of the condenser lens system and α is the convergence semi-angle (see Sec. 7.1) to which we will refer in the following simply as convergence angle. Thus the aperture transmission function A reads in Fourier space coordinates

$$\mathrm{A}(\vec{q}) = \begin{cases} 1 & \text{for} \quad |\vec{q}| \leq k \tan(\alpha) \\ 0 & \text{else} \end{cases} . \tag{5.13}$$

Using Eq. 5.11 the focal length f of the condenser system has been replaced with the convergence angle α which is more easily accessible through experiments (see Sec. 7.1). As α is of the order of several mrad the small angle approximation $\tan(\alpha) \approx \alpha$ is applicable and will be used in Sec. 5.2.1. Furthermore we introduce the angles of incidence β_i, which are defined by the displacements $\vec{d_i}$ of the aperture holes from the optical axis.

Fig. 5.2 illustrates the definition of the convergence angle α[55] (left hand side) and incidence angle β (right hand side) in a simplified model of the condenser lens system, in which the entire lens system is treated like a single lens with focal length f[98]. Thus the convergence angle of an aperture with radius R is given by the simple trigonometric relation in Eq. 5.11. Analogously the incidence angle relative to the optical axis is defined as

$$\tan(\beta) = \frac{d}{f}. \tag{5.14}$$

On first sight a translation d of the aperture from the optical axis would result in a reduction of the convergence angle, but as we are interested in the Fourier transform of a function (see Eq. 5.16) containing α, a translation d of the aperture will only introduce a phase factor[95,99] to the Fourier transform. Thus the wave function in the aperture plane ψ_{ap} can be written in the form

$$\begin{aligned} \psi_{ap}(\vec{q}) =& A\left(\vec{q} - \frac{1}{\lambda f}\vec{d_2}\right) \cdot e^{-i\varphi_2} + A\left(\vec{q} - \frac{1}{\lambda f}\vec{d_1}\right) \cdot e^{-i\varphi_1} \\ =& A\left(\vec{q} - \vec{k}_2 \tan(\beta_2)\right) \cdot e^{-i\varphi_2} + A\left(\vec{q} - \vec{k}_1 \tan(\beta_1)\right) \cdot e^{-i\varphi_1}, \end{aligned} \tag{5.15}$$

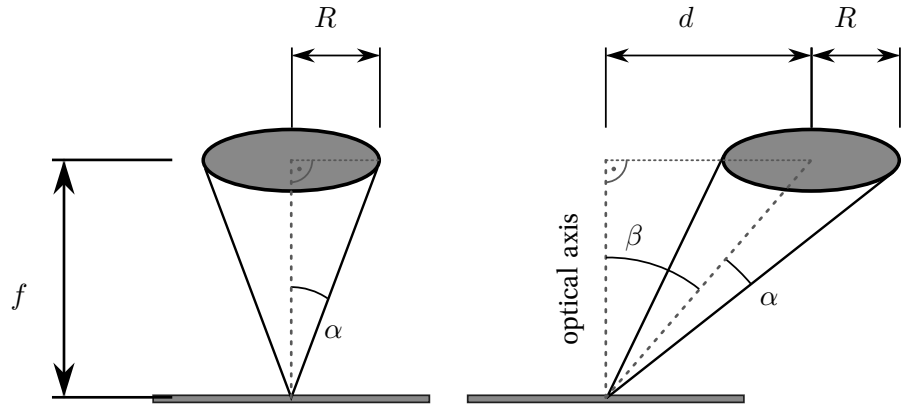

Figure 5.2.: Simplified model of the condenser lens system illustrating the transformation of aperture radius R and displacement d into angular quantities α and β. The convergence semi-angle α is experimentally accessible and in the simple model related to R and f. The properties of the Fourier transform state that a displacement of the function, that is to be transformed, only results in a phase term. As shown on the right hand side this displacement can be described by a tilt angle β.

where the displacements $\vec{d}_i$ have been replaced by a vectorial quantity $\vec{k}_i$. The absolute value thereof is the wave number k and its direction is dependent on $\vec{d}_i$.

The wave function ψ_{sp} in the specimen plane is the Fourier transform of ψ_{ap} (see Eq. 5.15) and thus given by

$$\begin{aligned}\psi_{sp}(\vec{x}) =& \mathcal{F}\left(A\left(\vec{q}-\vec{k}_2\tan(\beta_2)\right)\cdot e^{-i\varphi_2} + A\left(\vec{q}-\vec{k}_1\tan(\beta_1)\right)\cdot e^{-i\varphi_1}\right)\\ =& \mathcal{F}\left(A\left(\vec{q}\right)\cdot e^{-i\varphi_2}\right)\cdot e^{-2\pi i\tan(\beta_2)\vec{k}_2\cdot\vec{x}}\\ &+ \mathcal{F}\left(A\left(\vec{q}\right)\cdot e^{-i\varphi_1}\right)\cdot e^{-2\pi i\tan(\beta_1)\vec{k}_1\cdot\vec{x}},\end{aligned} \tag{5.16}$$

where $\vec{x}$ is a two dimensional vector in real space coordinates in the sample plane and $\mathcal{F}$ is the Fourier transform operator. Due to the tilt of the incidence angles β_i the Fourier transforms introduce phase factors that will cause an interference fringe pattern.

For all plot representation of the wave function ψ_{sp} in this chapter we will follow a common normalization convention. After calculation of the wave function it is multiplied with a normalization factor N, such that

$$\int N\cdot|\psi_{sp}(x,\,y)|^2\;dx\,dy = 1, \tag{5.17}$$

where x and y are the components of $\vec{x}$. In case, where line scans are not taken from the 2D data, but calculated directly (e.g. Sec. 5.2.1), the normalization is performed only in one dimension accordingly; thus the numeric values of the normalized intensities can differ between 2D and 1D plots.

Fixed parameters		
λ	R	d_i
2.5 pm	29 µm	$\pm$33.2 µm

Table 5.1.: Parameter set used for all calculations in this section. f and α are functions of R as described in Sec. 7.1.

In the following subsections we will have a closer look at the wave function in the sample plane. First we will use an analytical approach in Sec. 5.2.1 by assuming $\varphi_i(\vec{q}) = const$ and an ideal microscope. Afterwards in Sec. 5.2.2 we will use numerical methods to calculate the Fourier transform. In doing so we can regard $\varphi_i(\vec{q}) \neq const$ as well as aberrations. For all subsequent calculations in this section we will assume the parameters given in Table 5.1 and a coherent plane wave in the FFP of the condenser lens system.

5.2.1. First Approximation — Constant Phase Shift

In this analytical approach we will start by applying the small angle approximation to Eq. 5.16 and choose $\varphi_1 = 0$ and $\varphi_2 = \pi/2$

$$\begin{aligned}\psi_{sp}(\vec{x}) =& \mathcal{F}\left(A\left(\vec{q}\right)\right) \cdot e^{-2\pi i \beta_2 \vec{k}_2 \cdot \vec{x} - i\pi/2} + \mathcal{F}\left(A\left(\vec{q}\right)\right) \cdot e^{-2\pi i \beta_1 \vec{k}_1 \cdot \vec{x}} \\ =& \frac{\mathrm{J}_1\left(2\pi k \alpha |\vec{x}|\right)}{2\pi k \alpha |\vec{x}|} \times \left(e^{-2\pi i \beta_2 \vec{k_2} \cdot \vec{x} - i\pi/2} + e^{-2\pi i \beta_1 \vec{k_1} \cdot \vec{x}}\right), \end{aligned} \tag{5.18}$$

where the Fourier transforms of the annular apertures are Airy disks and J_1 is the Bessel function of the first kind and first order. As the Bessel function is a real valued function that only defines an envelope for the interference pattern caused by the two beams the phase difference $\Delta\phi$ between the two incoming waves in the specimen plane is given by the expression

$$\Delta\phi(\vec{x}) = 2\pi \left(\beta_2 \vec{k}_2 - \beta_1 \vec{k_1}\right) \cdot \vec{x} + \frac{\pi}{2}. \tag{5.19}$$

Thus, as can be seen in Eq. 5.19, the phase difference in the sample plane only depends on the aperture displacements $\vec{d_i} \equiv \beta_i \vec{k_i}$ and applied phase shift φ_i. To simplify matters we assume that the displacement vectors $\vec{d_i}$ are parallel to the x axis, which means that the phase difference only varies along the $\hat{x}$ axis (for orientation of axes refer to Fig. 2.3 on page 7).

Fig. 5.3 shows two dimensional plots of the amplitude, intensity (see Eq. 5.18) and phase difference (see Eq. 5.19) in the sample plane for $\varphi_2 = 0$. For α and β_i experimentally derived values (see Sec. 7.1) have been used.

$$\alpha = \quad 1.65\,\mathrm{mrad} \tag{5.20}$$

$$\beta_i = \pm 2.03\,\mathrm{mrad} \tag{5.21}$$

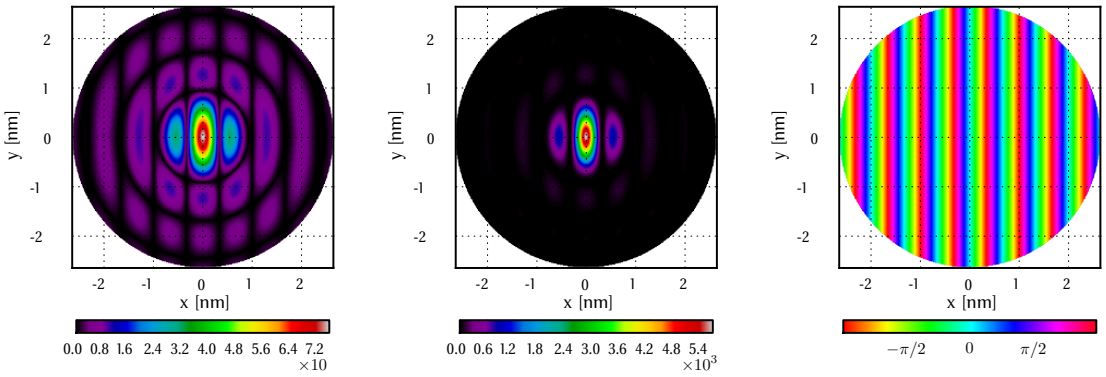

(a) Amplitude (b) Intensity (c) Phase Difference

Figure 5.3.: 2D images of amplitude $|\psi_{sp}|$, intensity $|\psi_{sp}|^2$ and phase difference $\Delta\phi$ for $\varphi_1 = 0$ and $\varphi_2 = 0$.

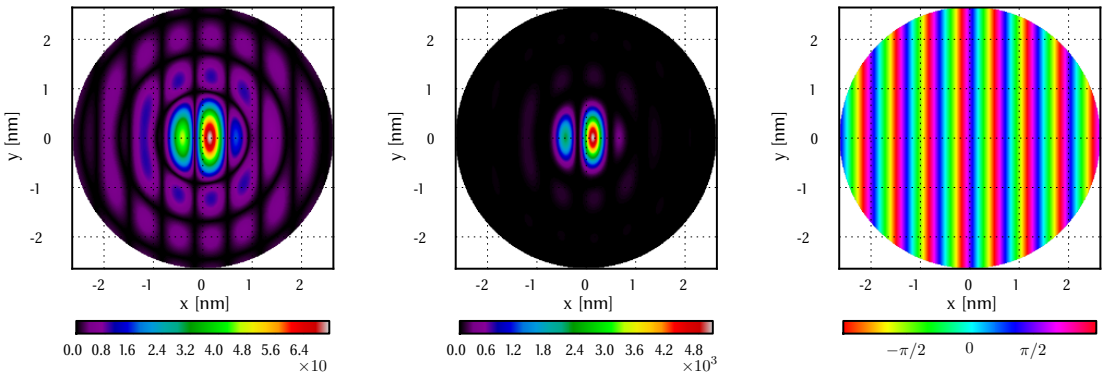

(a) Amplitude (b) Intensity (c) Phase Difference

Figure 5.4.: 2D images of amplitude $|\psi_{sp}|$, intensity $|\psi_{sp}|^2$ and phase difference $\Delta\phi$ for $\varphi_1 = 0$ and $\varphi_2 = \pi/2$.

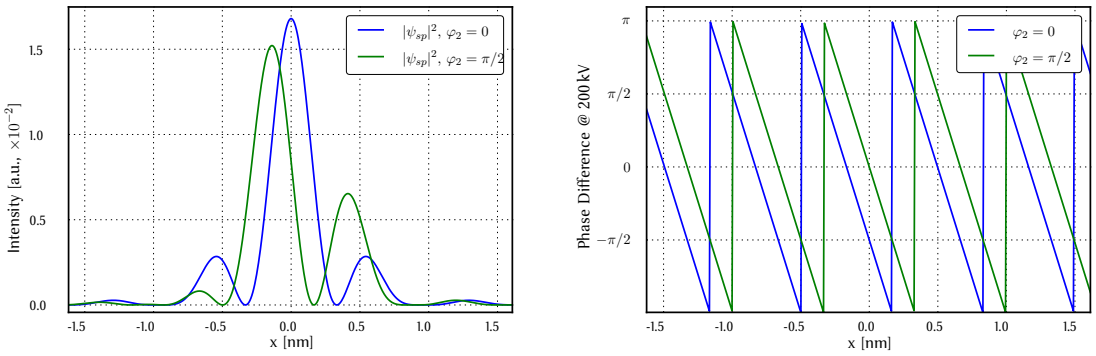

(a) Intensity (b) Phase Difference

Figure 5.5.: Line scans of intensity and phase difference 2D images (see Figs. 5.3 and 5.4) along the $y = 0$ axis.

As expected from general optics each aperture causes the wave function originating from it to take the shape of an Airy disk. Due to the coherent illumination of the apertures and the staticity of the Fourier transform the displacement of the apertures along the x axis leads to an interference pattern, which is periodic along the x axis, in the superposition of the two waves.

Eq. 5.19 and Fig. 5.3 explain the effect of changing the phase shift φ_2 to $\pi/2$. As one can see Eq. 5.18 is written in the polar representation of complex numbers thus a changing φ_i affects only the phase term, which only affects the position of the fringes in the interference pattern; this is described by Eq. 5.19.

This simple model predicts a sub-nm spot size and an amplitude-modulated plane wave passing through the sample plane. Due to the different incidence angles of the two partial waves assembling the electron probe ψ_{sp} the phase shift between those partial waves shows a constant gradient, which is shifted by the applied phase shift φ_2. Fig. 5.5 shows line scans along the $y = 0$ axis of the intensity and phase shift for both previous cases in order to visualize the effects of the phase shift for better comparison.

In this scenario we have investigated constant phase shifts. The sign of the phase shift φ_2 has virtually no significance for the intensity distribution except that the shift points into the opposite direction. As the analytical approach of the problem was subject to previous works[34,100] we will proceed without further treatment of this case by investigating a more realistic scenario by numerical means.

5.2.2. Second Approximation — Hyperbolic Cosine

In Chap. 4 we have simulated the electrostatic potential of the ring electrodes associated with each aperture hole of the twin aperture and derived a model for the phase shift φ_i that is to be expected upon application of a potential to one ring electrode. These calculations show that the treatment of the phase shifts as constants is quite inaccurate for the twin aperture. Therefore we will regard the phase shift models $\varphi_{U,i}(\vec{q})$ in Eq. 5.16 and treat each term of the sum separately.

Following the nomenclature of Chap. 4 we will call the wave passing through the active phase plate (Area A) ψ_A, which suffers a phase shift $\varphi_{U,2}$. Accordingly the wave passing through Area B will be called ψ_B. Thus Eq. 5.16 reads

$$\begin{aligned}
\psi_{sp}(\vec{x}) =& \mathcal{F}\left(\mathrm{A}\left(\vec{q} - \vec{k}_2\tan(\beta_2)\right)\cdot e^{-i\varphi_{U,2}(\vec{q})} + \mathrm{A}\left(\vec{q} - \vec{k}_1\tan(\beta_1)\right)\cdot e^{-i\varphi_{U,1}(\vec{q})}\right) \\
=& \mathcal{F}\left(\psi_A(\vec{q})\cdot e^{-2\pi i\tan(\beta_2)\vec{k}_2\cdot\vec{x}} + \mathcal{F}\left(\psi_B(\vec{q})\right)\cdot e^{-2\pi i\tan(\beta_1)\vec{k}_1\cdot\vec{x}}, \qquad (5.22)\right. \\
\psi_A(\vec{q}) =& \mathrm{A}\left(\vec{q}\right)\cdot e^{-i\varphi_{U,2}(\vec{q})} \qquad (5.23) \\
\psi_B(\vec{q}) =& \mathrm{A}\left(\vec{q}\right)\cdot e^{-i\varphi_{U,1}(\vec{q})} \qquad (5.24)
\end{aligned}$$

Due to the radial symmetries of the aperture holes the Fourier transform is advantageously performed in polar coordinates. The Fourier transform operator $\mathcal{F}$ reads in polar coordinates[96,97]

$$\mathcal{F}\left(f(r,\,\theta)\right) = \int_0^{2\pi}\int_0^{\infty} r\; f(r,\,\theta)\cdot e^{-irq\cos(\theta-\phi)}\; dr\; d\theta \qquad (5.25)$$

and simplifies for radial symmetric functions $f(r) = \mathrm{A}(r) \cdot g(r)$, that contain an aperture function A[97] (compare Eq. 5.9), to

$$\mathcal{F}\left(f(r)\right) = 2\pi \int_0^R r\ g(r)\mathrm{J}_0(2\pi r q_r)\ dr, \tag{5.26}$$

where R is the delimiting aperture radius and J_0 is the Bessel function of the first kind and order zero.

In the following numerical calculations we will use the modeled phase shifts φ_i determined from the FEM calculations for the mesh named twin_ap_2D_X5_5 (for numeric values see Table A.1) as this model regards the most free space below and above the twin aperture. Thus we deem this model to best describe the situation. The interested reader can find the results of the following calculations for the model twin_ap_2D_X5, which can be thought of as worst case model — neglecting twin_ap_2D_X1 — in the appendix Sec. A.4.

5.2.2.1. Aberration-free Lens

As we have seen in Sec. 4.3.3 the phase shift φ_2 of the active phase plate is also radial symmetric to the center of the aperture. Thus the Fourier transform of ψ_A can be written in the easy form of Eq. 5.26

$$\mathcal{F}(\psi_A(q_r)) = 2\pi \int_0^{k_2 \tan(\alpha)} q_r\ e^{-i\varphi_{U,2}(q_r)}\mathrm{J}_0(2\pi r q_r)\ dq_r, \tag{5.27}$$

$$\varphi_{U,2}(q_r) = \alpha(U) + \cosh(\beta(U) \cdot q_r) - 1 \tag{5.28}$$

$$\alpha(U) \propto U \tag{5.29}$$

$$\beta(U) \propto \mathrm{acosh}(U + 1) \tag{5.30}$$

where for $\varphi_{U,2}$ the model from Eq. 4.44 is inserted. $\alpha(U)$ and $\beta(U)$ are the model functions determined in Sec. 4.3.3.1[a], U is the applied potential. For a full list of geometry dependent parameters for the model functions see Table A.1. Due to the radial symmetry the coordinate x in Eq. 4.44 is replaced by the radial component q_r (Eq. 5.28). By numerical integration the radial component of the Fourier transform is calculated. By means of an interpolation algorithm the Fourier transform in two dimensions is constructed and multiplied with the phase term due to the aperture displacement.

Onto the other wave ψ_B, which suffered no phase shift in the previous case, also a phase shift is applied due to stray potentials. In Sec. 4.3.3.2 we have assumed that this stray potential is radial symmetric with respect to the center of the adjacent aperture hole. Thus we cannot calculate the simplified Fourier transform from Eq. 5.26 as we have to regard a linear translation $\vec{t}$ in polar coordinates in the Fourier transform $\mathcal{F}(\psi_B)$ (see Fig. 5.6), which breaks the radial

[a] Do not confuse the convergence and incidence angles α and β with the model functions $\alpha(U)$ and $\beta(U)$.

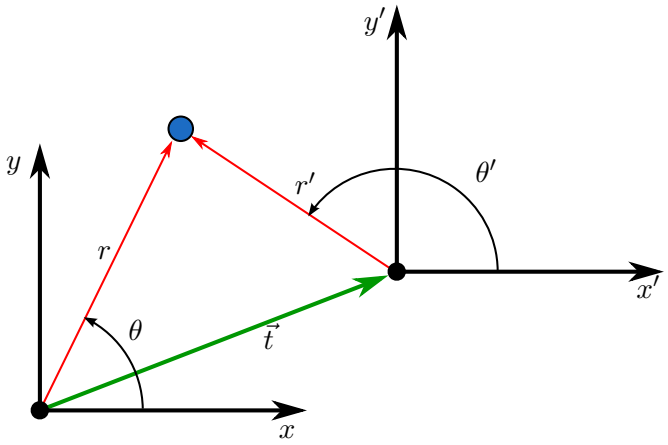

Figure 5.6.: Illustration of linear translation vector $\vec{t}$ in cartesian and polar coordinates.

symmetry. A linear translation in cartesian coordinates from $(x,\, y)$ to $(x',\, y')$ is given by the simple expression

$$(x,\, y) + \vec{t} = (x',\, y') = (x + x_0,\, y + y_0), \tag{5.31}$$

where $\vec{t} = (x_0, y_0)$ is the translation vector. Using simple conversion formulae the translated coordinate system $(r',\, \theta')$ can be written in terms of the linear translation vector $\vec{t} = (r_0,\, \theta_0)$ in polar coordinates performing the translation $(r,\, \theta) + \vec{t} = (r',\, \theta')$ as

$$\begin{aligned} r' =& \sqrt{(x + x_0)^2 + (y + y_0)^2} \\ =& \sqrt{r^2 + r_0^2 + 2 r r_0 \cos(\theta_0 - \theta)} \qquad (5.32) \\ \theta' =& \arccos\left(\frac{r\cos(\theta) + r_0\cos(\theta_0)}{r'}\right), \qquad (5.33) \end{aligned}$$

where $\vec{t} = (r_0,\, \theta_0)$ is the translation vector in polar coordinates. Thus we can regard the translated symmetry center of the phase shift $\varphi_{U,1}$ in the Fourier transform of the second wave by writing

$$\mathcal{F}(\psi_B(q_r,\, q_\theta)) = \int_0^{2\pi} \int_0^{k\tan(\alpha)} q_r \cdot e^{-i\varphi_{U,1}(q_r')+2\pi r q_r \cos(\theta - q_\theta)}\, dq_r\, dq_\theta \tag{5.34}$$

$$q_r' = \sqrt{q_r^2 + t_r^2 + 2q_r t_r \cos(t_\theta - q_\theta)} \tag{5.35}$$

$$t_r = \tan(\beta_1)|\vec{k}_1| + \gamma(U) \tag{5.36}$$

$$t_\theta = k_{1,\theta} \tag{5.37}$$

$$\varphi_{U,1}(q_r) = \alpha(U) + \frac{\beta(U)}{(q_r - \gamma(U))^2} \tag{5.38}$$

$$\alpha(U) \propto U \tag{5.39}$$

$$\beta(U) \propto U \tag{5.40}$$

$$\gamma(U) = const, \tag{5.41}$$

where $\alpha(U)$, $\beta(U)$ and $\gamma(U)$ are model functions determined in Sec. 4.3.3.2 and U is the potential applied to the adjacent phase plate. For a full list of geometry dependent parameters of the model functions see Table A.1. q_r' is the radial coordinate in the translated coordinate system. $\vec{t} = (t_r,\, t_\theta)$ is the translation vector. Fortunately this translation preserves a mirror symmetry, which allows the calculation of the Fourier transform in the $y \geq 0$ half plane and mirroring of it down to the other half plane.

Fig. 5.7 shows the wave amplitude, intensity and phase difference. A comparison to the previous model shows — at first sight — no remarkable differences in amplitude or intensity. A direct comparison of Figs. 5.3c and 5.7c reveals a concentric ring system in the phase difference plot. Within these rings of finite width the phase difference shows a continuous peak of height $\approx \pi/2$.

As we know from Sec. 5.2.1 the radial component of the wave function — and thus the intensity — follows a Bessel function of the first kind J_1. Comparing the intensities of the analytical and numerical calculations (see Fig. 5.8) we can see that the numerical solution is following a Bessel function as well. Using this finding one can see that the radii of said rings in the phase difference plot (Fig. 5.7c) approximately coincide with the zeros of the Bessel function.

Bessel functions J_1 have a co-domain which includes values of opposite sign. Contrary thereto the wave function is written in polar notation of complex numbers; the mathematical definition of which allows only positive values for the radial component — which is dominated by a Bessel function. Thus the change in sign of the Bessel function becomes regarded in the azimuthal part of the complex value and results in a discrete phase transition of π at the zeros of the Bessel function. In mathematical terms this means that a wave function ψ having a Bessel function J_1 in its radial component is implicitly rewritten as

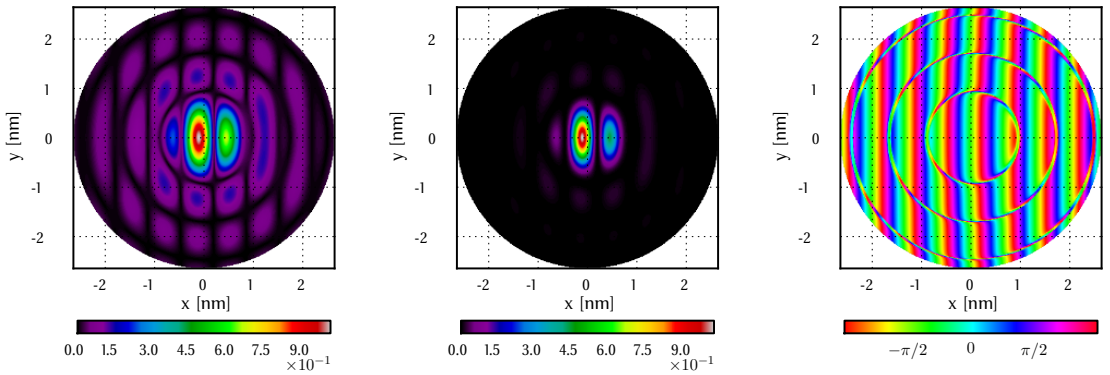

(a) Amplitude (b) Intensity (c) Phase Difference

Figure 5.7.: 2D images of amplitude $|\psi_{sp}|$, intensity $|\psi_{sp}|^2$ and phase difference $\Delta\phi$ for $\varphi_{U,i}(\vec{q})$.

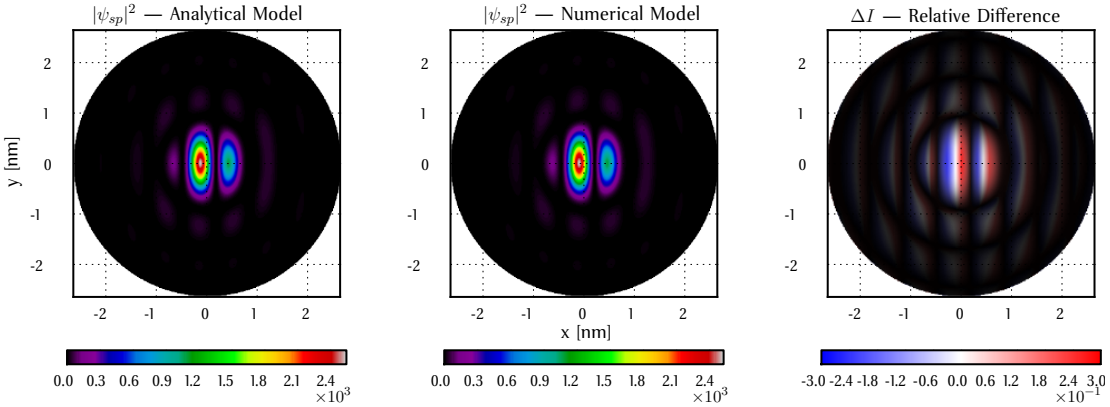

Figure 5.8.: Comparison between the intensity distributions of the simple model using constant phase shifts φ_i (**left** hand side, see Sec. 5.2.1) and a model based on potential dependent phase shifts $\varphi_{U,i}$ (**center**, see Secs. 5.2.2.1 and 4.3.3) in two dimensions. The **right** hand side plot shows the relative difference between those distributions overlaid with a black, semi-transparent filter derived from the sum of the two intensity distributions. The filter is scaled with a square root function, while the colorbar has been limited to the range [-30%, 30%]. See Fig. A.5 for plots regarding only the wave function ψ_B originating from *Area B*.

$$\psi \propto \mathrm{J}_1 \cdot e^{-i\varphi} \tag{5.42}$$

$$\propto |\mathrm{J}_1| \cdot e^{-i\mathrm{sgn}(\mathrm{J}_1)} \cdot e^{-i\varphi} \tag{5.43}$$

$$\mathrm{sgn}(x) = \begin{cases} 1 & \text{for } x > 0 \\ 0 & \text{for } x = 0 \\ -1 & \text{for } x < 0 \end{cases}, \tag{5.44}$$

where sgn is the sign function.

Fig. 5.9a shows the phase front of the partial wave ψ_B for $\varphi_1 = 0$ according to the analytical model. As we can see at the zeros of the Bessel function the phase front makes discrete jumps of π. In the phase difference plot these discontinuities are canceled out in the analytical framework resulting in a continuous phase difference.

When numerically investigating inhomogeneous phase shifts $\varphi_{U,i}(\vec{q})$ the phase front shows no longer discrete jumps, but reveals rings of finite width, in which the phase changes continuously by π (see Figs. 5.9b and 5.9c; best visibility in vertical direction). As the observant reader might notice the center of the ring system in Fig. 5.9b is slightly shifted away from the center of the plot $(0,\, 0)$ along the positive x direction, which also explains the stripe pattern in the relative difference ΔI plot of Fig. 5.8, to which we will refer again later. The interested reader can find intensity plots of ψ_B in Fig. A.5 illustrating the shifted entrance point of the beam originating from *Area B* in the sample plane (see also Fig. 5.10). The rather linear gradient in phase shift in *Area B* causes an additional tilt of the propagation direction of the electron wave and thus a shift of the wave function in the sample plane.

The shift of the wave function ψ_B in the sample plane and the non-constant phase shifts on both functions $\psi_{A/B}$ cause deviations from the discrete phase jumps at the zeros of the Bessel functions, which dominate the wave functions in the analytical theory. These deviations can in the best case give rise to transition areas of a finite size (see Fig. 5.9) or even change the shape of the ring structures defined by the zeros of the Bessel functions drastically (see Fig. A.8 for model `twin_ap_2D_X5`). Thus in the first case peak like features are introduced into the phase difference plots as shown in the line scan in Fig. 5.10.

As already stated, Fig. 5.8 shows a comparison between the intensity distribution for the analytical model (see Sec. 5.2.1) and the model derived in Sec. 4.3.3. The right hand side plot in the figure shows the relative difference ΔI between the two models, where the difference ΔI is calculated by

$$\Delta I = \frac{|\psi_{sp,hyper.}|^2 - |\psi_{sp,const.}|^2}{|\psi_{sp,const.}|^2}, \tag{5.45}$$

where $\psi_{sp,hyper.}$ is the wave function of the potential dependent model (see Eq. 5.35) and $\psi_{sp,const.}$ is the wave function for the constant phase shift model (see Eq. 5.18). For better visibility the plot of ΔI is overlaid with an inverse semi-transparent black colored plot scaling with the sum of the intensities of the incident waves. While a comparison of the intensity distributions by eye would suggest no difference in intensities ΔI reveals an alternating pattern, which is related to the previously found beam shift of ψ_B due to the newly regarded phase shift outside of the active ring electrode (see Sec. 4.3.3).

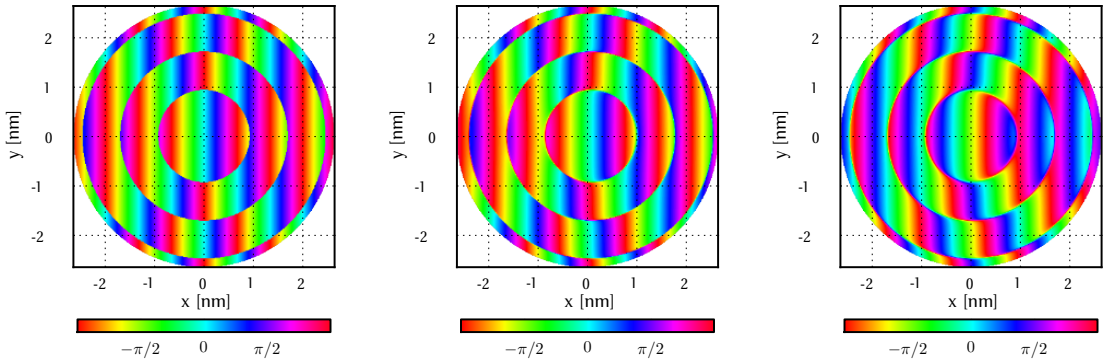

(a) Phase Front, ψ_B, analytical model.

(b) Phase Front, ψ_B, numerical model.

(c) Phase Front, ψ_A, numerical model.

Figure 5.9.: Phase fronts of the non-shifted wave originating from aperture displaced by d_1 of the analytical model (**left**), and both waves of the numerical model with phase shifts $\varphi_{U,i}$ as described in Sec. 4.3.3 (**center** and **right**). Phase fronts are the azimuthal component of the complex valued wave functions. In numerical calculations occur no phase jumps of π as in the analytical model for phase shifts $\varphi_{U,i} \neq 0$.

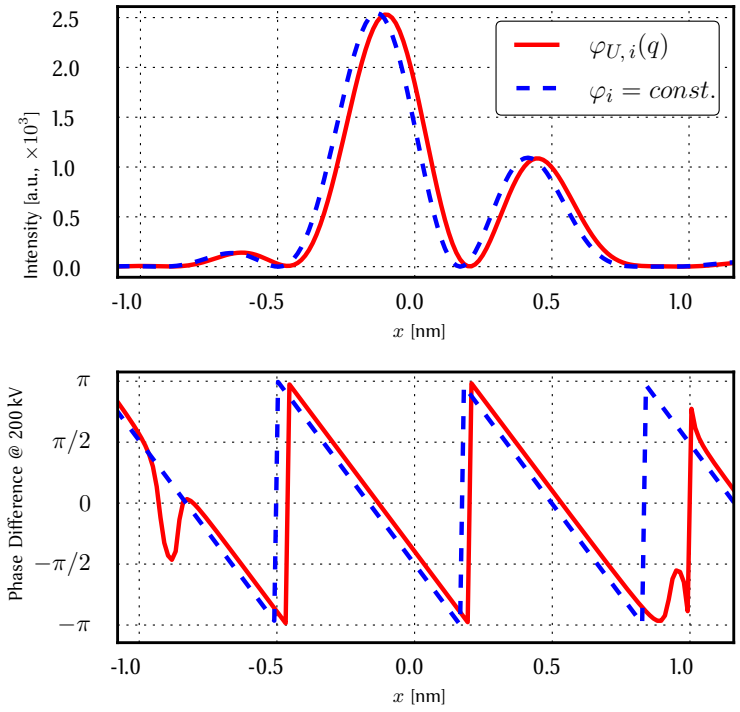

Figure 5.10.: Line scans along the $y = 0$ axis of the intensity distributions of Fig. 5.8 (**Upper** box) and phase difference (**Lower** box) between the incident beams for both cases.

As this alternating pattern in the relative difference is periodic in the x direction Fig. 5.10 shows a line scan across the intensity distributions of both models along the $y = 0$ axis. The **dashed blue** curve is the expected intensity distribution for constant phase shifts (compare Fig. 5.5), whereas the **continuous red** curve is the intensity distribution (see Eqs. 5.27 and 5.34) obtained for the non-constant model. Again one can see in the line scan that the intensity distribution is slightly shifted along the positive x direction. The calculation assumed a potential of 0.15 V with model "twin_ap_2D_X5_5" (see Table. A.1). As stated previously this shift is mainly caused by the rather linear gradient in the phase front of the wave ψ_B passing through the aperture in *Area B*.

The phase difference (in Sec. 5.2.1 called $\Delta\phi$, see Eq. 5.19) is correspondingly shifted. Furthermore at the minima of the wave function's amplitude $|\psi_{sp}|$ (approximately at ± 1 nm) the phase difference shows a peak — as previously mentioned — due to the shift of ψ_B. As seen in Fig. 5.9 these peaks appear in the transition area at the zeros of the Bessel function. The phase front gradients of the two incident partial waves have opposite signs due to the aperture displacements from the optical axis. This causes the linear gradient in the phase difference plot that is also observable in the analytical case (see Fig. 5.5). Due to the deformations of the phase front caused by the hyperbolically shaped phase shift and the additional phase term applied to the other wave, these waves do not converge into the same point as in the analytical case. This is observable in the line scan of the phase difference as these small peaks in the transition area have different sign.

In Sec. 5.1 the significance of the sign of phase shift terms has been highlighted. As the phase shift due to a negative potential would not change in form but only in sign we can take a quick look at the effect of such a change in phase shift. Fig. 5.11 shows line scans across the intensity distribution $|\psi_{sp}|^2$ for the analytical model and the numerical model for potentials $U = \pm 0.15$ V. The intensity distribution and phase difference plot for the negative potential have been flipped horizontally at the $x = 0$ axis in Fig. 5.11b. The intensity distribution matches the distribution for the positive potential within the accuracy of the used numerical methods. Due to the switching of the sign of the voltage U that was intended to achieve a phase shift of $\pi/2$ the green and red curves in the phase difference plot in Fig. 5.11a are offset approximately by π. As one can see the positions of the peaks in the phase transition region have changed as well, mainly because the wave ψ_B is now shifted along the negative x direction. Thus flipping of the phase difference plot for $U = -0.15$ V horizontally and vertically brings those peaks to an overlap just like the intensity distributions.

Thus we can conclude that in the absence of aberrations a sign-change of the potential results only in an horizontal flip at the optical axis when neglecting other effects in areas with low intensities. So far we have regarded phase shifts that are dependent on the position in the aperture plane. In the following subsection we will introduce the treatment of spherical and chromatic aberration in the calculations of Eq. 5.22.

5.2.2.2. Aberration-afflicted Lens

Common problems in the fabrication and usage of lenses in light and electron optics are imperfections of these lenses. These imperfections lead to a variety of aberrations, which are in detail explained in textbooks, e.g. Ref. [42]. In order to investigate the influence of these

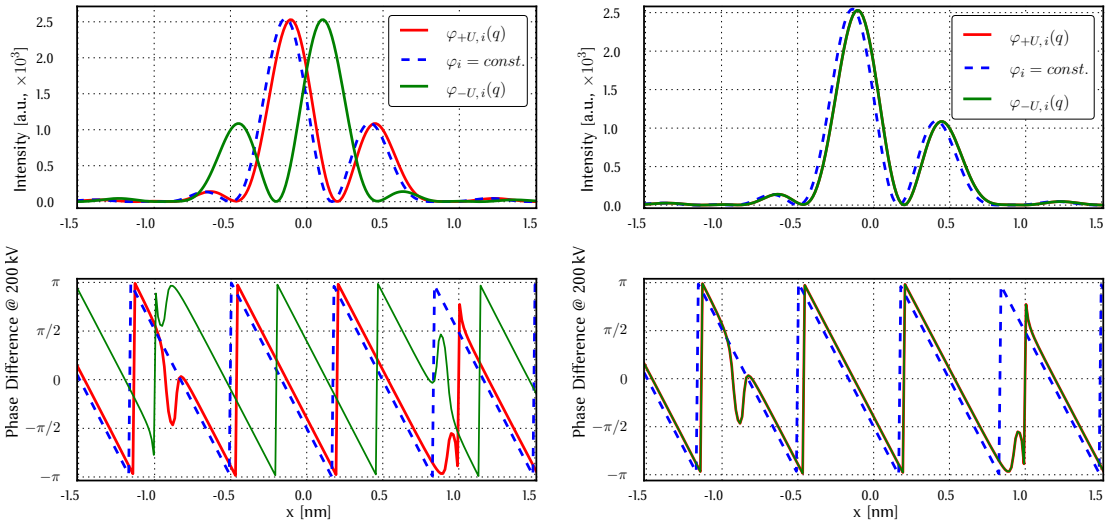

(a) Non-flipped (b) Flipped

Figure 5.11.: Line scans across intensity distributions. **Blue dashed** line: analytical model, **red continuous** line: $U = 0.15\,\mathrm{V}$, **green continuous** line: $U = -0.15\,\mathrm{V}$. The green curves have been flipped horizontally at the $x = 0$ axis to allow an easier comparison in subfigure **b**. The phase shift in subfigure **b** has been also flipped upside down. The intensities and resulting phase differences of the numerical model for potentials with different sign agree very well.

aberrations onto the cross-over formed by a twin aperture in the sample plane we will focus on the two most important types of aberrations: spherical and chromatic[91].

The effect of *spherical aberration* refers to rays leaving an axial object point at a large angle and being refracted too strongly by the outer zones of the lens. Thus these rays are brought to a focus before the Gaussian image plane[91]. This overfocusing behavior is described by an additional phase term $i\chi_s(\vec{q})$ introduced to the wave functions $\psi_{A/B}$ in the FFP or aperture plane (see Eq. 5.23 and 5.24). The term χ_s is given by[91,94]

$$\chi_s(\vec{q}) = \frac{1}{2}\pi C_s \lambda^3 |\vec{q}|^4, \tag{5.46}$$

where $C_s = 1.2\,\mathrm{mm}$ is the spherical aberration constant of the objective lens[b] as specified by the FEI company for Tecnai series TEMs.

Chromatic aberration refers to the dependence of the lens focal length on the wavelength of the radiation used, and hence on the electron energy. With polychromatic illumination, in-focus images are formed on a set of planes, one for each wavelength present in the illuminating radiation. The focusing error due to image formation by radiation of energy $V_0 - \Delta V$ must be considered with respect to the Gaussian image formed by radiation of energy V_0[91]. Thus we

[b] According to Ref. [94] one only regards C_s of the objective lens.

have to regard another term χ_c, which acts as a damping envelope, in the aperture plane[91,101]

$$\chi_c(\vec{q}) = -\pi^2\Delta^2|\vec{q}|^4 \approx -\pi^2 C_c^2 \left(\frac{\Delta V}{\lambda V_0}\right)^2 |\vec{q}|^4, \tag{5.47}$$

where $C_c = 1.4\,\mathrm{mm}$ is the chromatic aberration constant as specified by the FEI company for Tecnai series TEMs and Δ is a parameter regarding fluctuations — or spread — of the acceleration voltage and magnetic lens currents[91]. For the sake of simplicity we neglected the influence of lens current fluctuations. $\Delta V = 3\,\mathrm{eV}$ is the energy spread[c] and V_0 is the primary energy.

The expressions χ_s and χ_c due to the aberrations are regarded in the aperture plane wave function ψ_{ap} in Eq. 5.22 such that the wave function in the sample plane reads

$$\begin{aligned}
\psi_{sp}(\vec{x}) =& \mathcal{F}\left(A(\vec{q})e^{i\left(-\varphi_{U,2}(\vec{q})+\chi_s(\vec{q}\,')\right)+\chi_c(\vec{q}\,')}\right)\cdot e^{-2\pi i\tan(\beta_2)\vec{k_2}\cdot\vec{x}} \\
&+ \mathcal{F}\left(A(\vec{q})e^{i\left(-\varphi_{U,1}(\vec{q}\,'')+\chi_s(\vec{q}\,'''))\right)+\chi_c(\vec{q}\,''')}\right)\cdot e^{-2\pi i\tan(\beta_1)\vec{k_1}\cdot\vec{x}} && (5.48)\\
\vec{q}\,' =& \left(\tan(\beta_2)|\vec{k}_2|,\, k_{2,\theta}\right) && (5.49)\\
\vec{q}\,'' =& \left(\tan(\beta_1)|\vec{k}_1| + \gamma(U),\, k_{1,\theta}\right) && (5.50)\\
\vec{q}\,''' =& \left(\tan(\beta_1)|\vec{k}_1|,\, k_{1,\theta}\right), && (5.51)
\end{aligned}$$

where $\varphi_{U,i}$ are the phase shifts caused by the ring electrodes (see Eq. 5.38 and 5.28), χ_i are the additional terms due to the lens aberrations. As these aberrations are radial symmetric with respect to the optical axis we have to regard them in the Fourier transform with linear translations. Thus three linear translations $\vec{q}\,', \vec{q}\,''$ and $\vec{q}\,'''$ are required. $\vec{q}\,'$ describes the coordinate system with origin on the optical axis with respect to the coordinate system in which the aperture center is the origin. $\vec{q}\,''$ (identical to the coordinate $q\,'$ used in Eq. 5.35) represents the coordinate system for the phase shift in the inactive phase plate, which we have assumed to be radial symmetric relative to a point beyond the center of the adjacent aperture hole. $\vec{q}\,'''$ serves the same purpose as $\vec{q}\,'$, but for the other aperture.

The Fourier transforms in Eq. 5.48 are calculated for each point in the $y \geq 0$ half plane. To speed up the process *Pyro*[102] — a Python module for the distribution of Python objects over a network — has been used. Due to the symmetry with respect to the $y = 0$ axis all values in the $y > 0$ half plane are flipped down to the $y < 0$ half plane in order to obtain a full 2D image. Afterwards the shift terms due to the aperture displacements are calculated in 2D and multiplied onto the results of the Fourier transforms.

As a first step in the treatment of aberrations we compare in Fig. 5.12 the superposition of the two incident waves for an aberration-free (**red** curve) and aberration-afflicted (**green** curve) lens in absence of phase shift $\varphi_{U,i}$. The aberrations cause a redistribution of intensity from the central maximum to the entire sample plane. The phase difference shows only negligible effects in the area of interest. The attentive reader might notice again peaks at $x \approx \pm 1\,\mathrm{nm}$ in

[c] Proportional to measured width of zero loss peak in energy loss spectra.

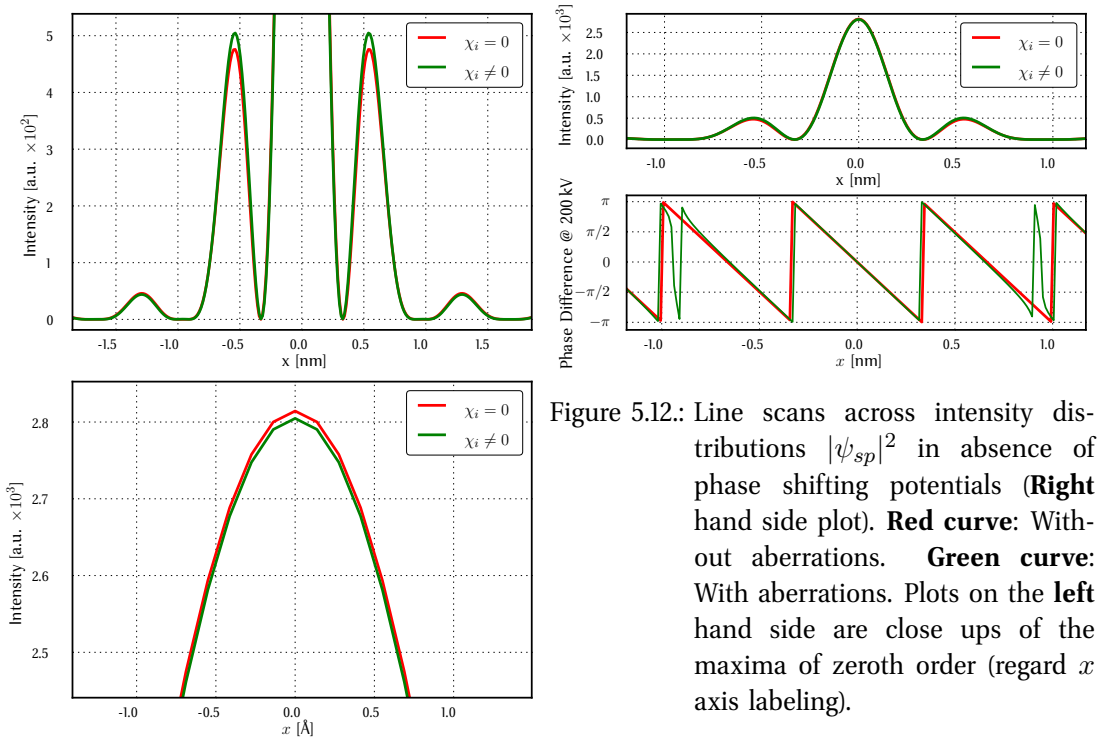

Figure 5.12.: Line scans across intensity distributions $|\psi_{sp}|^2$ in absence of phase shifting potentials (**Right** hand side plot). **Red curve**: Without aberrations. **Green curve**: With aberrations. Plots on the **left** hand side are close ups of the maxima of zeroth order (regard x axis labeling).

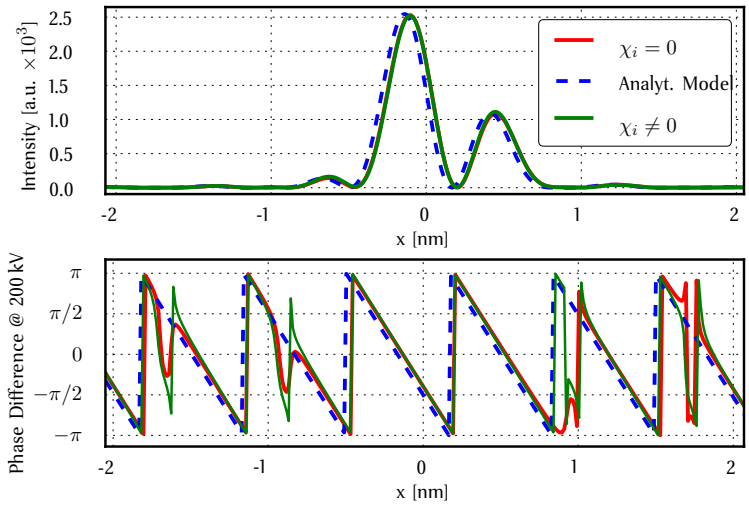

Figure 5.13.: Line scans across the intensity distribution $|\psi_{sp}|^2$ for the three investigated scenarios: analytical (**blue dashed** curve), numerical ($U = 0.15\,\mathrm{V}$) without aberrations (**green continuous** curve) and numerical with aberrations (**red continuous** curve)).

the phase difference plot (compare Fig. 5.10). As all phase shifting terms φ_i have been set to zero these peaks are caused by the treated aberrations χ_c and χ_s.

After investigation of the effects of aberrations on the setup in absence of phase shifting potentials $\varphi_{U,i}$ we will regard those in Fig. 5.13. The dashed blue line shows the intensity distribution and phase difference for a phase shift of $\pi/2$ (see Sec. 5.2.1) according to the constant model (see Sec. 5.2.1). The red curve reproduces the results of Sec. 5.2.2.1. The green curve results upon regard of aberrations and non-constant phase shift $\varphi_{U,i}$. As one can see the intensity distribution shows an negligible intensity redistributing effect as in Fig. 5.12; the peaks in the phase difference become stronger, but due to the lack of intensity in these regions these are negligible as well.

In Sec. 5.2.2.1 the switching of the sign of the applied potential had no noticeable effect except for the mirroring at the $x = 0$ axis (see Fig. 5.11). In presence of aberrations the negative potential can partially counteract the blurring effects of the aberrations as shown in Fig. 5.15; less intensity is distributed to regions of zeros of the Bessel function.

So far we have seen that the analytical model is a decent description of the cross over in the region $|x| < 1\,\mathrm{nm}$ for small phase shifting potentials, if the intensity shift is neglected. Aberrations show little influence on the intensity and phase difference in the region of interest and can be handled — in theory — rather well by application of a negative potential.

The calculations consistently suggest a full width at half maximum (FWHM) of the envelope Airy disk of approximately 1 nm independent of potential and aberrations. As the calculations in this section assumed an incident plane wave in the aperture plane one would expect to find larger FWHMs in experiments as the incident wave in reality is given by a spherical wave originating from a point-like source and propagating through the gun lens and C1 lens. Thus for a true realistic scenario one would have to regard the approximation error — deviation of the plane wave from the actual spherical one — in the aperture plane.

Furthermore the model for the phase shift $\varphi_{U,i}$ (see Sec. 4.3.3) has not produced quantitative reliable numbers, which might as well have a disadvantageous effect on experimental spot diameters.

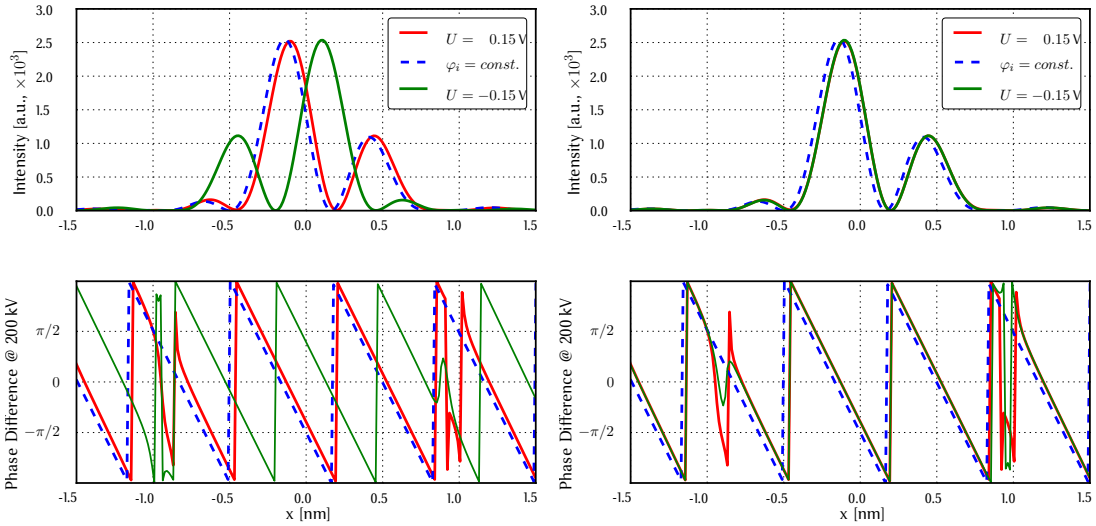

(a) Non-flipped (b) Flipped

Figure 5.14.: Line scans across the intensity distribution along the $y = 0$ axis. The line scans compare the analytical model (**dashed blue** curve) with the aberration afflicted model. In the latter positive (**red** curve) and negative (**green** curve) potentials are regarded.

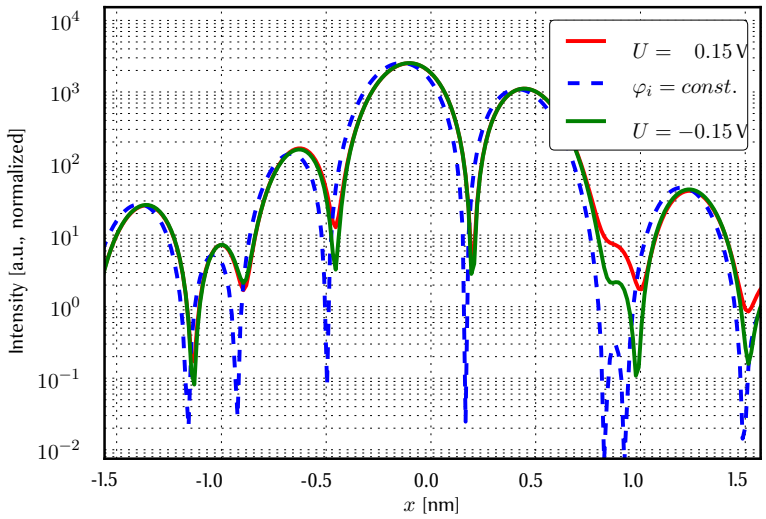

Figure 5.15.: Close up of intensity distribution from Fig. 5.14b on a logarithmic scale. The intensity blurring due to aberrations is partially counteracted by the negative potential applied to the ring electrode.

5.3. Electron Penetration Depth

Monte Carlo methods (or Monte Carlo experiments) are a broad class of computational algorithms that rely on random sampling to obtain numerical results. They are often used in physical and mathematical problems and are most suited to be applied when it is impossible to obtain a closed-form expression or infeasible to apply a deterministic algorithm. Monte Carlo methods are mainly used in three distinct problems: optimization, numerical integration and generation of samples from a probability distribution[103].

In Chap. 7 we will report experimental problems that we suspect to originate from charging effects that are caused by primary electrons creating electron-hole pairs or getting trapped inside the twin aperture (compare Sec. 6.2 for twin aperture design). Therefore we use electron trajectories calculated with the CASINO[104] software to estimate a minimum metal top layer thickness in order to prevent electrons from penetrating underlying insulating layers and thus electrostatic charging.

The used program *CASINO* ("monte CArlo SImulation of electroN trajectory in sOlids")[104–107] is a complex single scattering Monte Carlo simulation of electron trajectories in solids specially designed for low beam interaction in a bulk and thin foil samples. It can be used to generate many of the signals (X-rays and back scattered electrons) recordable in a scanning electron microscope (SEM)[108].

The main part of the CASINO program is the simulation of a complete electron trajectory through a solid. CASINO assumes an incident Gaussian-shaped electron beam, where the parameters[d] can be freely chosen. The program determines a mean distance between scattering events — elastic and inelastic ones — and assumes a continuous energy loss function. The trajectory — or the series of scattering events — is calculated until the electron energy falls below a limit value or the electron escapes the solid through one of its surfaces[104]. These calculations regard predetermined scattering cross-sections[104,106,109,110] for the chosen solid material. The interested reader can find a detailed description of the program and algorithms in Refs. [104–107]. For further evaluation these trajectories can be exported to ASCII files.

In order to determine a suitable metal layer thickness we have extracted the maximum depth of each calculated trajectory and plotted a histogram thereof (see Fig. 5.16). The histogram is normalized according to

$$\sum_i h(x_i) \cdot b = 1, \tag{5.52}$$

where b is the width of the bars of the histogram and $h(x_i)$ is the value of the bar with index i. For the calculation of trajectories a sample thickness of 25 µm was assumed. In case any electrons had passed through the layer, these electrons would have been regarded with a maximum penetration depth equal to the layer thickness as pointed out previously (see also Fig. 5.16a).

The histogram's data can be used to determine an approximation of the penetration depth probability. The histogram describes the distribution of maximum penetration depths achieved

[d] Diameter, angle of incidence, ...

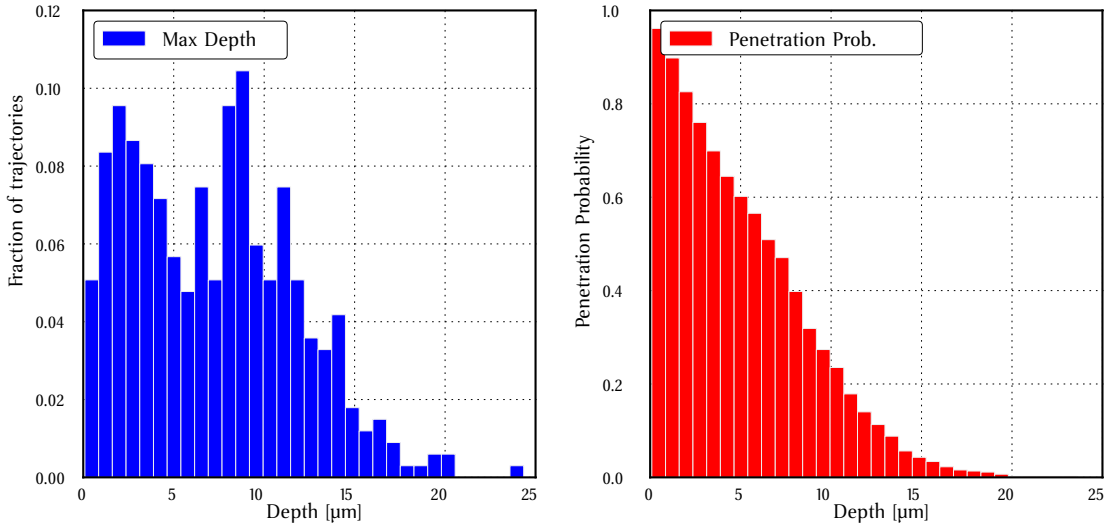

(a) Histogram of maximal penetration depth. (b) Penetration probability.

Figure 5.16.: Evaluation of 440 electron trajectories calculated with CASINO software for a platinum substrate and an acceleration voltage of 200 kV. (a) Histogram of maximal penetration depths of the trajectories. (b) Penetration probability derived by integration over the histogram data along the penetration depth.

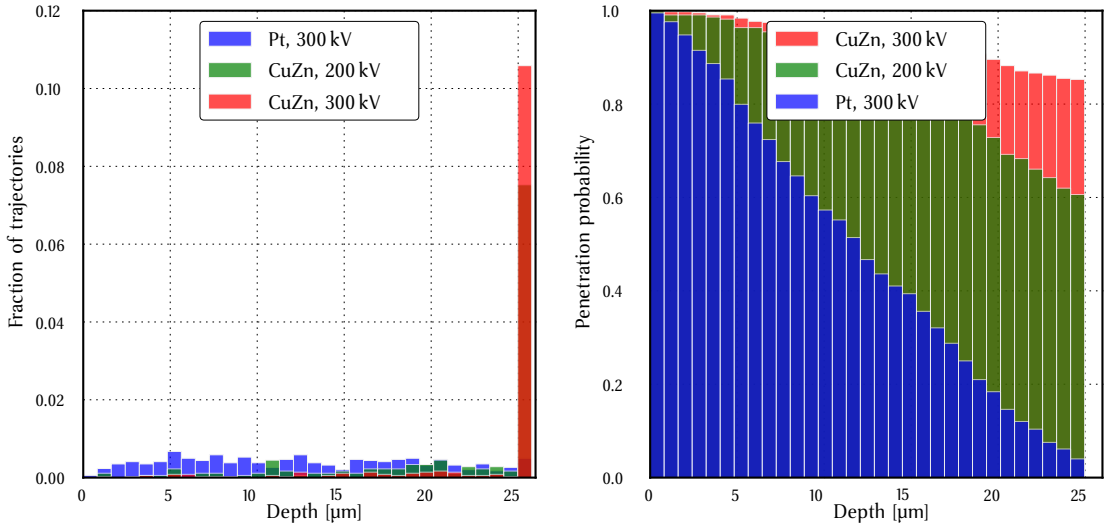

(a) Histogram of maximal penetration depth. (b) Penetration probability.

Figure 5.17.: Evaluation of electron trajectories calculated with CASINO software for a platinum and brass substrate at an acceleration voltage of 300 kV; for the latter material evaluation is included for 200 keV electrons. (a) Histogram of maximal penetration depths of the trajectories. The last bar behind 25 µm takes into account any transmitted electrons. (b) Penetration probability derived by integration over the histogram data along the penetration depth.

by single electrons. For an approximation one simply has to perform a dicretized integral over the histogram data $h(x)$ in order to obtain a penetration probability

$$P(x) \approx 1 - \int_0^x h(x')\, dx' \approx 1 - \sum_{i, x_i' < x} h(x_i') \cdot b, \tag{5.53}$$

where $P(x)$ is the penetration probability, b is the width of bars in the histogram and i is the index of each bar. Fig. 5.16a shows the maximum depth histograms and Fig. 5.16b the penetration probabilities determined in the way as described above.

The penetration probability approximately follows an exponentially decreasing function. Even with a small number of 440 simulated trajectories we get a sufficient description of the penetration probability. Thus we conclude that a platinum top layer with a thickness larger than 25 µm should be sufficient to prevent 200 keV primary electrons from penetrating underlying insulating layers. The value of 25 µm has been chosen close to the deepest simulated trajectories, as the thickness of a Pt foil can significantly increase the time required during the fabrication process (see Sec. 6.2.2 and *Step 8* in Fig. 6.8).

Fig. 5.17 shows histograms and penetrations probabilities for different materials and acceleration voltages. As expected a 25 µm thick layer of platinum is not sufficient for 300 keV electrons as shown in Fig. 5.16a; a transmission rate of approximately 0.08 is observed. Analogously lighter materials with a thickness of 25 µm are even unsuitable for 200 kV acceleration voltage, e.g. brass (CuZn) has transmission rates of $\gtrsim 0.6$ for 200 kV acceleration voltage and $\gtrsim 0.85$ for 300 kV acceleration voltage.

5.4. Dynamical Diffraction Simulations

The focus of this thesis is on the wave optics of the twin aperture. Nevertheless a theoretical prediction of the EMCD signal expected in a real space map[3,38,40,41] for the twin aperture method would be interesting. Jan Rusz has previously written a simulation[38] to calculate the diffraction patterns of a hcp-Co crystal oriented in $[0001]$ zone axis direction and the dichroic signal in the diffraction plane for incident extended plane waves.

He adapted his code to regard two incident waves in order to allow a comparison between the two methods. For the sake of simplicity he assumed extended plane waves in the latter case instead of converging ones[7] and constant phase shifts as in Sec. 5.2.1.

As we have seen in Sec. 5.2 the constant phase shift model is a decent description. Using this model and the Fresnel propagator (see Eq. 5.1) one can determine the wave function in arbitrary planes above and below the sample plane (see Fig. 5.18) in absence of a sample. For the sake of simplicity we have chosen $z = 0$ in the sample plane[e] and$\varphi_i = 0$ in Fig. 5.18. The plot in the center of Fig. 5.18 is the phase front of the superpositioned wave.

As we have considered incident converging beams forming a cross-over in the sample plane these beams have to be diverging after the sample plane. Thus close to the cross-over plane ($\equiv$ sample plane) the incident waves can be approximated coarsely as spatially confined plane waves. As the phase front in Fig. 5.18 shows such an approximation would be reasonable

[e] For the sake of simplicity the sample plane contains no sample.

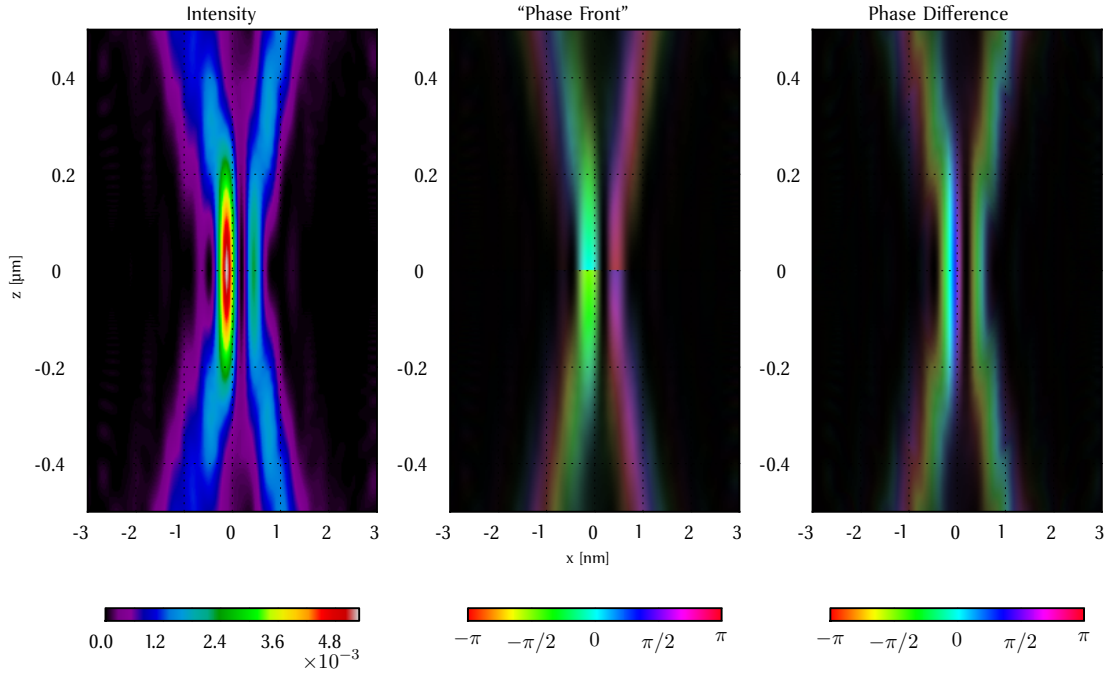

Figure 5.18.: Intensity distribution, phase front and phase difference in planes above and below of the sample plane ($z = 0$). Starting from Eq. 5.18 for the $z = 0$ plane with $\varphi_i = 0$ the wave function is propagated (see Eq. 5.1) to other planes. **Left**: Intensity distribution. **Center**: The phase front is the azimuthal component of the polar representation of the complex valued wave function. **Right**: Phase difference. Phase front and difference have been overlaid with a semi-transparent black layer, whereby the transparency is scaling with the intensity. For a z-range of approximately 100 nm the propagated wave can be approximated well by a plane wave.

for a range of approximately $z = \pm 50\,\mathrm{nm}$ — depending on the required accuracy of the approximation.

The following calculations in this section utilize a coarse approximation for the sake of simplicity — two incident spatially extended plane waves on a Co sample — as adaptations to Jan Rusz's code are not finished, yet. Jan Rusz is still working on adaptions for spherical waves. Preliminary results look very promising. Thus in this strongly simplified setup the incident wave function assumed by Jan Rusz is given by

$$|\psi_{in}\rangle = a_1|\mathbf{k}_1\rangle + a_2|\mathbf{k}_2\rangle \tag{5.54}$$

where $\mathbf{k}_{1,2}$ are the wave-vectors of the two extended plane wave components of the incoming beams and $a_{1,2}$ are their complex weight factors. For the idealized twin aperture experiment we assume $a_1 = 1$ and $a_2 = i$ in equivalence to $\varphi_1 = 0$ and $\varphi_2 = \pi/2$. The outgoing electron wave depends on the detector orientation and will be described by the wave vector $\mathbf{k}_f$.

If we denote the initial state of the electron subsystem of the specimen $|I\rangle$ and the final

excited state $|F\rangle$, the double differential scattering cross-section in such a setup follows the interferometric setup[35]

$$\frac{\partial^2\sigma}{\partial\Omega\partial E} \propto \left|\langle\psi_{\text{out}}| \otimes \langle F|\hat{V}|I\rangle \otimes |\psi_{\text{in}}\rangle\right|^2 \delta(E_I - E_F + E) \tag{5.55}$$

$$\propto \Bigg\{ \underbrace{|a_1|^2 \left|\langle k_f, F|\hat{V}|k_1, I\rangle\right|^2}_{\text{“reference beam”}} + \underbrace{|a_2|^2 \left|\langle k_f, F|\hat{V}|k_2, I\rangle\right|^2}_{\text{“shifted beam”}} + \underbrace{2\text{Re}\left[a_1^* a_2 \langle k_1, I|\hat{V}|k_f, F\rangle \cdot \langle k_f, F|\hat{V}|k_2, I\rangle\right]}_{\text{“interference term”}} \Bigg\} \delta(E_I - E_F + E) \tag{5.56}$$

where $\hat{V}$ is the interaction potential between the sample and probe electrons. Equation 5.55 gives rise to three terms describing inelastic scattering processes for each incident beam and an interference term (see Eq. 5.56). The first two terms are labeled as *reference beam* and *shifted beam* in Eq. 5.56. Occasionally we will refer to these terms as *direct terms* as well. These *direct terms* are of the same form as encountered in the treatment of the intrinsic method. Therefore these terms are computed by the non-modified code, which is discussed in Ref. [12]. Due to the shape of the incident wave function (see Eq. 5.54) the absolute value in Eq. 5.55 yields a third term, to which we will refer to as *interference term*. The mathematical treatment of this new term is described in Ref. [7].

Summarized, a modified version of the DYNDIF code[12], including the recently developed MATS algorithm[26], has been implemented for evaluation of such *interference terms*. Thus in principle evaluation of double differential scattering cross sections for a coherent illumination of the sample with an arbitrary number of coherent plane-wave components becomes possible. Such calculation would consist of separate evaluations of all single plane-wave contributions with the original code and all mixed terms with the modified version, taking care about relative shifts of the individual intensity contributions to the diffraction pattern[7].

By means of the mentioned methodology Jan Rusz calculated the individual contributions to the diffraction pattern for the L_3 edge of the hcp cobalt crystal illuminated by two coherent plane waves, both slightly tilted from the (0001) zone-axis orientation. The tilt is defined in terms of reciprocal lattice vectors $\mathbf{G} = (10\bar{1}0)$ as $lcc = \pm 0.3\mathbf{G}$, where lcc stands for Laue circle center. In this context the lcc simply defines the incidence angle, where lcc is the inplane component of the wave vector of an incident wave in reciprocal coordinates. In consistency with previous sections an acceleration voltage of 200 kV was chosen.

In the following figures the Thales circle is highlighted by a dashed blue circle in each diffraction pattern.

Fig. 5.19a shows the calculated diffraction pattern for $lcc = 0.3\mathbf{G}$ only. The first column shows the nonmagnetic component of the signal per hole in the $3d$-shell. Due to the nature of these calculations[17,37,111] the nonmagnetic signal is proportional to the number of holes in the $3d$-shell. For normalization purposed the number of holes was chosen to be one[17], resulting

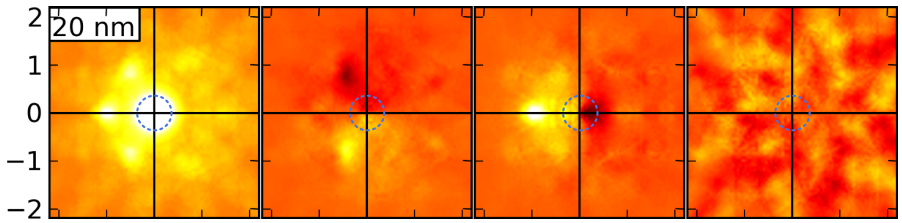

(a) Main components of the intensity in the diffraction pattern of hcp-Co with 200 keV and incoming beam direction tilted by $0.3\,\mathbf{G}$ from $[0001]$ zone axis, where $\mathbf{G} = (10\bar{1}0)$. These maps correspond to the non-interference/coherence term in Eq. 5.55. **First column** is the non-magnetic intensity per hole in the $3d$ shell (color range corresponds to ± 0.15) and **columns 2–4** represent the magnetic signal per $1\,\mu_B$ of spin magnetization in x, y and z direction (color range ± 0.005), respectively.

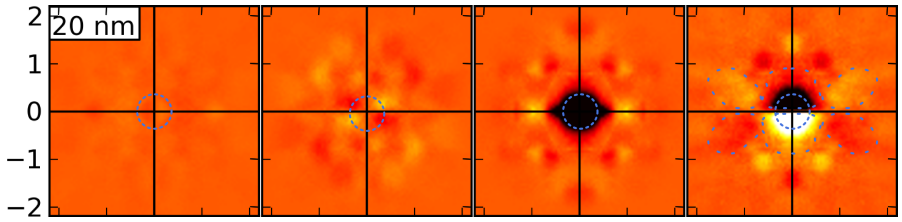

(b) Main components of the intensity in the diffraction pattern due to the coherence term. These maps correspond to the interference term in Eq. 5.55. See Fig. 5.19a for column description. Color scale was kept the same as in Fig. 5.19a to demonstrate the enhancement of EMCD signal. In **column 4** additionally the areas of positive and negative signal are outlined with blue dotted lines.

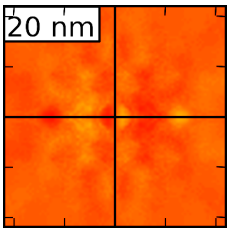

(c) First column of Fig. 5.19b at increased image contrast to illustrate left-right asymmetry.

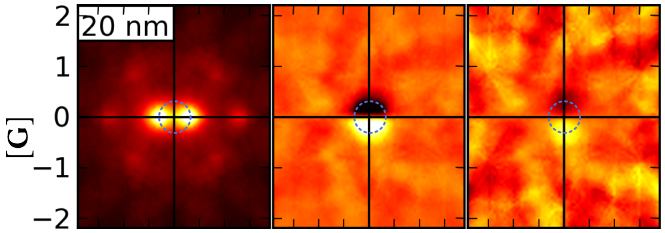

(d) Diffraction pattern (**left** column), absolute (**middle** column) and relative (**right** column) dichroic signal for a 20 nm thick hcp-Co sample oriented in $[0001]$ zone axis and acceleration voltage 200 keV. The color ranges are $[0,\ 2.0]$, $[-0.035,\ 0.035]$ and $[-0.07,\ 0.07]$ for the three columns, respectively.

Figure 5.19.: Simulation of intensity distribution in the diffraction pattern for a 20 nm thick cobalt sample and 200 keV electrons. Note the different ranges associated with the color bar. By means of a **dotted blue** circle the Thales circle is indicated. The range of axes for all plots in this figure are $q_x \in [-1.9\,\mathbf{G},\ 1.9\,\mathbf{G}]$ and $q_y \in [-2.2\,\mathbf{G},\ 2.2\,\mathbf{G}]$, where $\mathbf{G} = (10\bar{1}0)$. Courtesy of Jan Rusz. For maps for different sample thicknesses see Ref. [7] or Appendix A.5.

in a signal per hole. It is the major contribution to the diffraction pattern giving it the overall shape consisting of several broadened Bragg spots. The columns 2, 3 and 4 show the magnetic signal[f] per magnetic moment μ_B along the x, y and z directions, respectively.

Initially the EMCD effect was thought of to work only for magnetizations along the z direction, but Klaus Leifer et. al. proposed that a dichroic signal would also be measurable for inplane (x, y) magnetizations[112]. Even if the signal per magnetic moment is stronger for inplane magnetizations, most magnetic moments are aligned along the magnetic field of the objective lens of the microscope, which is parallel to the z direction.

Maps for the $lcc = -0.3\mathbf{G}$ can be obtained from Fig. 5.19a by exploiting the symmetry properties of the experimental geometry.

Fig. 5.19b shows the *interference term*. The non-magnetic signal (1st column) is very small compared to similar contributions from direct terms (*reference beam* and *shifted beam*; compare 1st column in Fig. 5.19a); its peak values are about 6–7 times smaller[7] than contributions from a single direct term. This signal shows an asymmetry between the left and right half plane, which depends on the relative phase difference between the two incoming plane waves. Fig. 5.19c shows the 1st column of Fig. 5.19b at increased image contrast. As one can see the non-magnetic signal is axially symmetric; the left and right half plane show similar features, but with different sign. We have encountered a similar effect on the focused electron probe in the sample plane in Sec. 5.2, where the intensity within the Airy disk is modulated and redistributed by a fringe pattern due to the phase difference.

The most important result of these simulations can be seen in the maps of the magnetic signal (columns 2–4 in Fig. 5.19b). The magnetic signal is substantially stronger in the *interference term* compared to the direct term (compare Fig. 5.19a); the peak magnetic signal is about 5–10 times stronger[7].

For the magnetization along the z-direction (Fig. 5.19b, 4th column) we observe an area of positive and negative signal approximately at the Thales circle (dashed blue circle) positions around each strongly excited Bragg spot; these areas are indicated by blue dotted polygons.

Magnetization along the x direction (Fig. 5.19b, 2nd column) does not lead to a strong intensity contribution in the diffraction pattern, even if it is of comparable magnitude to the intrinsic EMCD (Fig. 5.19a). On the other hand the signal that would originate from magnetization along y direction (Fig. 5.19b, 3rd column) is rather strong and predominantly of negative sign. Changing the sign of the phase shift a_2 of the two incoming plane waves we would observe a positive contribution instead. This signal can be attributed mainly to inelastic scattering causing nonzero z components of the momentum transfer vectors[7].

Fig. 5.19d shows the combined nonmagnetic signal and maps of the absolute and relative magnetic signals, which is the fraction of absolute magnetic and nonmagnetic signal. These maps show a left-right asymmetry in the nonmagnetic signal due to the contribution from the interference term — as mentioned previously. Strong dynamical diffraction effects cause variations in the spot intensities and the signal in between them. Figs. A.11 and A.11c show maps of the (non-)magnetic signal for different thicknesses in the range 5–30 nm. The total absolute magnetic signal (middle column) shows a considerable dependence on the sample thickness as known from the intrinsic method, were this dependence is due to dynamic diffraction effects.

[f] Normalization derived due to similar reasons as for nonmagnetic signal.

The signal originates in the interference of the two phase shifted beams. Generally, its intensity scales with the intensity of the spots of the two transmitted beams. This dependence of the magnetic signal is referred to as *Pendellösung* oscillations[8,12,31].

While the absolute signal — magnetic and nonmagnetic contributions — shows a strong dependence on sample thickness due to dynamical diffraction, which is the main goal of the new proposed setup to overcome, Jan Rusz's calculations show that the relative magnetic signal (right column in Figs. 5.19d and A.11c) — magnetic signal divided by absolute signal — is significantly less dependent on the sample thickness[7].

Having this theoretical prediction, which is based on extended plane waves and a constant phase shift, one might be slightly optimistic whether the measurement of a dichroic signal using this setup will be successful in the future. In Chap. 7 we will point out some remaining issues with the constructed twin apertures, which prevented the attempt of measuring an EMCD signal so far.

5.5. Summary

In this chapter three different kinds of electron optical calculations have been performed.

The first subject of investigation was the probe formation due to a twin aperture in Sec. 5.2. The attempt of focusing a single spot in the sample plane — i.e. the condenser system is tuned such that the sample plane coincides with the BFP of the condenser system — one obtains a superposition of two focused spots due to the two aperture holes. In the formation of this superposition we have investigated the influence of different phase shifting potentials. As we have shown the rather coarse approximation of constant phase shifts allows a sufficient description of the resulting electron wave in the sample plane within certain limitations. Hyperbolic dependencies of the phase shift basically result in a small shift of the intensity distribution with some minor effects on the phase front at large distances from the optical axis. Phase terms due to aberrations cause some minor differences in the intensity distribution, which can be reduced by choosing the sign of the applied potential such that the phase term due to the potential has a different sign than the phase term due to the aberrations.

Using Monte Carlo simulations of electron trajectories we have determined a thickness for the top metal layer of the twin aperture which should ensure that no primary beam electrons can penetrate underlying layers of the twin aperture as such penetrating electrons could cause electrostatic charging and lead to aberration effects.

Jan Rusz performed numerical calculations of the diffraction pattern and expected dichroic signal for a twin aperture setup using the approximation of incident plane waves instead of converging ones. His calculations show a stronger signal, but which is still modulated by dynamical diffraction effects.

6. Experimental setup

In this chapter we will give a detailed description of the laboratory setups and modifications to the setup as far as needed for this work.

6.1. Microscope & Equipment

6.1.1. Microscope

Electron microscopes[113–115] have been and still are very useful tools in science. The working principles of these machines in all their operational variations (TEM, SEM, STEM) are subject of a series of textbooks — e.g. Refs. [42, 55, 91, 116]. Therefore the description of the principal electron microscopes will be omitted at this point. The interested reader is referred to the previously cited text books. Instead we want to take a closer look at the used microscope.

For the course of this work a *FEI Tecnai F30 ST* with a field emission gun[119] (FEG) has been used. The condenser system comprises three lenses (C1, C2 and mini condenser (MC)). Two of them (C1 and C2) receive an aperture holder for defining the beam shape (see Fig. 6.1). The twin aperture introduced in Sec. 2.2.3 is installed as a C2 aperture.

As pointed out in Sec. 2.2.3 the goal is to prepare a focused beam in the specimen plane. The MC lens is under automatic control of the microscope software, which sets the MC excitation to a static value depending on the mode of operation and magnification. The C1 lens is only excitable in eleven discrete levels, which are commonly referred to as *spot sizes* as the C1 lens illuminates the C2 aperture and thus has considerable influence on the beam coherence (in TEM mode) and the smallest achievable cross over (in STEM mode). Thus the operator only can control smoothly the C2 lens which is commonly referred to as *Intensity* as the C2 lens alters the current density in the sample plane.

6.1.2. Energy Filter

Electron energy loss spectroscopy (EELS) is almost as old as electron microscopy itself. Since the first measurements[120–122] in the 1930s and 40s spectrometer technology has been under constant development. Latest devices (e.g. Gatan GIF[a] Quantum[123]) allow acquisition of up to 1000 spectra per second and simultaneous acquisition of two different energy ranges.

In Sec. 2.2 we have already stated the necessity of an electron energy filter for EMCD measurements. The microscope used for the experiments in Chap. 7 is equipped with a post-column *Gatan GIF Tridiem*. Fig. 6.2 shows a schematic drawing of the setup. The electron beam enters the spectrometer through an aperture. By means of a magnetic prism the electrons are forced onto a circular path, where the radius of this circle is depending on the strength of the field

[a] Gatan Image Filter.

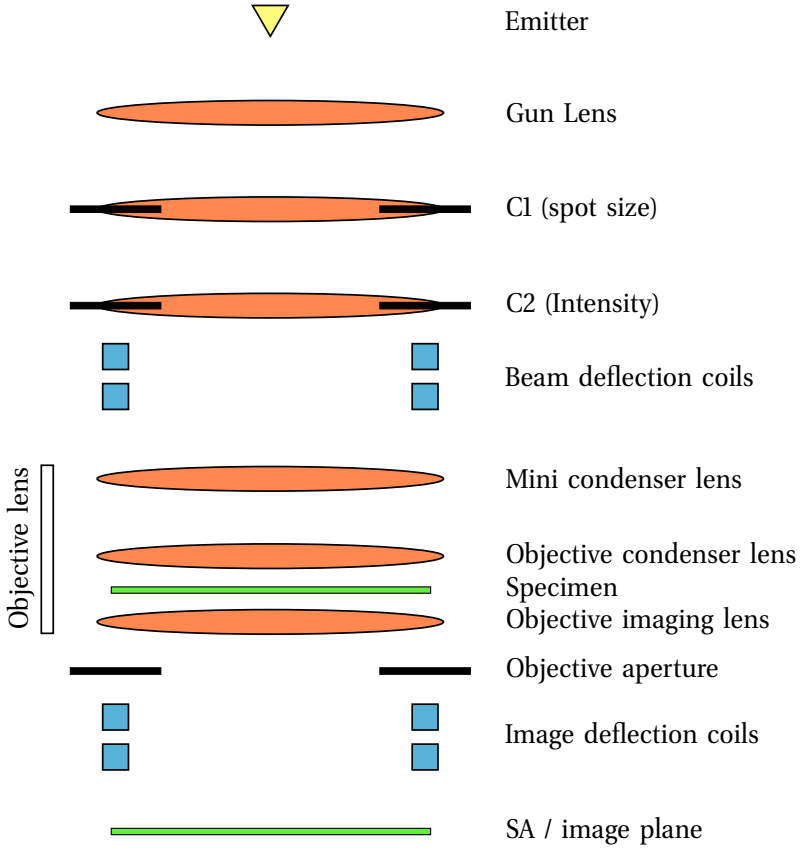

Figure 6.1.: Schematic arrangement of optical elements in a Tecnai F30 according to manufacturer's manuals[117,118]. The MC and objective lenses are contained in a single assembly group indicated by the bracket on the left in the figure. In the SA plane the first magnified image is visible and further magnified using the projector system. The projector and stigmator systems have been omitted in this figure. As the path of rays depends on the different operations modes of the (S)TEM the path of rays has been omitted, too.

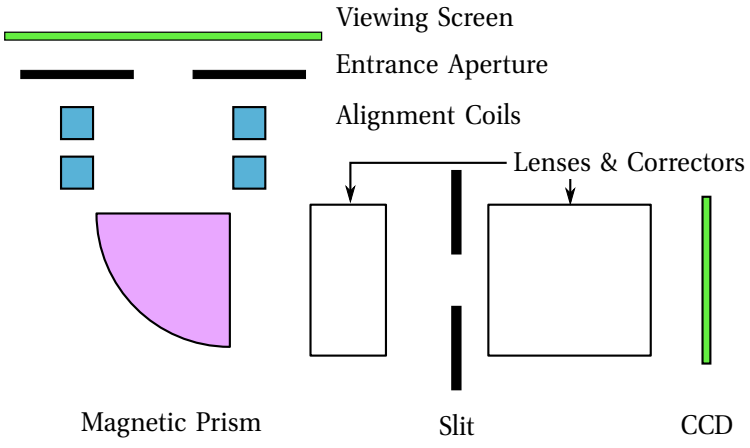

Figure 6.2.: Schematic arrangement of energy filter *GIF Tridiem*.

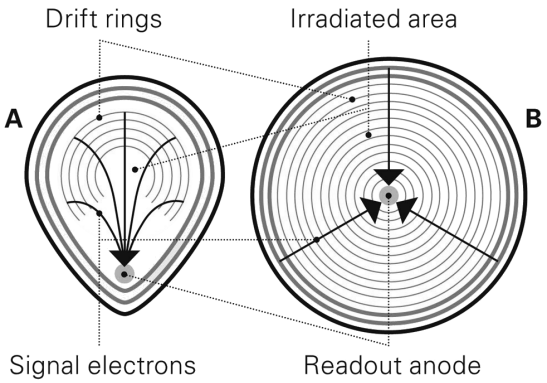

Figure 6.3.: Schematic of the droplet shaped (A) and round (B) SDDs used by Bruker. Arrows indicate the drift path of the excited electrons towards the readout anode. Image taken from Ref. [126].

and the velocity of the electrons. Thus at the exit face of the prism one already gets a spectral distribution. Depending on the desired operation mode the lenses and correctors (sextu- and quadrupoles) project the image of the spectrum (spectroscopy) onto the CCD camera. Alternatively the actual TEM image can be reassembled by the second lens assembly allowing to insert a slit into the spectrum. Thus an energy filtered TEM image (EFTEM), where only electrons that have suffered a certain energy loss contribute to the image, is projected onto the camera.

6.1.3. Energy-dispersive X-ray Spectroscope

Energy-dispersive X-ray spectroscopy (EDX) is an analytical technique used for the elemental analysis or chemical characterization of a sample. It relies on the fundamental principle that each element has a unique atomic structure allowing only a unique set of lines in an X-ray spectrum[124,125]. The emission of characteristic X-rays from a specimen is stimulated by high-energy electrons. Initially the bound electrons in the sample are considered to be in no excited states. The incident beam may excite an electron in an inner shell, ejecting it from the shell while creating an electron hole. An electron from an outer, higher-energy shell then fills the hole while emitting a photon with an energy being equal to the energy difference of the two states[124].

The installed EDX system by Bruker uses a silicon drift detector (SDD), which is a type of energy dispersive solid state detector. It utilizes a special drift field structure to guide charges produced by absorbed X-rays to an extremely small readout anode. The structure is optimized for each type of SDD[126,127]. Bruker SDD detectors come in two different shapes: droplet and round (see Fig. 6.3).

The SDD is derived from the principle of side ward depletion[128] and has an additional electrical field parallel to the surface. The method of side ward depletion allows the full depletion of a thin large area semiconductor wafer, e.g. n^- Si, through large area p^+ junctions on each surface of the wafer and a small sized n^+ ohmic contact[128,129]. The ionizing X-rays generated on an investigated sample are absorbed in this depleted volume of the detector and

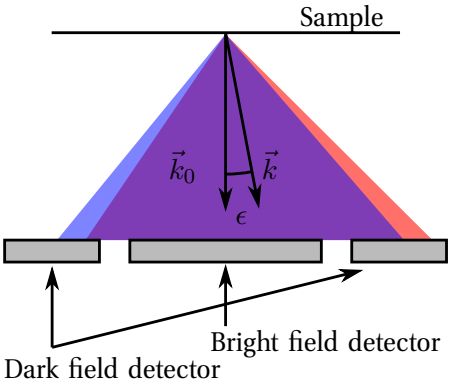

Figure 6.4.: Schematic cross section of STEM detectors to demonstrate working principle of DPC. In equilibrium the divergent electron beam propagates along $\vec{k}_0$ (blue beam) and illuminates the dark field detector segments (left/right) evenly. Electromagnetic forces tilt the propagation direction by an angle ϵ to $\vec{k}$. Thus the segments are no longer evenly illuminated and we measure a horizontal strength. In practice the same is done with the other pair of segments (out of plane, not shown).

the charges generated during this absorption process need to be transported to the n^+ contact; this is done by the additional in-plane electrical field[129,130].

In order to conduct energy dispersive measurements the *readout anode* (n^+ contact; see Fig. 6.3) is surrounded by a transistor structure, which creates a potential well.

6.1.4. DPC Detector

Differential Phase Contrast[131–133] (DPC) measurements in a TEM are in principle rather easy to perform as the setup for such measurements only requires a different STEM detector that allows the measurement of deflections of the electron probe caused by electric and magnetic fields[77–80,134]. Using the technique of Differential Phase Contrast (DPC) imaging and quantification of electric[79,134] and magnetic[77,78] fields down to the subatomic scale[80] become possible.

For this task the default annular dark field detector is replaced with an annular detector that is split into four independent segments[81,135]. Detailed description of the construction of the particular installed detector device can be found in Ref. [135].

Assuming that the beam hitting the detector has an equilibrium position (blue beam in Fig. 6.4), in which the four segments are exposed to an equal number of electrons, a deflection due to an electric or magnetic field will cause a difference in the electron count of adverse segments (red beam in Fig. 6.4). Thus by calculating the difference between the electron counts of adverse segments one gets a value describing the deflection along the axis defined by those two segments. Thus a DPC image describes the beam deflections in a coordinate system defined by the detector orientation. These deflections can be quantitatively related to magnetic[78,135] and electric[79] fields.

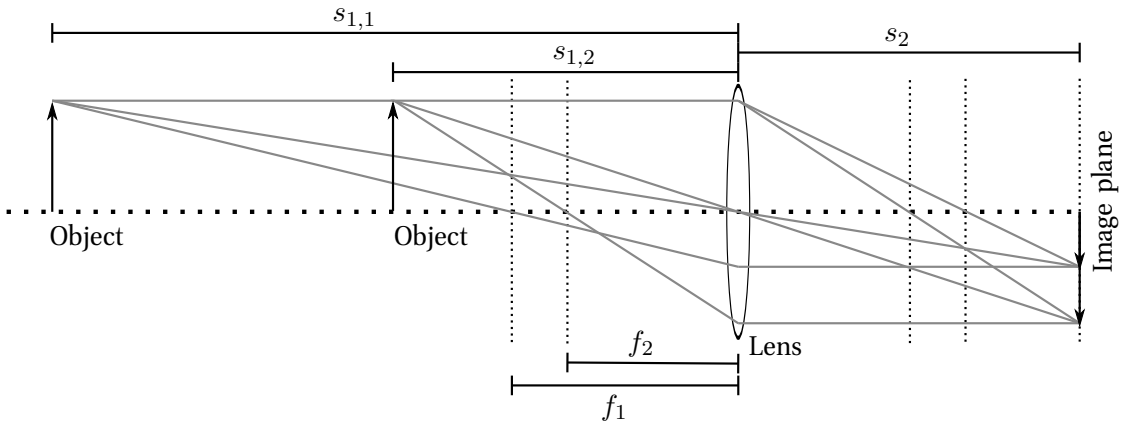

Figure 6.5.: Ray diagram for the imaging of an object point in front of a lens (system) by a distance $s_{1,i}$ for two different focal lengths f_i of the lens. The distance s_2 between lens and imaging plane is constant. By decreasing the focal length from f_1 to f_2 an object in a plane closer to the lens is sharply projected into the image plane.

6.1.5. Shadow Image

A prerequisite for the observation of a *shadow image* [b] or *Ronchigram*[118,136,137] is the operation of the imaging lens system of the microscope in *overfocus*[55,136]. In the imaging TEM mode an overfocus causes the imaging system to project an object plane — that is below the sample plane — to the image plane. Fig. 6.5 is illustrating the meaning of overfocus. The thin lens formula describes the relations between object distance, image distance and focal length

$$\frac{1}{f_i} = \frac{1}{s_2} + \frac{1}{s_{1,i}}, \tag{6.1}$$

where f_i is the tunable focal length of a (magnetic) lens, s_2 is the constant distance of the image plane to the lens plane and $s_{1,i}$ is the distance of the object plane to the lens plane (see Fig. 6.5).

Assuming a sample is at a distance $s_{1,1}$ from the lens the microscope operator obtains a sharp image of the sample in the image plane by adjusting the focal length of the lens to f_1 — the sample is *in-focus*. If the operator changes — e.g. reduces — the focal length the image becomes blurred because a change in focal length changes the object distance, if the image distance is kept constant. One speaks of *overfocus* when the distance of the plane, which is sharply projected to the viewing screen, to the lens plane is shorter than the distance $s_{1,i}$ of the object plane to the lens plane as the lens action is increased.

In a TEM no other objects are in the path of rays than the sample[c]. Thus when imaging a plane that does not coincide with the sample plane one is imaging a wave function that has propagated[91] a *defocus* distance — that is the change in object distance due to the change

[b] Also known as *blow-up image*.
[c] Except for apertures.

in focal length — from the sample plane to the current object plane. To this propagated (defocused) wave function or object we will refer as *shadow image*.

In overfocused imaging TEM mode one can create a focused spot in the specimen while an extended beam is visible in the image plane as the object plane is in the optical path of the electron behind the sample plane. The ray diagram in Fig. 6.6 shows a sample in overfocus between the condenser lens system and the object plane, which is projected to the viewing screen. The condenser system — in case of a standard condenser aperture — annularly illuminates the sample plane and projects a (magnified) image — the *shadow image* — of the sample section to the object plane. The shadow image in the object plane is shown at the right hand side of the object plane in Fig. 6.6 for the cases 'spot in sample plane' and 'spot in front of sample plane'. The shadow image is magnified by the projector system and shown for different condenser lens excitations in Fig. 6.7.

Commonly one has not a truly parallel beam hitting the sample, but a slightly divergent or convergent one. To view the Ronchigram, a special case shadow image, the condenser system is used to form a cross over of the beam in the sample plane. Let us start with a convergent beam with a cross over in front of the sample plane. The divergent illumination in the sample plane casts an enlarged shadow into the object plane, which is projected to the image plane. If the radius of the illuminated area in the sample plane is reduced, the cross over approaches the sample plane. Thus the cast shadow image shows a smaller area of the sample. During the transition of the cross over through the sample the radius of the illuminated area is changing faster than the convergence/divergence angle. Thus — as Fig. 6.6 illustrates — the magnification of the shadow image increases rapidly to a maximum and the Ronchigram is considered to be focused at the highest magnification in the shadow image.

The magnification of the shadow image is dominated by the defocus distance and the radius of the illuminated area. In an idealized, aberration-free microscope for the particular inclination of the rays for which the cross-over is in the sample plane ($\hat{=}$ convergence angle) the magnification becomes infinite so that a circle of infinite magnification appears on the screen (see also Fig. 6.7).

The previous consideration is describing an aberration-free lens. If applied to a lens having strong spherical aberration, the ray diagram in Fig. 6.6 also explains how a gradient of magnification is observable in the shadow image (see Ref. [136]). Beams traversing the lens plane at a point far away from the optical axis (abaxial) suffer a stronger deflection than rays passing through the lens plane close to the optical axis (adaxial). In case of strong aberrations the abaxial rays are even more deflected towards the optical axis such that abaxial rays form a cross-over in a plane in front of the plane containing the cross-over formed by adaxial rays. Thus abaxial rays project a larger specimen area with a lower magnification onto the screen. As one can see from the focal series in Fig. 6.7 the used Tecnai F30 has no strong aberrations such that the shadow image shows no noticeable gradient in magnification (compare Fig. 3 in Ref. [137]).

Thus the Ronchigram is commonly used to accurately focus the electron probe to the sample plane for STEM mode. In Sec. 7.4.1 we will use this technique to grow contaminations with a focused spot on a thin Si_3N_4 membrane.

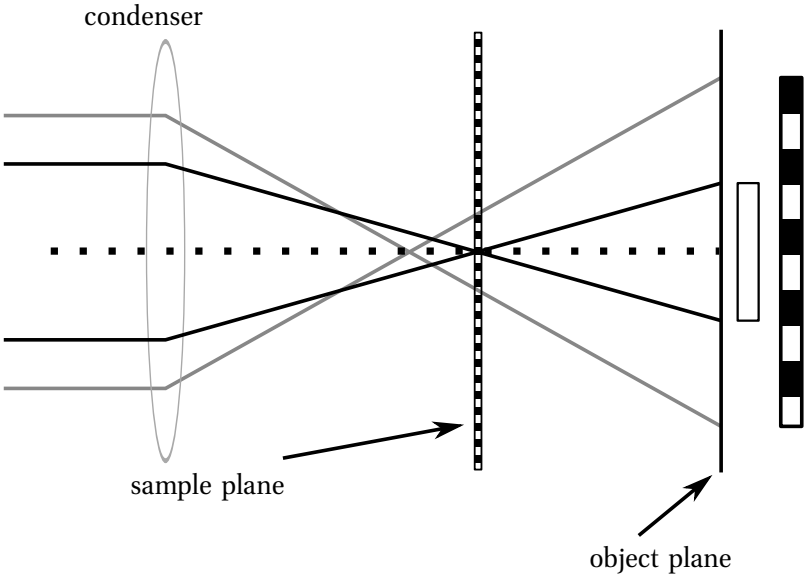

Figure 6.6.: Ray diagram of the formation of a shadow image with an “aberration-free” lens. Partial reconstruction of Fig. 5 from Ref. [136]. The sample is represented as a grating of black and white boxes. Depending on the cross over position the shadow image in the object plane shows different magnifications. Shadow images right of object plane indicator.

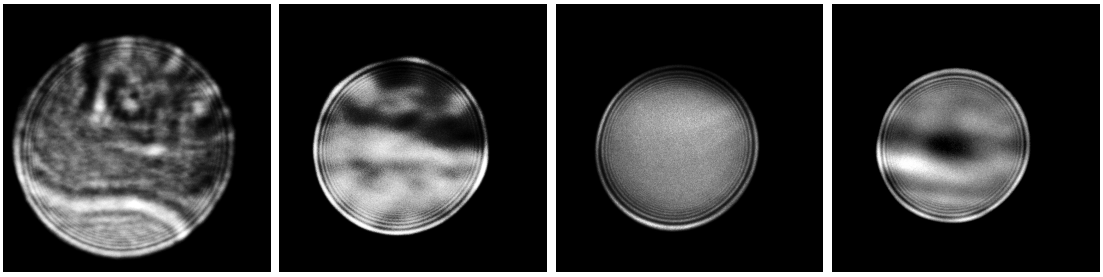

(a) $\Delta I = 47 \cdot 10^{-3}\%$ (b) $\Delta I = 17 \cdot 10^{-3}\%$ (c) Intensity: $I_0 = 52.346\%$ (d) $\Delta I = -8 \cdot 10^{-3}\%$

Figure 6.7.: TEM images of shadow images for different cross-over planes for a constant over-focus of the objective lens of 21.33 µm (compare Fig. 3 in Ref. [137]). Images show a flake of graphite. Scale bar has been omitted due to the effect shown in Fig. 6.6.

6.2. Manufacturing of Twin Aperture

The production process used in this work follows the idea of the process described in Ref. [58]. For convenience we start with a substrate and perform a series of electron beam lithographic (EBL), etching and evaporation processes. As the differences between those processes due to different substrates are marginal we will describe the process for commercial Si_3N_4 (or in short: SiN) membrane substrates in more detail in Sec. 6.2.1 and only point out those differences in Sec. 6.2.2.

In the following we will be referring to the incomplete twin aperture as sample occasionally.

6.2.1. Substrate: Commercial Si_3N_4 Membrane

The substrates used for this class of twin apertures are commercially available Si_3N_4 membranes. A 30 nm thick Si_3N_4 layer spans over the surface of a silicon wafer which has been etched from the back in a regular, rectangular pattern such that the membrane spans freely over gaps in the wafer. Each of these windows has a size of approximately $100 \times 100\,\mu m$ and the distance between these windows is in each direction approximately 2 mm.

The production process consists of eight steps and is illustrated on the left hand side in Fig. 6.8.

The **first step** is to support the stability of the membrane by plasma-enhanced chemical vapor deposition (PECVD) of silicon dioxide (SiO_2). Preferably this is done from the "back"[d] in order to avoid the formation of ripples on the membrane or even rupture of the membrane.

The **second step** is an electron beam lithography[138,139] process. With a scanning electron microscope (SEM) a PMMA[e] positive resist, which is previously spin coated onto the top face of the sample, is exposed and developed[139,140] using a mixture of MIBK[f] and IPA[g].

Afterwards in the **third step** a layer of gold is deposited onto the top surface, e.g. by thermal evaporation. After a lift-off process in acetone only the ring electrodes, conductors and bond pads remain (compare Fig. 6.9).

Then in the **fourth step** an optical lithography process using a positive resist follows. A general purpose mask has been used to expose the entire area of the twin aperture sample except for the bond pads. After development the bond pads will remain covered with the resist until step seven is finished.

Steps five to **seven** are simple steps during which SiO_2 and Au are deposited onto the top of the sample as known from previous steps. Additionally a golden bottom layer is deposited — by thermal evaporation for thin layers or galvanization for a thick layer (see Table 6.1). Afterwards the optical resist is removed in a lift-off process using acetone.

Finally in **step eight** the aperture holes need to be etched or milled into the sample. In a convenient way this can be done using a focused ion beam (FIB) inside a SEM. As pointed out in Ref. [62] FIB milling can lead to gallium contaminations at the resulting cylinder face of the milling hole, which the author suspects to increase chances of short circuits and electrostatic

[d] The side from which the wafer is etched.
[e] Poly(methyl methacrylate)
[f] Methyl isobutyl ketone
[g] Isopropyl alcohol

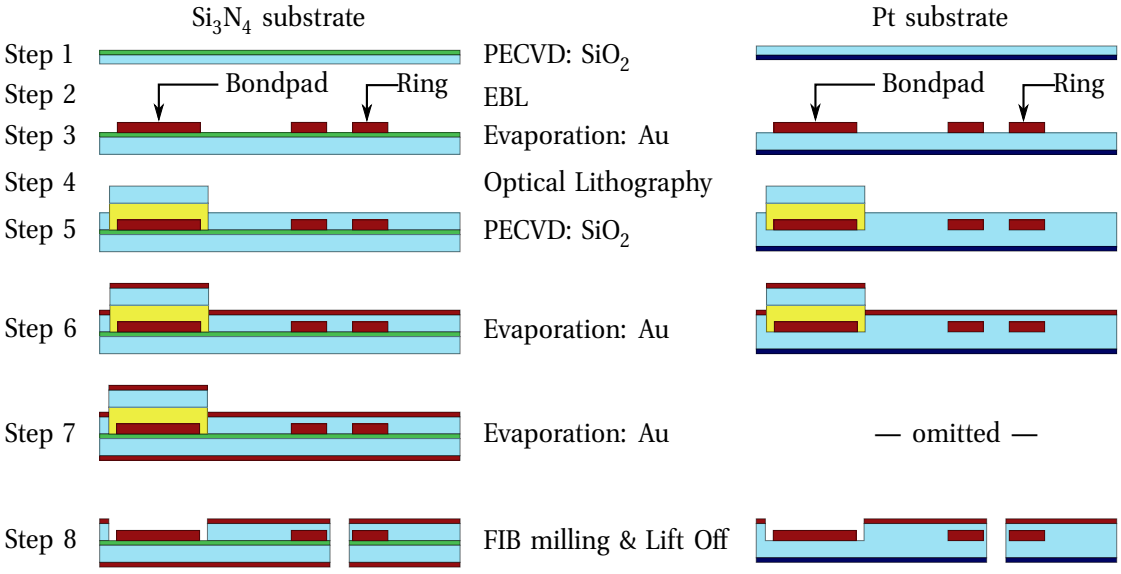

Figure 6.8.: Schematic partial cross sections of twin aperture during the production steps. The cross sections show one ring electrode and one bond pad, but not the line connecting both. On the *left hand side* the process is illustrated for a SiN substrate, on the *right hand side* for a Pt substrate. These schematics are not true to scale. **Green**: SiN, **blue**: SiO, **dark red**: Au, **dark blue**: Pt, **yellow**: PMMA.

charging. Therefore one might consider chemically assisted ion beam etching (CAIBE). But due to the smaller etching rates one would perform the step earlier, e.g. before optical lithography (step 4).

Fig. 6.9 shows SEM images of an actual Si_3N_4 membrane based phase plate. Subimage 6.9a shows the phase plate from the top (orientation as in Fig. 6.8: EBL structured layers are on the top). Due to the structure of underlying layers the top layer shows a relief of these layers. By means of FIB milling one can image the cross section of a discarded phase plate (see Fig. 6.9b). The image shows a cross section of an early generation twin aperture with different layer thicknesses containing a ring electrode. The milling area is indicated by the red rectangle in Fig. 6.9a.

In the course of this work electric charging in the phase plate was a serious issue. Given the electron penetration depth calculation in Sec. 5.3 the thickness of the bottom layer has been varied over a large range. Table 6.1 lists the layer thicknesses for the two different phase plate generations presented in chapter 7.

In the experimental part of this work (see Chap. 7) the deficiencies of both SiN based generations will be investigated.

[h] Layer thickness was limited due to depletion of electrolytic solution.

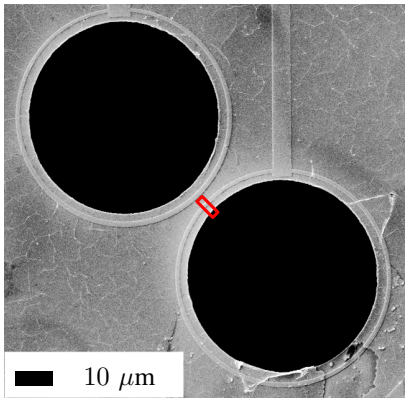

(a) Top View.

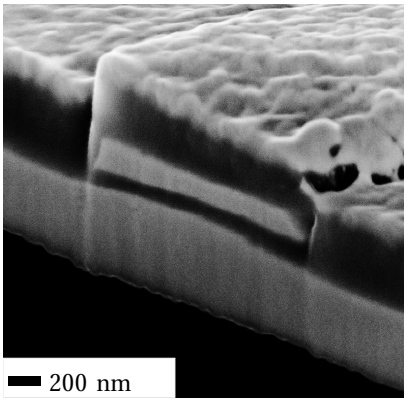

(b) Cross sectional View.

Figure 6.9.: SEM images of membrane based phase plates. **(a)** Underlying structured layers cause a relief in the top layer allowing to recognize these underlying layers. The region marked by the red rectangle has been milled away. **(b)** Cross section of phase plate has been prepared by FIB milling.

Step	Layer	Thickness
1	SiO_2	0.4 μm
3	Au	0.1 μm
5	SiO_2	0.4 μm
6	Au	0.1 μm
7	Au	1 μm or 18 μm[h]

Table 6.1.: Layer thicknesses of Si_3N_4 based phase plates with a thin and "thick" bottom layer.

6.2.2. Substrate: Commercial Pt Foil

As pointed out in Ref. [62] and Chap. 7 "thin" phase plates can suffer from serious charging effects. As an alternative we have chosen to manufacture phase plates also from commercially available platinum foils with a thickness of 25 µm. This thickness has been chosen due to the calculations in Sec. 5.3.

The manufacturing process described in the previous section only needs a few modifications for the new substrate material (see right hand side of to Fig. 6.8).

In **step 1** the SiO_2 layer is deposited onto one face of the foil, which will be referred to as the top face in the following steps. **Step 7** is entirely omitted as the Pt foil is already a metallic layer of desired thickness.

Milling or etching of platinum is a rather slow process, which makes techniques targeting an area — e.g. reactive ion etching (RIE) or CAIBE — a bad choice. Using a Zeiss Auriga FIB/SEM the milling process takes about 45 minutes during which the ion beam and sample have to be spatially stable with an accuracy of less than 1 µm. Each aperture hole milling process is split into two substeps. When starting from thick metal substrates first a hole with small diameter is

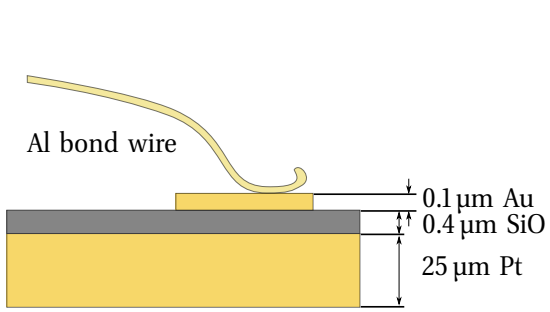

(a) Bonding problem.

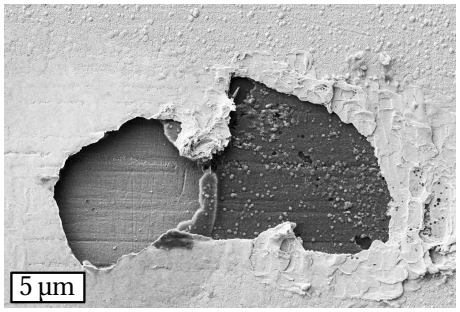

(b) Unsuccessful bond on dummy phase plate

Figure 6.10.: Schematic of bond problem and SEM image of remains of unsuccessful bond. Surface of a phase plate dummy made from brass (CuZn) after failed bonding attempt. What appears **bright** is the golden top layer, the **dark** parts are the SiO layers and **grey** is the brass substrate (compare Fig. 6.8).

milled using a high-current. Commonly high-current ion beams produce eroded edges. Thus in a second substep a low current focused ion beam is used to cut sharp edges (see twin aperture model `twin_ap_2D_X5_5` in Fig. 3.4f). Unfortunately the available machine could not always fulfill the stability conditions. Thus the obtained aperture holes have no sharp annular edges.

Having produced a twin aperture with Boersch phase plates one is still facing problems. Wire bonds on this type of twin aperture suffer from either one of the following problems:

Short Circuit — All wire bond connections established on Pt based twin apertures show a resistance smaller than 0.4 Ω. Investigations of cross sections (prepared by FIB milling) suggest that the insulating layer gets pierced due to application of ultrasonic waves in the bonding process. Furthermore surface roughness of the commercial foils might contribute to establish an electrical connection between the Pt substrate and Au bond pad.

Adhesion — The adhesion between the layers of the sample is not optimal for wire bonding. In most cases the bond wire removes a considerable area of the deposited layers such that the Pt substrate or SiO layer becomes visible (see Fig. 6.10b).

Due to these technical difficulties we were unable to construct a working twin aperture based on a Pt substrate that would have allowed application of a potential to one ring electrode exclusively. For future attempts one would have to consider a thicker substrate and insulating layer[141] in order to increase mechanical stability and avoid the possibility of the wire bond to pierce through the SiO layer.

6.3. Manufacturing of Customized C2 Aperture Holder

The default aperture and sample holders for a transmission electron microscope (TEM) have no means to allow an electrical connection between an electrode at the tip of the holder and a power source on the outside of the microscope. Therefore a new holder had to be designed and manufactured for the needs of this thesis.

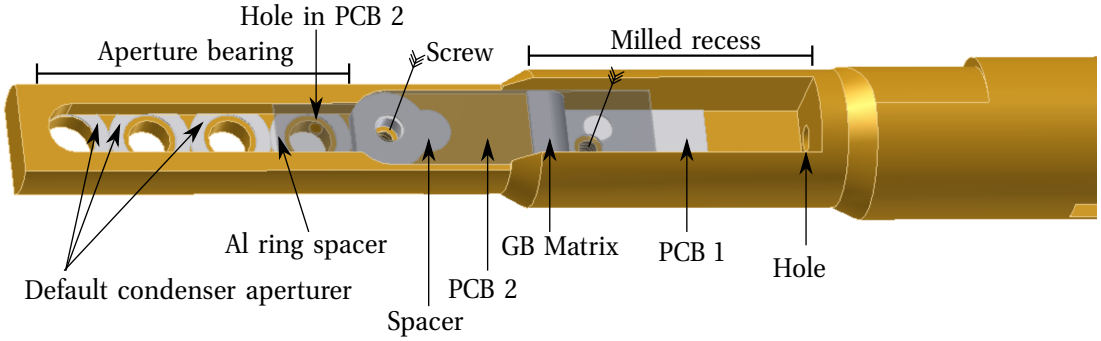

Figure 6.11.: CAD drawing of tip of custom condenser aperture holder. The holder accepts up to three default annular apertures and an aluminum ring spacer keeping the apertures in place. Above this spacer the twin aperture fixed to the PCB is located. By means of an interconnector sheet (GB Matrix) a connection between the PCBs is ensured.

In the designing process the original construction of the condenser aperture holder and a customized sample holder with electrical feed through designed by Thomas Haug[142] were used as sources of inspiration. The new holder design has to fulfill only a few requirements:

- allow the mounting of three conventional apertures;
- allow the mounting of a twin aperture;
- provide means for electrically connecting the twin aperture to an external power supply.

The new design basically is a modification of the original aperture holder design. The spring operated piston, which is intended to fixate apertures in the holder, has been omitted in the new design due to several reasons.

Fig. 6.11 shows a CAD drawing of the new holder design in which the printed circuit board PCB 2 is semi-transparent. An aluminum ring ($\varnothing_1 = 3.05\,\mathrm{mm}$, $\varnothing_2 = 2.0\,\mathrm{mm}$, $t = 0.1\,\mathrm{mm}$) is inserted into the bearing to replace the fourth aperture. The bore — designed for the insertion and removal of apertures from the bearing — is filled with a fitting brass spacer. By means of this spacer the standard apertures and the Al ring are kept in their positions.

Wafer pieces carrying the SiN membrane based phase plates have a cuboid shape (approximately $2 \times 2 \times 0.4\,\mathrm{mm}$). Such a wafer piece can not be inserted into the holder without further measures as it can not be fixated in the bearing designed to receive 100 µm thick apertures. The opposite problem arises for Pt foil based twin apertures which do not have a sufficient mechanical stability and would fold too easily, if the default spring loaded piston was used.

Furthermore manual soldering or welding of wires onto contact pads (size $\approx 100\,\mu\mathrm{m} \times 200\,\mu\mathrm{m}$) is almost impossible. Therefore a different technique is required. By wire bonding the contact pads are connected to connectors on PCB 2[143]. This PCB has a small hole at its tip, where the twin aperture is mounted, allowing the electron beam to pass. As this PCB is an obstacle in the optical path it requires a metallic back in order to avoid charging effects in the PCB substrate.

Behind the bearing for the apertures and the spacer a recess is milled (right hand side of *Spacer* in Fig. 6.11). From the back of the holder (not shown in Fig. 6.11) a hole is drilled by

wire-electro discharge machining in order to allow wires being fed from the outside through this hole into the recess housing PCB 1. These wires are soldered[143] to contacts on PCB 1. The hole is afterwards sealed with a vacuum epoxy[i].

PCB 2 carrying the phase plate will be mounted bottom up as shown in Fig. 6.11 by means of two small screws such that the hole in PCB 2 is concentric to the last bore on the aperture bearing and such that the conductor paths on both PCBs are facing each other. By means of an interconnector[j] sheet placed between the PCBs electrical connection between the opposing conductor paths on both PBCs is ensured.

In the appendix Sec. A.1 the interested reader can find further CAD drawings of the holder and the PCBs.

[i] Varian Torr Seal

[j] http://shinpoly.com/products/interconnectors/gb_matrix01.shtml

7. Experiments

In the previous chapters we have derived the theoretical foundations for the application of a twin aperture in EMCD experiments. Furthermore we have also pointed out potential problems specific to the different substrate materials.

Now we want to determine the optical properties of the microscope required for the calculations in Chap. 5 and evaluate whether the theoretical predictions regarding probe formation can be confirmed.

As previously mentioned in Sec. 6.2.2 the holes of the Pt based twin aperture — shown in Fig. 7.1 — have no sharp edges due to complications in the FIB milling process and there appear to be quite some contaminations that lead to azimuthal fringes and obstacles within the annular apertures. These defects give rise to disadvantageous effects in the experimental results presented in this chapter.

First we will measure the convergence semi-angle of the microscope in Sec. 7.1 and proceed in the following Secs. 7.2 and 7.3 by investigating SiN based twin aperture specimens for their suitability as condenser apertures.

Sec. 7.4 will focus on the electron probe formation due to Pt based apertures. We will compare the achieved spot diameters with those obtained using default C2 apertures.

7.1. Convergence Angle

In Sec. 5.2 Fourier transformations were used to calculate the electron probe in the specimen plane caused by an object in the aperture plane. As these Fourier transformations also transform the coordinate system (real space $\leftrightarrow$ Fourier/reciprocal space) we require the focal length f of the condenser system or the convergence (semi-) angle α in order to convert the one system into the other.

Fortunately the convergence (semi-) angle can be rather easily determined from measured convergent-beam electron diffraction (CBED) patterns, which one can see directly on the TEM screen and acquire with a camera[55].

Fig. 7.2 shows a schematic ray diagram for the generation of CBED patterns. First the microscope is adjusted to acquire a normal electron diffraction pattern by selecting a large illumination area on the sample and focusing the diffraction lens to the diffraction pattern. Then the condenser system is used to create a cross-over[a] in the sample plane. The observable width a of the diffraction disks in the CBED pattern is proportional to the full convergence angle 2α. Knowing the Bragg angle θ one can derive a value for the unknown α[55].

[a] Verification with shadow image; see Secs. 6.1.5 and 7.4.2.2

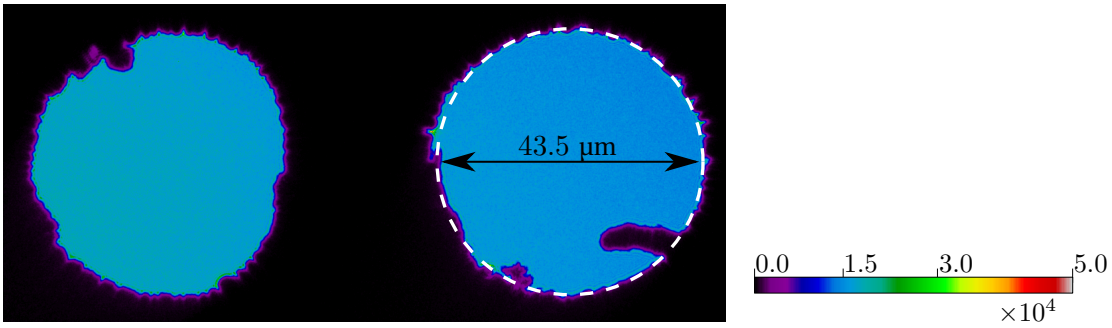

Figure 7.1.: TEM image acquired in absence of a sample in the specimen plane. The platinum twin aperture installed in the condenser aperture plane shapes the electron beam. The colorbar indicates the number of counts on the CCD camera. Quality of beam contour is decreased due to rough edges and contaminations (from FIB milling) on the aperture. Aperture on the right hand side is approximated with a circle (dashed white line) and shows a diameter of 43.5 µm, which has been determined from a SEM image. Deviations to the values assumed in Chap. 5 are caused by misalignments of the FIB milling software.

$$\sqrt{h^2+k^2+l^2}\lambda = 2d\sin(\theta) \tag{7.1}$$

$$\theta_{hkl} = \arcsin\left(\frac{\sqrt{h^2+k^2+l^2}\lambda}{2d}\right). \tag{7.2}$$

Using Eq. 7.2 one can calculate the Bragg angles in dependence on the lattice spacing d and wave length λ. h, k and l are the three indices of the Bragg beam. As indicated in Fig. 7.2 one can derive the convergence angle α by evaluating the relation[55]

$$\alpha = \frac{a}{b}\theta_{hkl} \tag{7.3}$$

$$= \frac{a}{b}\arcsin\left(\frac{\lambda\sqrt{h^2+k^2+l^2}}{2d}\right). \tag{7.4}$$

During the evaluation of one acquired CBED pattern (see Fig. 7.3) one can refer to many different Bragg reflexes hkl. Acquisition was performed with spot size **5** for all C2 aperture sizes. Evaluation of these CBED patterns yields the convergence angle α as shown in Table 7.1.

Having determined the convergence angle for the standard C2 apertures we can proceed with fitting these experimental values with a function as shown in Fig. 7.4. As fit function we have chosen an arc tangent as we have experimentally determined the convergence angle of the entire condenser system. As a lens system can be treated as a single lens as in the schematic setup (see Fig. 2.3) one can conclude

$$\tan(\alpha) = \frac{R}{f}, \tag{7.5}$$

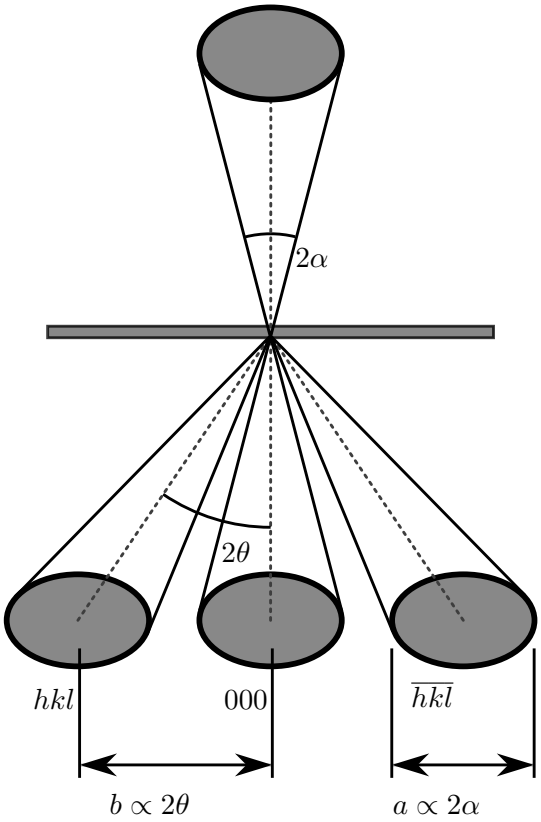

Figure 7.2.: Ray diagram for convergent-beam electron diffraction (CBED). After setting up the microscope for "parallel" illumination a focused probe on the sample results in large diffraction disks. Knowing the Bragg angle θ one can calculate the convergence angle α.

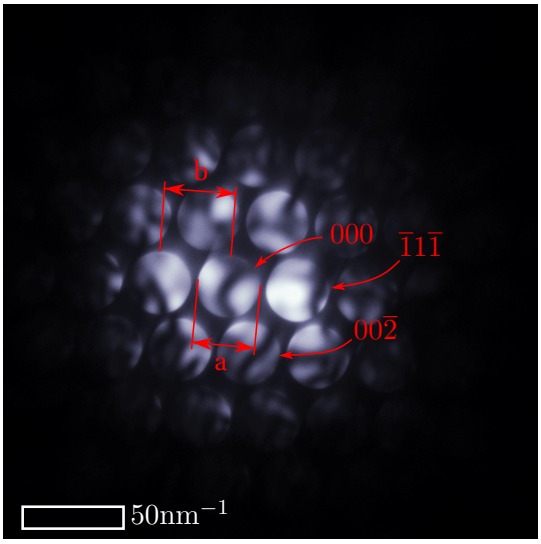

Figure 7.3.: TEM image of CBED pattern of GaAs oriented in [110] direction for standard 100 µm C2 aperture acquired at 200 kV. The image illustrates how and where a and b have beam measured.

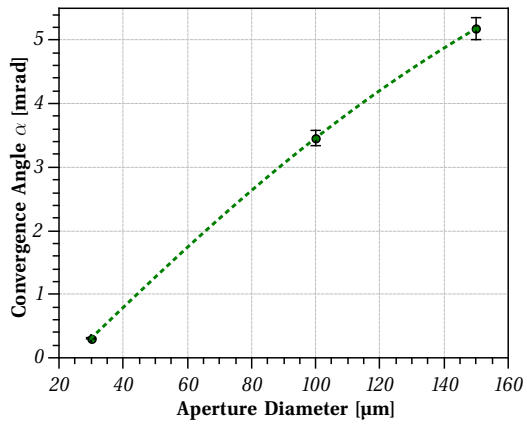

Figure 7.4.: Experimentally determined convergence angle in dependence of C2 aperture diameter and function fitted thereto.

⌀ [µm]	α [mrad]
30	0.31 ± 0.01
100	3.5 ± 0.1
150	5.2 ± 0.2

Table 7.1.: Experimentally determined convergence angle α in dependence of C2 aperture diameter for spot size **5**.

where R is the aperture radius and f the focal length of the entire condenser system. Thus an arc tangent is a good choice for the dependence of α on R. The fit function $\alpha(R)$ is given by

$$\alpha(R) \approx 8 \arctan\left((12R - 200\right), \tag{7.6}$$

where R and α are of units µm and mrad, respectively.

Finally we can derive realistic parameters for the simulations of Sec. 5.2. An aperture radius of 29 µm is equivalent to 1.65 mrad. The displacement from the optical axis of 33.2 µm is equivalent to a tilt angle of 2.03 mrad.

7.2. Thin Twin Aperture

The first generation of twin apertures followed the construction process of Boersch phase plates with similar layer thicknesses. Unfortunately the layers were not sufficiently thick to prevent electrostatic charging of the insulating layers. This led to strong astigmatic effects as the inability to create a cross over (see Fig. 7.5) on the nanometer scale.

In this short section we will perform measurements on thin SiN based twin apertures (see Sec. 6.2.1) to support the claimed correlation between electrostatic charging and aberrations.

7.2.1. Differential Phase Contrast Measurements

Compared to the detection limit of the used DPC detector[81,146] the applied potential to the ring electrodes of the twin aperture arrangement produces an electrical field that is below the detection limit of the setup. Using a best case approximation we expect the strongest field, where the distance between the ring electrodes is smallest — a region that is considered as opaque for the electron probe. For an applied voltage of 10 V this field would be a factor 3 smaller than the detection limit determined by Ralph Schregle[146]. As the following measurements are performed in low magnification STEM (LM-STEM) mode we furthermore expect a larger detection limit.

Even as the phase shifting potential cannot be mapped by using the DPC technique it is very helpful in recording time-dependent charging effects on a scale of 1-60 mins. For the following measurements the twin aperture was inserted in the specimen plane by means of a customized sample holder designed by Thomas Haug[142], which provides 3 channels for electrical contacting.

Fig. 7.6 illustrates how each DPC measurement is evaluated in order to extract the time-dependent effects of electrostatic charging from an acquired time series. As one can see in

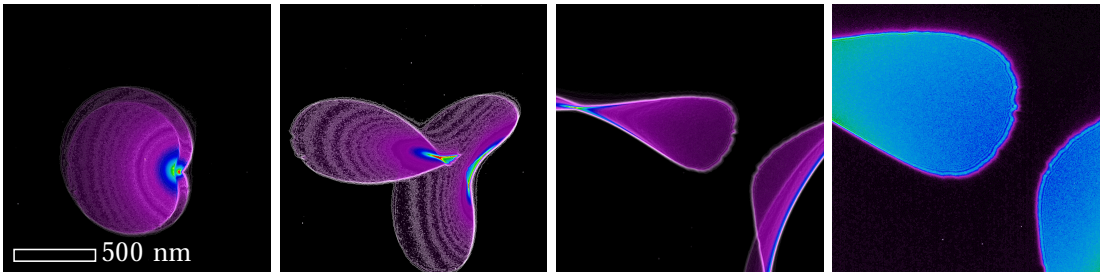

Figure 7.5.: Focal series in TEM µProbe mode. "In focus" on the left hand side; increasing defocus to the right. Strong threefold astigmatism (confirmed by P. Tiemeijer, FEI; see appendix Sec. A.9) prevents an actual common cross-over on a nanometer scale. Each image is constructed as a superposition of an opaque output of the Sobel operator[144,145] and a transparent version of the image itself, where the color black has been replaced by transparency.

the upper left and right plots the DPC image contains a radial symmetric gradient in the background, which is a stationary byproduct of the low magnification scanning mode (LM-STEM). This gradient can be minimized with an accurate alignment, but in the investigation of the time-dependent changes to the signal due to electrostatic charging this gradient has no significant influence on the results due to its staticity. DPC images with and without this background gradient indicate similar time-dependent behaviors.

By means of two annular masks (red circles in upper left plot in Fig. 7.6) points in the DPC image are selected for further statistical evaluation. The radial and azimuthal component of the deflection vector at each point are treated separately. For each component and aperture the histogram is shown in the lower plots (radial: lower left, azimuthal: lower right) to give a visual impression of the data used for further analysis. For each data set the mean deflection vector in polar coordinates $(\mu_r \pm \sigma_r,\ \mu_\phi \pm \sigma_\phi)$ is calculated, where μ_i is the mean value and σ_i the standard deviation. For the data set shown in Fig. 7.6 these vectors are

$$\vec{A} = \begin{pmatrix} (9 \pm 4) \cdot 10^3 & \text{[a.u.]} \\ -5 \cdot 10^{-2} \pm 1 & \text{[rad]} \end{pmatrix}, \tag{7.7}$$

$$\vec{B} = \begin{pmatrix} (3.8 \pm 0.7) \cdot 10^4 & \text{[a.u.]} \\ 0.7 \pm 0.2 & \text{[mrad]} \end{pmatrix}, \tag{7.8}$$

where $\vec{A}$ is the mean deflection vector in the aperture in the upper right corner of the DPC image in Fig. 7.6.

Having evaluated all images one can plot the temporal dependence of the deflection vector's length on a time axis as in Fig. 7.7 or furthermore regard the azimuthal component in a polar plot as in Fig. 7.8. The applied voltage between the two ring electrodes is plotted on the right hand side axis in Fig. 7.7. For measurements 1 to 39 one ring electrode was connected to the microscope's ground terminal while the voltage was swept at the other electrode; afterwards the connection to ground was swapped and the voltage sweep performed on the first electrode.

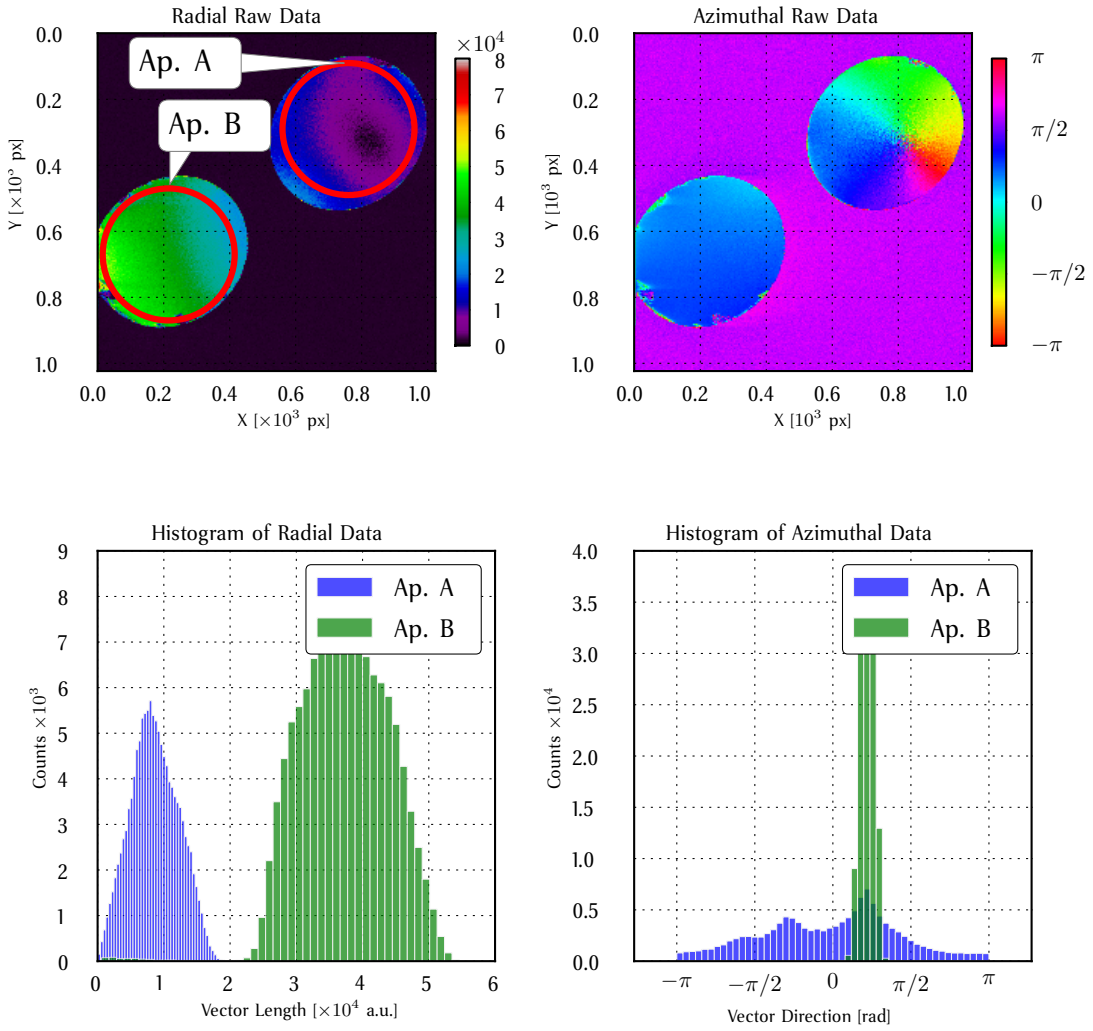

Figure 7.6.: Statistical evaluation of one DPC measurement showing two holes of the twin aperture. For each hole of the twin aperture the mean value and standard deviation of the strength (upper left plot) and direction (upper right) of the deflecting forces are determined. To allow automated evaluation only points within the red circle — stationary in all DPC images — are regarded. The lower left and right plots show histograms for each aperture hole of the absolute of the deflection and its direction. In the low magnification scanning mode (LM-STEM) the DPC signal shows an ellipsoidal offset independent of the specimen.

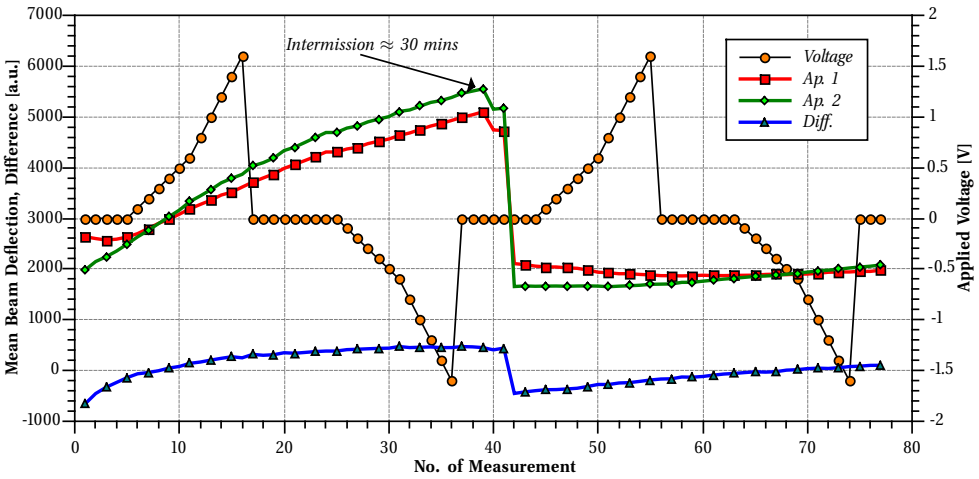

Figure 7.7.: Time dependence of the radial component of both aperture holes. For a polar plot that includes the azimuthal component see Fig. 7.8.

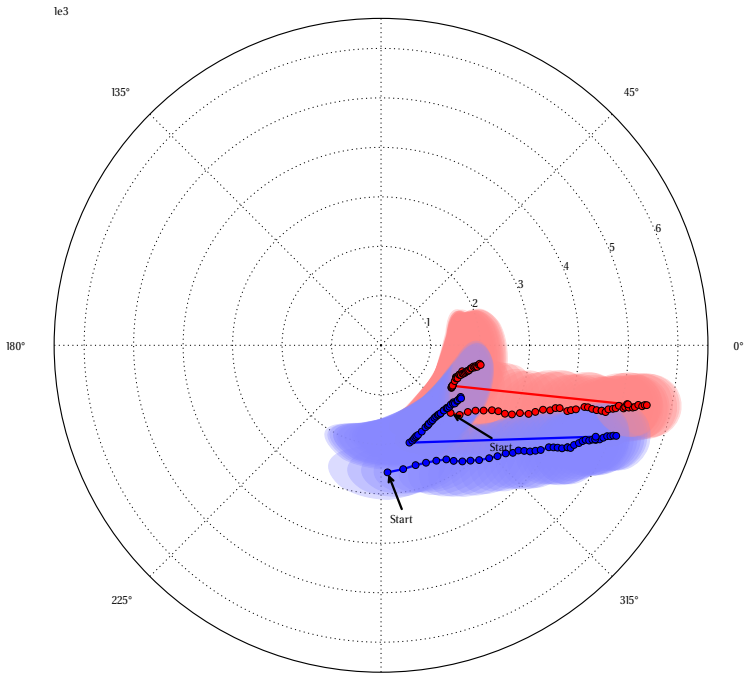

Figure 7.8.: Time dependent mean beam deflection for beams passing through both holes of the twin aperture. Standard deviation has been used as a basis for the generation of error ellipsoids. The same measurement data has been used as for Fig. 7.7. For polar plots of further measurements see Sec. A.6.

For applied potential see the **orange** line with circle markers. Between the measurements with numbers 39 and 40 acquisition was paused for 30 mins.

The mean deflection in each aperture (**red** and **green** curves) is increasing during the first 39 measurements independently of the applied voltage. After the intermission the deflection has decreased slightly, but continues its trend until measurement 42, in which the amount of the deflections is reduced to values close to the initial ones. Afterwards the deflecting forces are increasing again. As one can see from the difference of the two curves the applied potential shows no noticeable effects. The difference curve shows resemblance to the charging curve of a capacitor, which is a first indication of a charging effect in the twin aperture.

A polar trace plot in Fig. 7.7 (see also Fig. A.13) conveniently illustrates how these charging effects influence the direction of the beam deflection. The mean deflection vectors for each aperture — disregarding any initial offsets — show in each plot a synchronized behavior.

During the acquisition of DPC images the focused electron probe is scanned over a quadratic area larger than the twin aperture (see Fig. 7.6). The time dependent mean deflection nicely shows how a relatively broad statistical distribution of deflection vectors[b] gets influenced by a charge accumulation. During the measurements for Fig. 7.7 the direction of both mean deflection vectors changes by an amount $\lesssim 3/8 \cdot \pi$ in a very synchronous way. This suggests that the accumulated charge is not symmetrically distributed around the annular aperture holes, which is rather obvious as the scanning area, across which the focused electron probe is scanned, is quadratic.

At this point we will not proceed in the treatment of the dependence of the mean deflection vector on charge accumulation as our goal is to eliminate such effects.

The DPC measurement of this section do not explain the initial problem of threefold astigmatisms illustrated in Fig. 7.5, but point out the general problem of electrostatic charging. The following measurements will be performed with the twin aperture inserted as C2 aperture with the holder described in Sec. 6.3.

7.2.2. Resistance Measurements

Due to the distortions and aberrations presumably caused by electrostatic charging we will perform measurements of the resistance between the ring electrodes (compare Fig. 7.9).

Let us start with a thought experiment. Imagine the ring electrodes of the twin aperture to be the *source* and *drain* of a field effect transistor (FET; compare Figs. 3.4, 6.9 and 7.9). The top layer, which is exposed to beam electrons, would be similar to the *gate*. These metallic contacts we might consider as very strong n-type doped regions of a FET. The silicon compounds (Si, SiN, SiO) between the ring electrodes, to which we will refer occasionally as *bulk*, are typical insulators; thus one would expect that the conductivity of this device is very low.

Due to the lack of doping of the silicon compounds no space-charge regions can be formed at the interfaces to the source and drain. Thus a charge accumulation or potential application in the gate would have no effect on the conductivity of the transistor. But as we know from simulations (see Sec. 5.3) primary beam electrons (200 – 300 keV) have a considerable penetration depth. While travelling through the transistor material the primary electron has

[b] Larger error-ellipsoidals in polar plots.

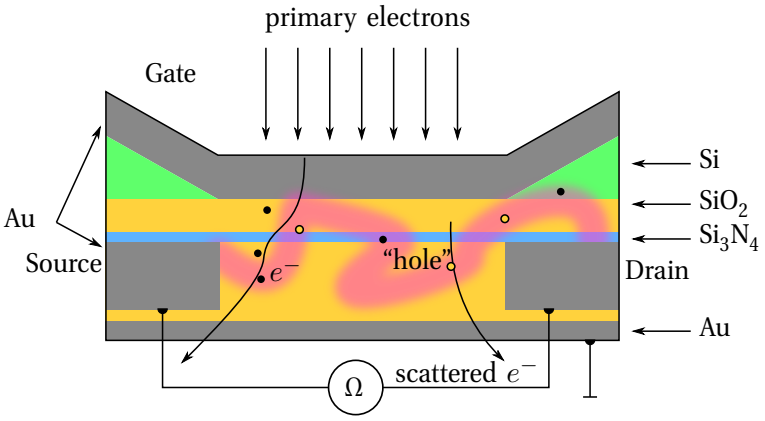

Figure 7.9.: Schematic cross section of twin aperture for thought experiment. The device is exposed to electron irradiation, which is generating space charges (black dots: e^-, black circles: holes) by various inelastic scattering processes. For a sufficient space charge creation rate a conductive channel (purple) is formed.

several interaction mechanisms that allow for the creation of a space charge, e.g. exciting an electron from a bound state to a free state in the conduction band (electron - hole pair) by inelastic scattering, stimulated emission of Auger electrons, etc.

By design the gate and the bottom layer are on a neutral potential. If the electron beam produces by means of the previously mentioned effects space charges with a sufficient rate — larger than the recombination rate — these charges should be able to carry a measurable current between source and drain. One might expect that the electron irradiation can inject more space charges in the thick silicon substrate. During electron irradiation one might consider the gate as being on a negative potential causing a conducting channel and thus increasing the conductivity of the device.

For this measurement the twin aperture was installed in the C2 aperture plane using the customized holder described in Sec. 6.3.

Fig. 7.10 shows a measurement of the resistance between the two ring electrodes. This measurement has been performed after an elongated exposure to the beam in order for the multimeter[c] to measure a finite resistance even when the illumination is turned off. Referring to the thought experiment the electron beam has to generate sufficient charge carriers in the silicon compounds before one can measure a resistance or conductivity. After this "doping" process the non-illuminated twin aperture shows a resistance of approximately 25 MΩ that is stable for several hours. Having a relatively large resistance the recombination takes a correspondingly long time.

When turning on the illumination (opening of column valves) the resistance drops within a couple of seconds down to another relatively stable value which is dependent on the illuminated area. The **black** line shows the resistance between the ring electrodes in absence of a C1 aperture. The resistance drops to $\approx 2.5\,\mathrm{M\Omega}$, where it is not especially stable. For the second measurement (**red** curve) the C1 lens (spot size) was set up such that with the largest available C1 aperture the illumination was limited to an annular area that just covered the holes of the

[c] Metering range $< 60\,\mathrm{M\Omega}$.

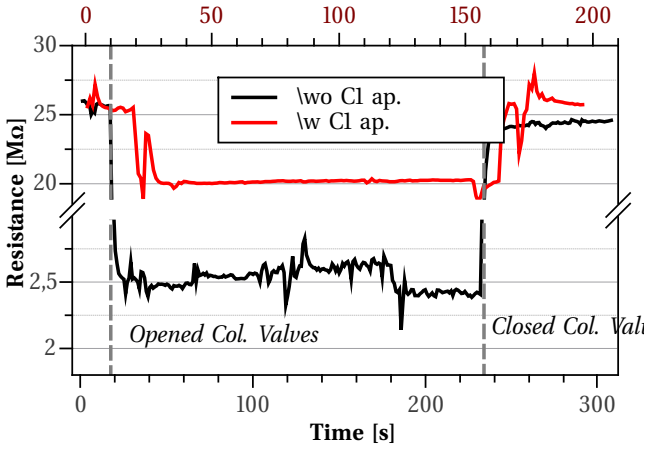

Figure 7.10.: Resistance measurement between ring electrodes with no applied potentials in dependence of electron beam exposure.

twin aperture and the resistance dropped only to a value of 20 MΩ.

This deviation of one order in magnitude can be understood by regarding the specimen geometry and the previous thought experiment. While the twin aperture is approximately only 1 µm thick at its central rectangular area, the thickness outside of this rectangle quickly increases up to 400 µm. Thus outside of the central rectangle the available volume to generate space charges is strongly increased and if this volume is illuminated more space charges are generated that can contribute to a higher conductivity.

Thus charging effects (absorption of primary electron) and electron-hole pair generation are serious issues for electrical circuitry that is inserted in the condenser system of a TEM. The use of "thin" metallic top layers is impossible; one definitely has to switch to thicker layers to prevent electron penetration.

In the following sections we will investigate the properties of electroplated Au top layers (Sec. 7.3) and the usability of Pt substrates (Sec.7.4).

7.3. Energy Dispersive X-Ray Investigations

In Sec. 5.3 it was shown that a thick Pt top layer of approximately 25 µm is required to ensure zero transmission for 200 kV acceleration voltage. For both designs suggested and described in Sec. 6.2 one can in principle create a thick top layer, but in case of the Si_3N_4 based design electroplating of Au was the only available technique to achieve a layer thickness of 18 µm within a reasonable time[d].

Unfortunately the used electroplating bath[e] contains traces of cobalt[147]. As Co is one of the prominent 3*d* ferromagnetic materials we conduct energy dispersive X-ray (EDX) measurements

[d] 12 hours of electroplating.
[e] WILAPLAT Glanzgoldplattierbad 750 SC

to determine whether the electroplated gold layer contains non-negligible Co concentrations that could lead to magnetic distortions in the aperture plane. Due to a defect in the EDX detector of the Tecnai F30 the measurements in this section were performed with a Philips CM30 with a LaB_6 cathode.

For these measurements two lamellas have been cut out of a broken SiN based twin aperture using FIB techniques. Fig. 7.11 shows TEM images of these lamellas; the black arrow between the lamellas indicates the direction along which FIB milling was performed. The particular specimen from which the lamella was prepared has not the full 18 µm thick layer. Therefore it was possible to prepare a lamella that also contains parts of the SiO and Si layers. As one can see the layer interface is not perfect as no epitaxial growth techniques were used. The measured thickness of the SiO layer is 350 nm (target value during PECVD deposition: 400 nm).

The TEM images allow a good distinction between the layers containing heavy elements (Au) and lighter ones (Si, O, ...). The lamella shown on the right hand side of Fig. 7.11 shows several distinguishable layers of silicon. This could be a result of various processes[f] the wafer piece was subject to.

To investigate the cobalt contamination of the lamella a line scan of EDX spectra (see Fig. 7.12) has been acquired along a line normal to the stacked layers. The red arrow in Fig. 7.11 and the green arrow in the small image above the line scan in Fig. 7.12 indicate where the line scan was acquired.

The line scan allows a good distinction between the Au layer and layers containing silicon. The thermally evaporated seed layers for electroplating contain a Cu layer as well. Thus it is not surprising to find Cu at the interface to SiO. The Au layer deposited by electroplating shows a noticeable amount of Co.

The direction of FIB milling using Ga ions was approximately along the direction of the line scan. During FIB milling Ga ions usually get implanted into the processed material, whereas the milled material usually is redeposited in the vicinity. This effect can be visualized nicely using a Ga-based specimen. Fig.7.13 shows the top surface of a GaN capped sapphire[g] substrate[79,81,148,149] into which a square of size 5×5 µm was milled. The milling area is outlined with a red dashed square. Milling started at the bottom face of the square and proceeded upwards. Material that is milled of in the upper half of the milling area is redeposited in previously milled cavities; in this special case of a crystalline Ga sample the redeposited material is building new clustered structures at the lower half of the square.

Thus one can observe redeposited heavy elements (Au, Cu, Co) in the underlying Si layers of the lamella. As expected we find a rather constant concentration of Ga as gallium is the abrading medium in the used FIB machine.

Focusing on the Co profile in the line scan we can see that the Co concentration has its maximum within the first deposited micrometers during electroplating. The acquisition/evaluation software[h] estimates an atomic Co concentration in the gold layer of approx. 7–8%. Considering that the twin aperture will be installed within an electron-optical lens with field intensities of a few Tesla this rather low concentration might be sufficient to modify the magnetic field locally

[f] Wafer growth, EBL processes (see Sec. 6.2.1), electroplating, FIB milling, ...
[g] Al_2O_3 substrate, $\approx$ 100 nm AlN, $\approx$ 4 µm GaN, ...
[h] Bruker Esprit

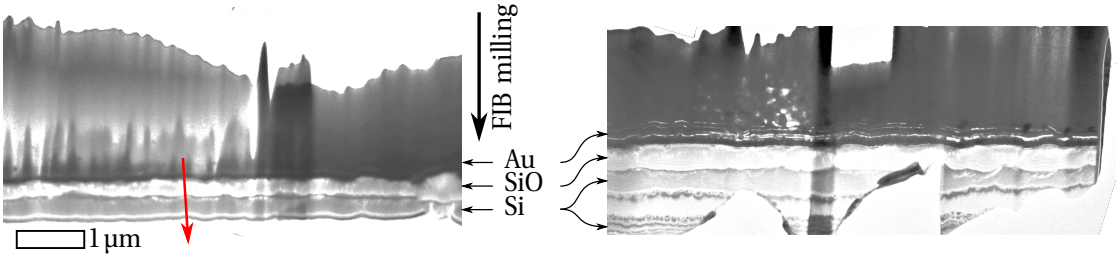

Figure 7.11.: TEM image of lamellas. Lamella is a cross section of several layers of the SiN based twin aperture. The direction of incoming ions is marked with a **black** arrow. Typically this direction is tilted out of the lamella's plane by 2°. **Red** arrow denotes where EDX line scans (see Fig. 7.12) have been performed.

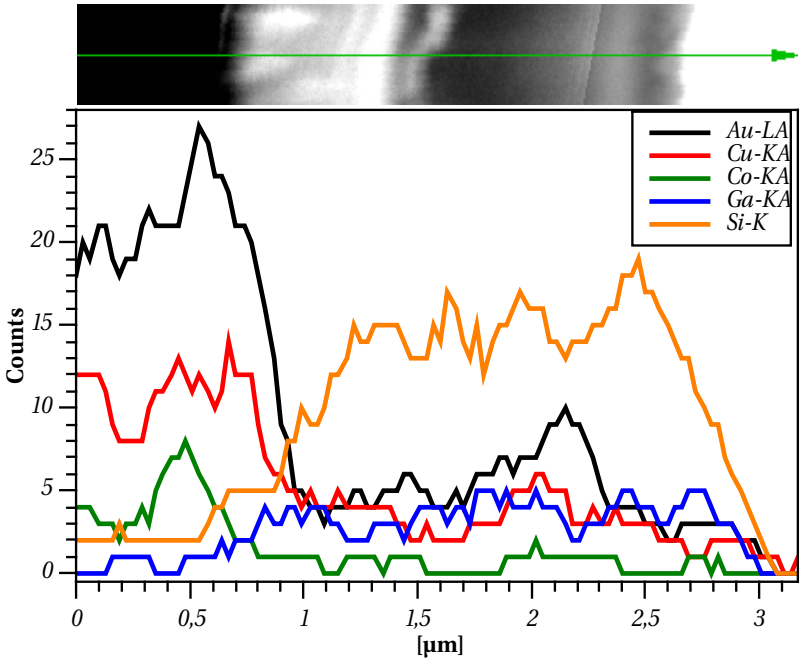

Figure 7.12.: EDX spectral line scan. Scaling of x-axis was not calibrated on the CM30 microscope.

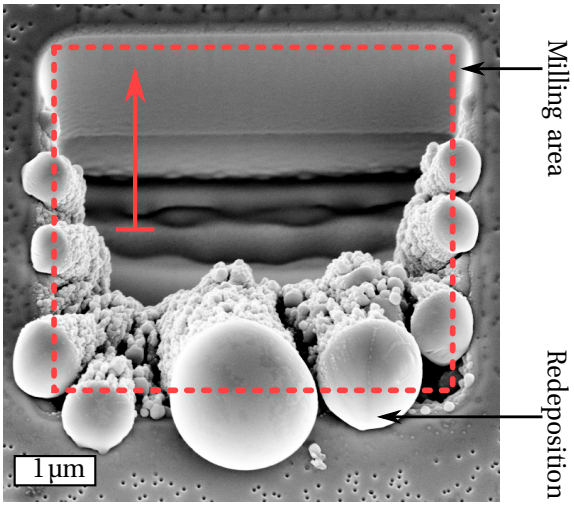

Figure 7.13.: SEM top view of GaN capped sapphire substrate after milling of a square of size $5 \times 5\,\mu m$ to a depth of $\approx 1.2\,\mu m$. Shape of the square (red dashed box) and milling direction (red arrow; ion beam is rapidly scanning along a line perpendicular to the milling direction. This line is constantly displaced in the milling direction) are indicated in the image. As the milling process progresses to the upper part of the square material milled at these upper parts is redeposited[150] at the lower parts. The strange form of the redepositions might be a result of the material being gallium — just like the ion beam. Outside of the milled area one can see small black dots, which are GaN pyramids[79,148].

and thus introduce non-correctable aberrations into the optical system. Thus a layer deposited from the available electroplating bath cannot be regarded as suitable for the task ahead without further evaluation.

Additionally, EDX mappings in Figs. 7.14 and 7.15 of both lamellas give a better understanding of the elemental distributions. Onto the bright field images of each lamella the Sobel operator[144,145] has been applied in order to generate a dark background image which only highlights edge features. Semi-transparent elemental maps (compare to Figs. A.14 and A.15) have been imposed on the background image. The resulting compositions are shown in Figs. 7.14 and 7.15, where the elemental maps are shown only in stripes in order to get a better impression of the actual elemental distributions. Figs. A.14 and A.15 show the original data (bright field image and elemental maps).

Figs. 7.14 and 7.15 illustrate well the elemental distribution of the heavy elements. In the electroplated layer one can observe a higher Co concentration, which has its maximum right after the seed layer. As this layer may contain further contaminations due to the electroplating it is not surprising to find a higher Au concentration in the seed layer, which was deposited by thermal evaporation in vacuum, than in the electroplated layer. Depending on the lamella the elemental maps indicate more or less redeposited heavy elements in the Si layers. This could be a side effect due to small differences in the FIB milling process or an artifact due to a non-optimal focus.

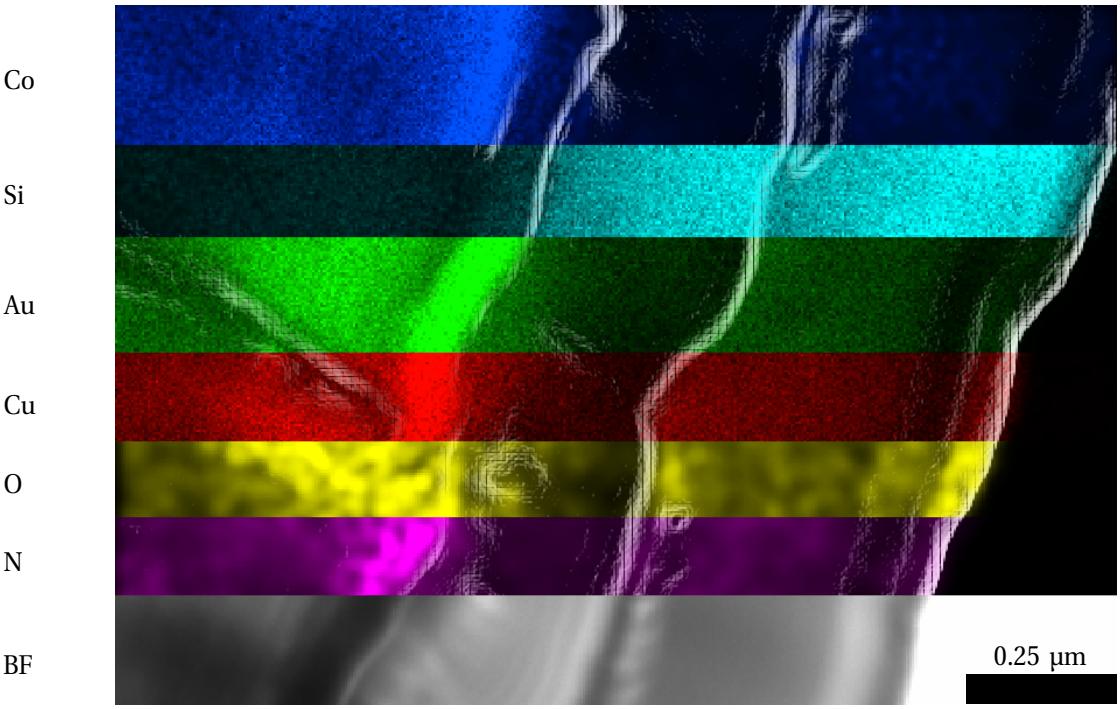

Figure 7.14.: Composition of EDX elemental maps. Maps have been acquired on **left** hand side lamella in Fig. 7.11.

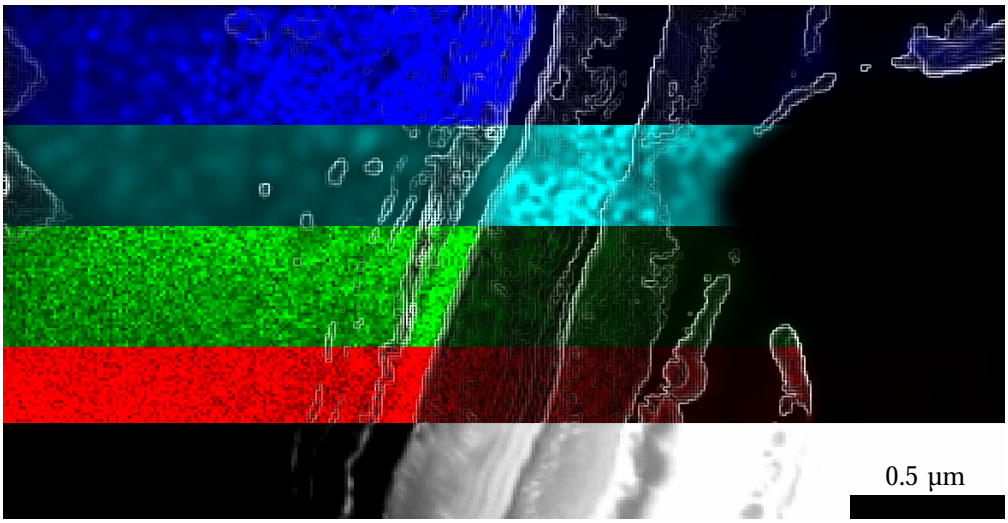

Figure 7.15.: Composition of EDX elemental maps. Maps have been acquired on **right** hand side lamella in Fig. 7.11. For elemental legend refer to Fig. 7.14, where elemental maps appear in the same order and color.

In conclusion the electroplating of Au can not be regarded as a success due to the non-negligible concentration of Co in the deposited layer. Unfortunately most plating solutions contain ferromagnetic elements[151]. For future work on this topic plating solutions containing indium alloys or solutions for the deposition of Pt[152,153] might be of interest.

7.4. Spot Size Analysis

One question arising from the calculations presented in Chap. 5 is how well these calculations describe the actual spot in the specimen plane. Due to the well known types of astigmatism[42,55,91], the deviation from a plane wave illumination and the lack of quantitative numbers for the phase shifting models an experimental determination of the diameter of electron probes is required.

In order to get an idea of the spot size and shape based on experiments one basically has three choices:

1. Acquire an image of the spot with a CCD camera.
2. Acquire a STEM or differential phase contrast (DPC) line scan across a sharp edge and reconstruct the spot size[81].
3. Acquire an image of electron induced in-situ deposited[154] residual material.

In the following subsections we will investigate the first and last option as those rely on no assumptions, whereas the method in the second option assumes a radially symmetric Gaussian beam profile for the reconstruction of the electron probe shape. As pointed out in Sec. 5.2 the radial symmetry is broken by the twin aperture which could lead to complications.

In Secs. 6.2.1, 7.3 and 7.2.1 we have shown the deficiencies of SiN based twin apertures — basically due to the too thin top layer. Thus they are not suitable to be used as condenser apertures. The experiments in this section were only performed with a Pt based twin aperture (see Sec. 6.2.2) inserted to the C2 aperture plane.

7.4.1. Acquisition with CCD Camera

The acquisition of images that contain only a few spots of intensity is usually considered a bad idea as a focused spot very easily can deliver a critical number of electrons to a few pixels of the camera, which will lead to over exposition. In the best case this only leads to saturation in the acquired image or imprinting of artifacts on the image. In the worst case these artifacts could become permanent or parts of the camera, e.g. the scintillator, could be damaged. Especially when operating the CCD camera close to saturation one has to regard blooming[155], which is the diffusion of electrons from saturated pixels to neighboring ones.

Taking precautions to avoid these problems one has to regard one minor issue. The acquisition software[i] offers a scale bar marker, which is adjusted for the projector system being focused to the eucentric plane; this is a reference plane in which a point on the optical axis does not

[i] Gatan Digital Micrograph

move laterally when the specimen is tilted around the holder axis[55]. In order to image the shape of the cross-over in this plane the imaging and illumination systems need to be focused accurately to this plane. Otherwise a slightly magnified version of the cross-over is projected onto the camera.

Fig. 7.16 shows the image of a focused spot produced with the twin aperture (Fig. A.16 shows a focal series with a similar cross over) acquired at an acceleration voltage of 200 kV. As indicated in the image on the left line scans have been performed to determine the diameter of the spot. The line scan data has been fitted with a Lorentzian[156–159] (continuous lines in Figs. 7.16-7.18) of the shape

$$f(x) = y_0 + \frac{A}{\pi}\frac{w}{(x-x_0)^2 + w^2}, \tag{7.9}$$

where y_0, A, x_0 and w are fit parameters. Of interest is the fit parameter w as it specifies the half-width at half-maximum (HWHM). The beam diameter can be defined using different quantities (Full-Width at Half Maximum (FWHM), $1/e^2$ width, ...).

Alternatively a Gaussian fit function could have been chosen; data acquired under good conditions — standard 100 µm aperture — is best fit with a Gaussian as the interested reader can see in Fig A.21, but data acquired during the use of the twin aperture shows a number of distortions and artifacts, which are more conveniently covered by a Lorentzian (e.g. see Figs. 7.16 and 7.17) as it is by default broader than a Gaussian distribution. As all quantities of the form "Full With at $1/n^{th}$ Maximum" (FWnM) are related by the expression

$$\begin{aligned} \mathrm{FWnM} =& 2\sqrt{n-1}\cdot w \\ =& \sqrt{n-1}\cdot \mathrm{FWHM} \end{aligned} \tag{7.10}$$

we can choose $2w$ (FWHM) as definition of the beam diameter for the sake of simplicity. Thus one can determine the spot diameter directly from the fitting parameter. The first column in Table 7.2 shows the results of this process for data retrieved from Figs. 7.16 and A.18a.

Table A.2 reveals a typical problem of this kind of measurement, the resulting spot diameters depend on environmental quantities and conditions like spot size, stigmator settings and others[j]; this makes a quantification difficult especially when the microscope shows instabilities[k]. The averaged spot diameters for 200 kV in Table 7.2 agree with the expectation, that a smaller aperture produces a larger spot.

Despite using a Lorentzian for fitting experimental data we know from theory (see Chap. 5) that an electron probe's wave function is dominated by a Bessel function. Taking a closer look at the Bessel function describing the cross-over

$$\frac{1}{2\pi Rq} J_1(2\pi Rq), \tag{7.11}$$

where R is the aperture radius and q the Fourier space coordinate in the back focal plane (plane of the cross over), one would expect that switching from an aperture diameter of 100 µm

[j] Use of a different user's alignment can change the observable FWHM by a factor 2.

[k] Charging effects & beam wobbling, specimen drift,....

$2w$ [nm]			
200 kV gun 5, spot 5		**300 kV** gun 5, spot 5	
Twin Ap.	100 µm Ap.	Twin Ap.	100 µm Ap.
7 ± 2	4 ± 1	1.8 ± 0.2	1.7 ± 0.3

Table 7.2.: Spot diameters determined from line scans of cross-overs for different investigated cases: twin aperture at 200 kV (see Fig. 7.16 and Table A.2) and 300 kV (see Fig. 7.17 and Table A.4) & 100 µm standard C2 aperture (see Fig. 7.18 and Table A.5).

to 43.5 µm increases the spot diameter (FWHM) by a factor of approximately 2.3. Regarding that this value is determined for a theoretical, ideal microscope with coherent illumination and that the beam shape is quite poor (see Fig. 7.1) one should not be surprised to get a deviation from this value. From the mean values in Table 7.2 one obtains a value of 1.75, whereas for certain measurements this value can rise to 2.4.

In Sec. 5.3 we had used a Monte Carlo simulation to determine a sufficient thickness of the twin aperture's top layer to avoid penetration of the underlying insulating layers by 200 keV electrons. But Fig. 7.17 has been acquired with 300 kV electrons and also shows both beams converging into a common cross-over point. Being able to observe a single cross-over point also for 300 kV is promising for the usability of twin apertures based on Pt substrates.

Unfortunately the measured spot diameter for 300 keV electrons shows no significant dependence on the aperture size as in the 200 keV case. The ratio between the spot diameters — for twin aperture and 100 µm aperture — ranges from 1 to 1.6. In order to understand this lack of change in spot diameter one might consider the simulation results (see Secs. 4.3.4.3 and 5.3) which predict that primary electrons will penetrate the Pt and insulating layers. Arguing with the thought experiment from Sec. 7.2.2 these electrons are decelerated — thereby creating electron-hole pairs — until they can be considered as bound electrons; thus due to the trapping of decelerated primary electrons a predominantly negative space charge will be accumulated. These accumulated charges, if treated as an electrostatic lens, introduce a converging phase term: the beams passing through the aperture holes are deflected towards the center of each aperture hole. Thus the focal length of the condenser system becomes effectively reduced. In terms of the mathematical formalism this electrostatic lens has no influence on the size of the spot in Fourier space coordinates, but when transforming these into real space coordinates ($x = f\lambda q$) one gets a smaller spot diameter than without accumulated charges.

Focal series acquired for both 200 kV (see Fig. A.16) and 300 kV (see Fig. A.17) acceleration voltage suggest common cross-overs of both incoming waves. Especially in the latter case a twofold astigmatism (beams are elongated in similar directions at defocus; direction changes when switching between under- and overfocus) can be observed. Whether this astigmatism is due to a misalignment of the stigmator or due to charging — as encountered for thin phase plates (see Fig. 7.5) — remains uncertain.

Parallel to this work Matthias Lohr[81] has performed a measurement of the spot diameter

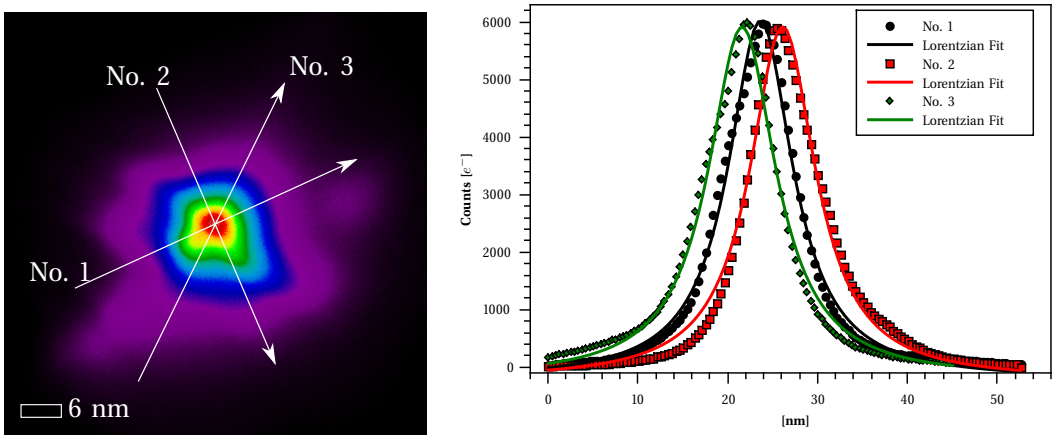

Figure 7.16.: TEM image of focused spot caused by twin aperture and line scans. Location and direction of line scans are indicated by white arrows. Microscope settings: TEM µProbe, gun lens 5, spot size 5, high tension 200 kV, magnification 145 kx. For colorbar see Fig. 7.17.

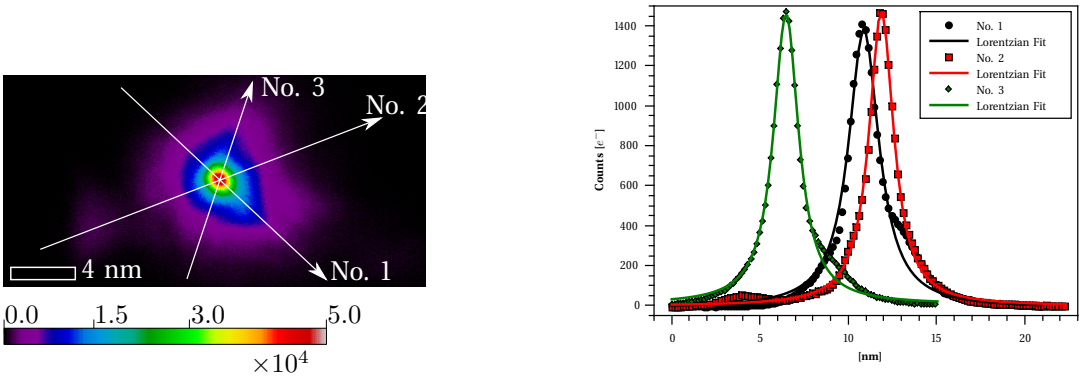

Figure 7.17.: Focused spot of twin aperture and line scans thereof. Microscope settings: TEM µProbe, gun lens 5, spot size 5, high tension 300 kV, magnification $8 \cdot 10^5$ x.

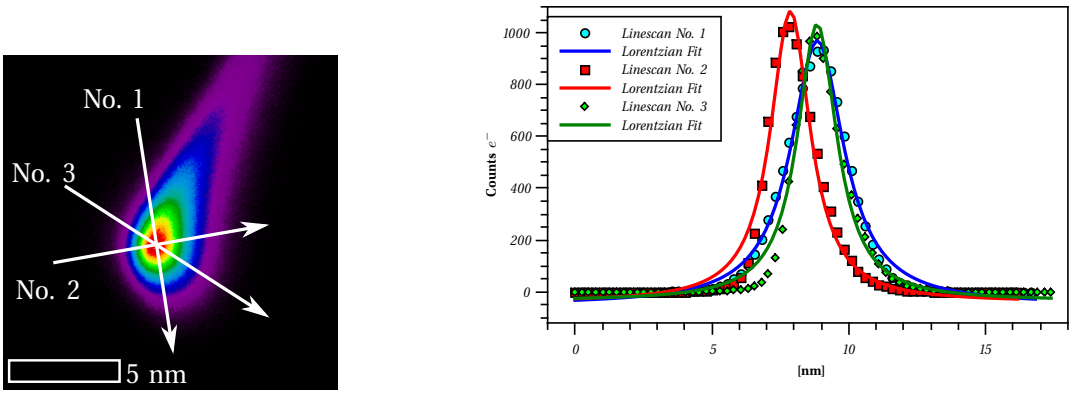

Figure 7.18.: Focused spot of 100 µm aperture and line scans thereof. Microscope settings: TEM µProbe, gun lens 5, spot size 5, high tension 300 kV, magnification 590 kx. For colorbar see Fig. 7.17.

for slightly different microscope settings[1]. By using the second method mentioned in the enumeration at the beginning of Sec. 7.4 he found a spot diameter of $\leq 3.9\,\mathrm{nm}$ by performing a DPC line scan across the edge of a piece of crystalline silicone.

The spot diameter of approximately $1.8\,\mathrm{nm}$ determined for the $100\,\mu\mathrm{m}$ aperture at $300\,\mathrm{kV}$ (see Table 7.2) does not agree very well with the result of Matthias Lohr. Despite the different microscope settings one would have expected to observe a dependence of the spot diameter on the *spot size* microscope setting, which controls the C1 lens. A stronger C1 excitation (higher spot size value) causes a stronger divergence of the beam and thus a smaller curvature of the spherical wave in the C2 aperture plane. This increases the resemblance of the wave function in the aperture plane to a plane wave. Accordingly one would expect to observe smaller spot diameters for larger spot size values for identical aperture diameters. As pointed out previously this deviation might be caused by electrostatic charging in the twin aperture device.

Finally we can compare the shape of the cross-over to the theoretical prediction from Sec. 5.2. According to the prediction for an incident coherent plane wave we would expect to observe an Airy disk superposed with interference fringes. Direct observation of the cross-over does not reveal such a structure.

As we are trying to image an interference pattern in a focused spot one can find many possible explanations why this did not succeed. For one the exposure time of the CCD camera was equal to $1\,\mathrm{ms}$, which gives rise to a considerable tail of the spot due to the frequent blanking and unblanking of the beam. As pointed out in Ref. [62] the FIB milling process can deposit material at unfavorable positions — e.g. metal ions on an area of insulator — and thus increase chances of high frequency charging/discharging cycles. Further reasons might include instabilities of the microscope due to environmental conditions.

To set the findings of this section into proportion the next section will investigate contamination spots grown with a focused electron probe.

7.4.2. Acquisition of Contamination Spots

In the previous section we have evaluated images of focused spots to determine the spot diameter of an electron probe. As the image of the cross-over in the previous technique is projected from the sample plane to the plane of the CCD camera the shape and size of the image of the cross-over can be modified using stigmator settings (Objective and Diffraction). In order to set the quantities obtained in Sec. 7.4.1 into proportion we choose a second technique to estimate the spot diameter. We are using the focused electron probe to grow contamination spots[42] on commercial Si_3N_4 membranes.

7.4.2.1. Focused Electron Beam Induced Deposition & Etching

Contaminations grow on electron-irradiated areas of the specimen by cross-linking of adsorbed hydrocarbon molecules on the specimen surface. In competition with this contamination, reactions with activated, adsorbed H_2O, O_2 or N_2 molecules cause etching of material. Depending on environmental properties — e.g. specimen preparation, partial pressures, specimen tempera-

[1] 300 kV, nProbe, gun lens 3, spot size 9 and 100 µm C2 aperture.

ture, and irradiation conditions — either process may prevail; equilibrium (zero growth/etching) is virtually impossible[42,160].

A technique intended to exploit the mechanisms of contamination growth in order to grow metallic and/or magnetic structures is called (focused) electron beam induced deposition ((F)EBID)[161–163] and uses a so called precursor gas, which is split by the electron probe such that — in theory — the metallic parts are deposited onto the specimen and the remaining gaseous parts are diffusing away from the sample. E.g. for the deposition of Fe diiron nonacarbonyl ($Fe_2(CO)_9$) is used as precursor[154]. Using this technique structure sizes $\leq 3\,\text{nm}$ can be achieved[164]. But without a proper setup — one can imagine — the resulting depositions can contain tremendous contaminations[154,165].

Alternatively the technique embodying electron beam exposure in order to etch material is called (focused) electron beam induced etching ((F)EBIE)[166–168]. To enhance the etching rate different precursor gases are used, e.g. XeF_2 for etching of SiO_2[167] or GaAs; in the latter case a resolution of 30 nm has been reported[169].

Fortunately we do not need pure depositions or high etching/growing rates; in order to determine the spot diameter of the electron probe we only need sufficient contrast between the membrane and grown contaminations or etched holes. To achieve this we want to increase the contamination growth process to avoid broadening of the contamination spot/needle due to multiple scattering[42,170]. To accelerate the contamination growth a PMMA resist was spin coated onto the membrane and baked out according to typical recipes for EBL processes. As proposed by Hoole[171] elongated exposure of the PMMA to electron irradiation allows usage of PMMA as negative resist.

The idea is to manually expose a spot pattern and investigate the residual PMMA after development. But if done in a TEM with a 200 – 300 keV electron probe, it is difficult to find and distinguish any spots grown due to irradiation from regular residuals on the membrane after development in acetone (see Fig. 7.19). Fig. 7.19 shows PMMA residues on a SiN membrane after development in acetone and cleansing with propanol. In the center one can see an ellipsoidal feature caused by irradiation with a focused ion beam (Exposure settings: 16 nA, 3 s). Virtually everywhere on the membrane one can find annular features which appear to be some 10 nm up to 500 nm in diameter. These residual PMMA disks cover the entire surface of the membrane. Due to their diameters down to the interesting regime differentiation between these disks and actual spots due to exposure is virtually impossible. Therefore we will use a slight modification to allow observation of a spot immediately after its growth. Here the electron ronchigram (see Sec. 6.1.5), which is commonly used for STEM alignments, is very useful.

7.4.2.2. Shadow Image

The specimen is prepared — like in the previous case — by spin-coating and baking out PMMA. Before exposing the PMMA it is removed using acetone and propanol. It is known from previous works[172] that some residues of PMMA will remain on the membrane. These residues are almost invisible in TEM images but — more conveniently — serve as seeds for increased growth of contamination spots.

By focusing the shadow image (see Sec. 6.1.5) one can grow noticeable contamination spots on SiN membranes while using identical microscope settings as in Sec. 7.4.1 with 300 kV elec-

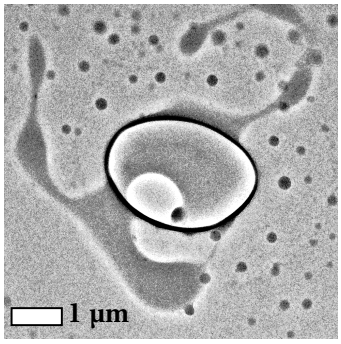

Figure 7.19.: TEM image of SiN membrane. The large ellipsoidal feature in the center was created by exposing a focused ion beam (16 nA, 3 sec) to the membrane. The smaller annular features in the image are residuals of PMMA that did not get washed off during development in acetone. These PMMA disks have diameters down to the order of the spot diameter.

trons within 20 seconds. Unfortunately we were not able to grow contaminations with 200 kV acceleration voltage[m].

7.4.2.3. Analysis

As described in the previous subsection the C2 lens excitation is adjusted such that the magnification in the shadow image becomes maximal. After the exposure time the intensity is spread to illuminate a larger area. Being at overfocus the sample is brought close to focus in order to reduce fringes due to defocus and eliminate the additional magnification due to projection of the shadow image. The grown spot or etched hole can be observed with sufficient contrast when the specimen is not in Gaussian focus, but in the so called *Scherzer defocus*, which aims to optimize the contrast transfer by counteracting spherical aberration effects by defocus. As the investigated contaminations and holes are quite small or offer very little contrast an even higher defocus than the Scherzer defocus is needed occasionally.

Fig. 7.20 shows the results for different apertures after an exposure time of 20 s. Fig. 7.20a shows a defocused image of holes etched into the SiN membrane by use of a standard 100 µm aperture with the same microscope settings as in Sec. 7.4.1 (compare caption of Fig. 7.20). The defocus is required to achieve a decent contrast in the image. The holes have a diameter of approximately 3.2 nm, which is close to the limit of ≤ 3 nm reported for (F)EBID in Ref. [164].

The spot diameters determined in the previous section are of the same order of magnitude as the hole diameters. The deviation between the previously determined spots' FWHM and the hole diameter is a factor of ≈ 1.8. The broadening of the hole can have multiple causes, e.g. wobbling of the beam[n], mechanical drift of the stage or that etching was not limited to the area defined by the FWHM. As we have seen in Sec. 7.4.1 a Lorentzian is a good approximation to the intensity distribution of a focused beam. Assuming a Lorentzian shaped beam with FWHM of 1.8 nm as determined in the previous section etching has been performed in an area, where the intensity is higher than $\approx 1/4$ of the maximum's value. Given a rather large defocus distance in the acquisition of Fig. 7.20a the obtained numbers appear plausible assuming the hole diameter has been overestimated.

Taking a look at the depositions grown using the twin aperture (Figs. 7.20b and 7.20c) matters look worse than during the acquisition of focused spots using the CCD camera. Three of four

[m] Exposure times of up to 20 mins were tested.
[n] A problem that was amplified by the custom aperture holder.

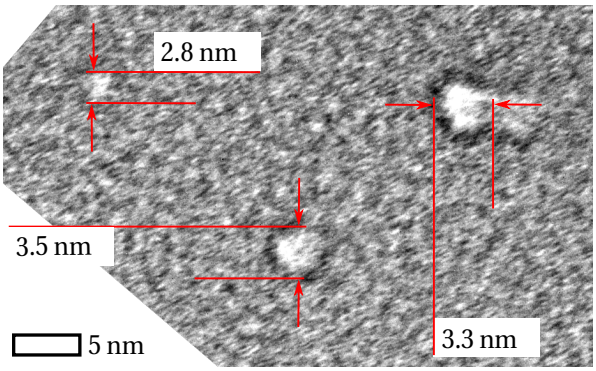

(a) TEM image of holes etched with focused electron beam. C2 aperture: ⌀ 100 µm.

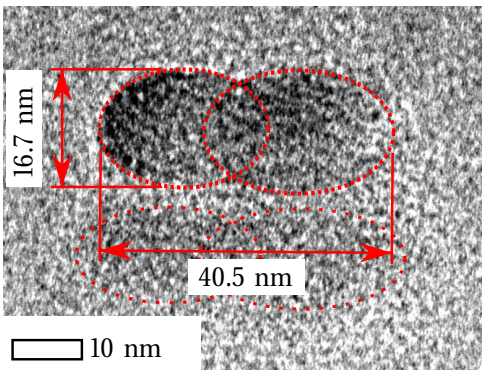

(b) TEM image of contamination grown by exposure to a "focused" beam. C2 aperture: Twin aperture.

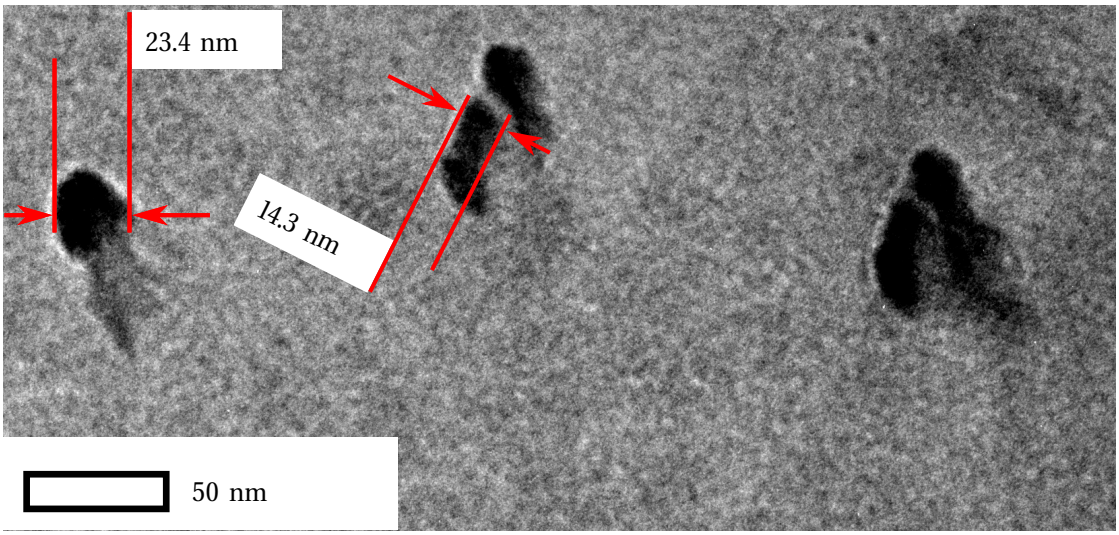

(c) TEM image of contaminations grown by a "focused" beam. C2 aperture: Twin aperture.

Figure 7.20.: TEM images of holes and contamination spots created on the SiN membrane. Holes were etched using a standard C2 aperture (⌀ 100 µm). Contaminations were grown using the twin aperture. Microscope settings: 300 kV, gun 5, spot 5, exposure time 20 s.

shown contamination patterns indicate that the beams originating from the two aperture holes do not converge into a common cross-over point or the cross-over point resides not within the sample plane. This could be explained by various hypotheses, e.g.

1. The shadow image is not in focus; this can happen rather easily due to the combination of the SiN membrane not providing much contrast and the not well-defined edges of the aperture holes.
2. The exposure time was too long allowing lateral growth[42,154,170] due to sample/beam drift.
3. Charging and scattering effects can produce more complex intensity distributions, which were due to the high intensity of the "main peak" not visible in CCD images.

Fig. 7.20c gives an overview of three nearby contamination patterns grown by exposure to the cross-over of the twin aperture. Except for the left pattern no common cross-over was achieved, whereas the left pattern has a diameter of 23.4 nm. As one can see the dark dot has a lighter tail pointing to the lower right. As this tail is rather edgy it is presumably caused by a combination of charging effects and the poorly defined aperture hole edges.

The other patterns in Fig. 7.20c have a smallest diameter of 14.3 nm and can be explained by reference to the focal series in Fig. A.17. The focal series shows at under- and overfocus strong aberrations that elongate the beams originating from the aperture plane almost in a parallel manner. Contrary thereto the angle between the elongations in the remaining patterns in Fig. 7.20c appears to be larger. This deviation might be caused by degeneration of the twin aperture over time[o] or by the fact that the cross-over images of the focal series were improved by stigmator settings.

Fig. 7.20b shows a single contamination pattern (16.7 nm $\times$ 40.5 nm) generated with a twin aperture. As indicated by the red dashed ellipsoids the specimen and/or beam has drifted during exposure. Due to the lack of contrast and the presence of distortions focusing the shadow image is almost impossible.

As we were able to achieve cross-overs of similar sizes as in Sec. 7.4.1 for a standard aperture it would be improbable that a different measurement technique would suggest a spot diameter of an order of magnitude larger for the twin aperture unless serious charging effects had degraded the twin aperture's circuitry.

In conclusion we can say that we were able to produce spot/hole diameters of the same order of magnitude for the 100 µm aperture as with the previous method. Unfortunately we were unable to verify this behavior for the twin aperture as it probably took serious damage due to elongated exposure to the electron beam. Before the removal from the aperture holder the electron beam was very unstable (strong in-plane vibration) even when a standard C2 aperture was inserted into the beam.

7.5. Summary

In this chapter we have experimentally determined the convergence semi-angle, which allowed to perform electron optical simulation of the cross-over that is to be expected for a twin aperture

[o] focal series was acquired prior to contamination pattern

under realistic conditions of a Tecnai F30 series microscope.

Furthermore we have characterized the problems arising from electrostatic charging in thin phase plates and thick electroplated gold layers.

Using thick platinum substrates we have conducted different measurements to determine the achievable spot diameter for a twin aperture and compared it to results obtained for a default C2 aperture. Despite different problems we have shown that a spot diameter (FWHM) of the order of a couple of nanometers is possible for 200–300 keV electrons.

Verification of these numbers with a second technique was not successful.

8. Conclusion

In this work we have proposed a new setup for measuring EMCD experiments, which does — in theory — not rely on a crystalline sample for providing the required phase shifted beams.

FEM calculations of the electrostatic potentials caused by phase plates justify the commonly assumed constant phase shift approximation inside a ring electrode for *small* radii, which are an order of magnitude larger than their thickness; if the radius is increased by another order of magnitude the phase shift has to be described by a hyperbolic cosine. On the other hand we have shown that the phase shift outside of the ring electrode in general cannot be neglected.

Based on these insights we have investigated the intensity distribution and phase difference in the sample plane caused by a twin aperture. Thereby we have demonstrated the effects of different phase shifting models and aberrations. From these we have concluded that aberrations can be neglected for the particular microscope and that the effects of most investigated non-constant phase shift models are still in reasonable agreement with the analytical model as the strongest effects due do non-constant phase shifts appear to be a shift of the *non-phase-shifted* beam in the sample plane and a "blurring" of the *phase shifted* beam.

Calculations of the expected magnetic signal by Jan Rusz suggest a strong dichroic signal due to interference of the two incident waves assuming plane waves instead of convergent ones.

In experiments we have seen that for the construction of phase plates in the condenser system thick layers of Pt are needed and that a common cross over of two incident waves originating from the twin aperture is possible. An interference pattern in this cross over was not observable — mainly due to technical issues.

The proposed setup uses convergent waves with a phase difference that is not determined by the crystal structure as in the intrinsic EMCD method, but by the microscope and twin aperture geometry. Thus the phase plate geometry (aperture radius and displacement) would need to be optimized for a specific microscope and the lattice constant of the primary investigated material.

Even if the competing setup for vortex beams is more in the focus of the EMCD community, the twin aperture setup might still be of interest. As vortex beams are due to their donut shape larger in diameter than the crossover of the twin aperture the twin aperture might be the technique to allow high resolution, magnetic imaging on a sub-nm range.

Currently Jan Rusz is working on adaptations of his code to simulate the diffraction pattern and magnetic signal for two incident converging beams of the shape presented in Sec. 5.2. Furthermore he intends to perform these calculation for different incidence angles — ranging from optimal to worst case scenario. Preliminary results look are very promising as they appear to verify the results found for plane waves.

On the other hand the group of Peter Schattschneider is investigating the possibility of combining a twin aperture and condenser stigmator to create vortex beams (unpublished, yet).

A. Appendix

A.1. Aperture Holder Schematics

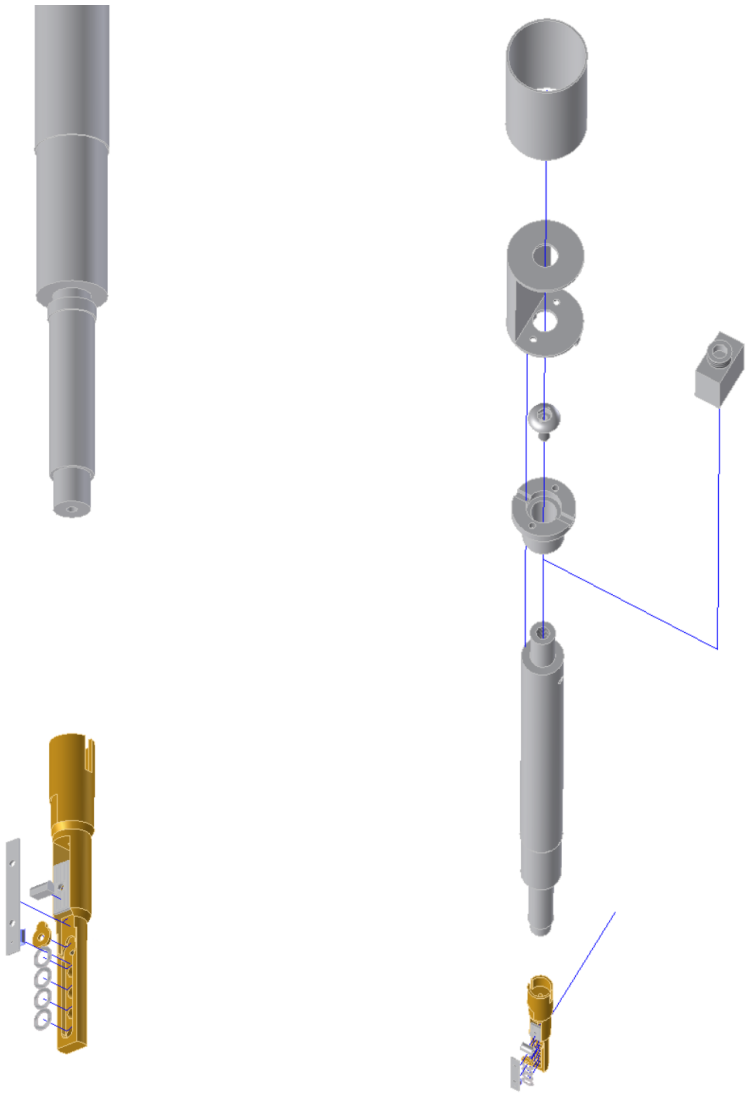

Figure A.1.: Explosion diagrams of customized aperture holder.

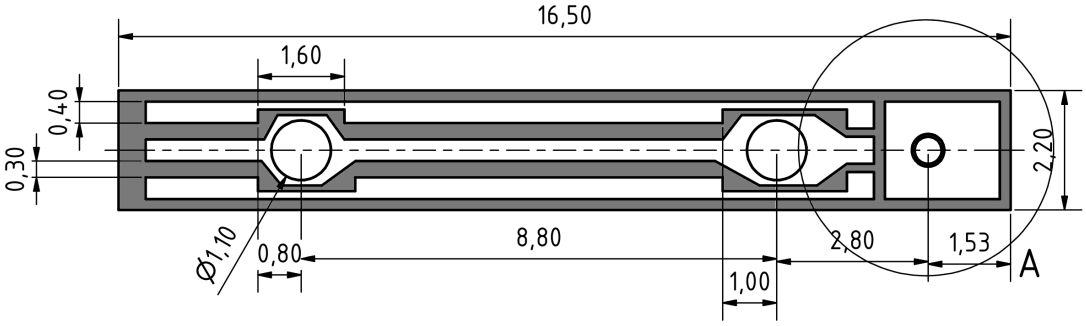

(a) PCB 2

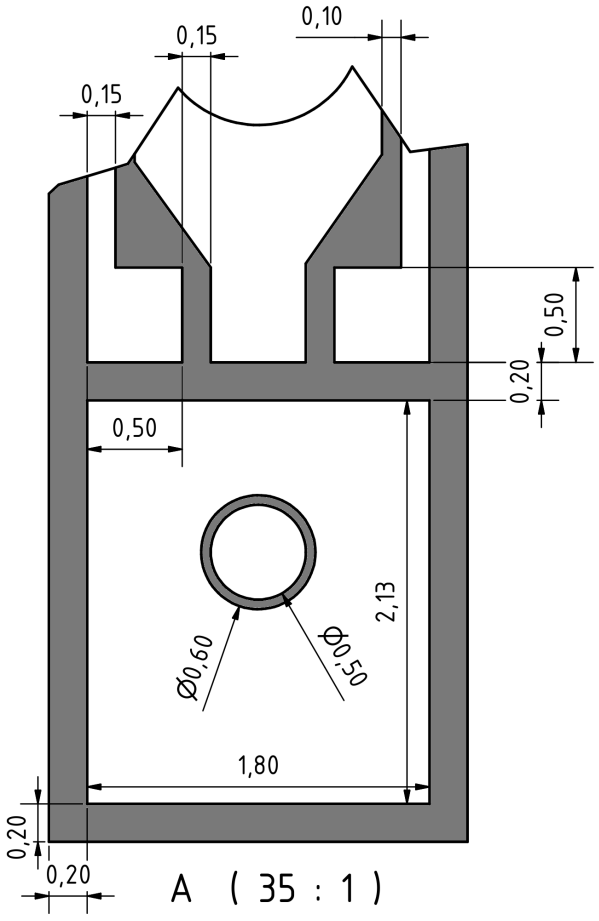

(b) PCB 2 – Close Up

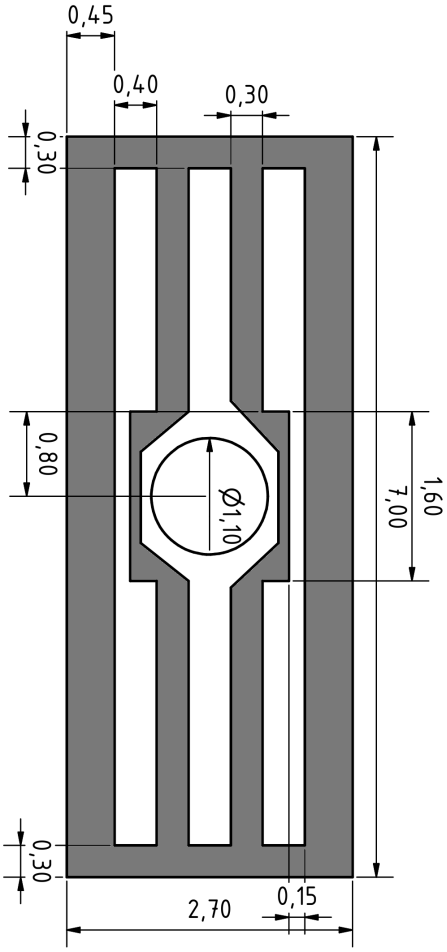

(c) PCB 1

Figure A.2.: Printed Circuit Boards (PCBs) for use in the customized holder as described in Sec. 6.3.

A.2. Software

For this work a series of Python scripts have been used for calculations and/or evaluations. The majority thereof can be found in the *Bazaar* repository https://em.ur.de/code/ after registration at https://em.ur.de/users/register/.

Another tool — initially intended for evaluation and treatment of EMCD spectra[173] — has been adapted to treat DPC data. This tool has been published on https://launchpad.net/emcd.

A.3. FEM Results

Table A.1.: Fit parameters α, β and γ for all variations of the twin aperture. The designs `twin_ap_2D_X5_i`, $i \in [2, 3, 4, 5]$, are identical to `twin_ap_2D_X5`, but has more free area above and below the phase plate. This free space along the z axis is called δz.

Design	**Area**	**Parameters** α, β, γ	z **range** [μm]
`boersch_pp`	A	$\alpha(U) \approx 7.7\ U$ $\beta(U) \approx 0.53\ \sqrt{U}$	$[-10,\ 11]$, $\delta z = 10$
	B	$\alpha(U) \approx -2.74 \cdot 10^{-1}\ U$ $\beta(U) \approx 3.38 \cdot 10^{2}\ U$ $\gamma \approx -8.86\,\mu\mathrm{m}$	
`twin_ap_2D_X1`	A	$\alpha(U) \approx 4.70 \cdot 10^{-2}\ U + 1.78 \cdot 10^{-2}\ U^2$ $\beta(U) \approx 5.74 \cdot 10^{-2}\ \mathrm{acosh}(U+1)$	$[-10,\ 11]$, $\delta z = 10$
	B	$\alpha(U) \approx -6.95 \cdot 10^{-3}\ U$ $\beta(U) \approx 1.46 \cdot 10^{1}\ U$ $\gamma \approx 0.53\,\mu\mathrm{m}$	
`twin_ap_2D_X2`	A	$\alpha(U) \approx 9.07 \cdot 10^{-2}\ U$ $\beta(U) \approx 2.07 \cdot 10^{-2}\ \mathrm{acosh}(U+1)$	$[-15,\ 35]$, $\delta z = 10$
	B	$\alpha(U) \approx -4.96 \cdot 10^{-4}\ U$ $\beta(U) \approx 3.01\ U$ $\gamma \approx 9.25\,\mu\mathrm{m}$	
`twin_ap_2D_X3`	A	$\alpha(U) \approx 1.51\ U$ $\beta(U) \approx 5.31 \cdot 10^{-2}\ \mathrm{acosh}(U+1)$	
	B	$\alpha(U) \approx -1.44 \cdot 10^{-2}\ U$ $\beta(U) \approx 8.56 \cdot 10^{1}\ U$ $\gamma \approx 13.17\,\mu\mathrm{m}$	
`twin_ap_2D_X4`	A	$\alpha(U) \approx 8.22\ U$ $\beta(U) \approx 3.61 \cdot 10^{-2}\ \mathrm{acosh}(U+1)$	
	B	$\alpha(U) \approx -2.50\ U$ $\beta(U) \approx 1.28 \cdot 10^{5}\ U$ $\gamma \approx 141.32\,\mu\mathrm{m}$	

Table A.1.: Fit parameters α, β and γ for all variations of the twin aperture. (Continued)

Design	**Area**	**Parameters** α, β, γ	z **range** [μm]
`twin_ap_2D_X5`	A	$\alpha(U) \approx 2.24\ U$ $\beta(U) \approx 5.58 \cdot 10^{-2}\ \mathrm{acosh}(U+1)$	$[-15, 35]$, $\delta z = 10$
	B	$\alpha(U) \approx -1.93 \cdot 10^{-2}\ U$ $\beta(U) \approx 97.9\ U$ $\gamma \approx 9.87\,\mu\mathrm{m}$	
`twin_ap_2D_X5_2`	A	$\alpha(U) \approx 4.53\ U$ $\beta(U) \approx 4.58 \cdot 10^{-2}\ \mathrm{acosh}(U+1)$	$[-30, 55]$, $\delta z = 30$
	B	$\alpha(U) \approx -2.49 \cdot 10^{-1}\ U$ $\beta(U) \approx 2.94 \cdot 10^{3}\ U$ $\gamma \approx 41.45\,\mu\mathrm{m}$	
`twin_ap_2D_X5_3`	A	$\alpha(U) \approx 6.77\ U$ $\beta(U) \approx 3.93 \cdot 10^{-2}\ \mathrm{acosh}(U+1)$	$[-50, 75]$, $\delta z = 50$
	B	$\alpha(U) \approx -1.15\ U$ $\beta(U) \approx 3.09 \cdot 10^{4}\ U + 1$ $\gamma \approx 90.4\,\mu\mathrm{m}$	
`twin_ap_2D_X5_4`	A	$\alpha(U) \approx 8.22\ U$ $\beta(U) \approx 3.61 \cdot 10^{-2}\ \mathrm{acosh}(U+1)$	$[-70, 95]$, $\delta z = 70$
	B	$\alpha(U) \approx -2.5\ U$ $\beta(U) \approx -1.3 \cdot 10^{5}\ U$ $\gamma \approx 141,32\,\mu\mathrm{m}$	
`twin_ap_2D_X5_5`	A	$\alpha(U) \approx 1.08 \cdot 10^{1}\ U$ $\beta(U) \approx 3.39 \cdot 10^{-2}\ \mathrm{acosh}(U+1)$	$[-90, 115]$, $\delta z = 90$
	B	$\alpha(U) \approx -4.11\ U$ $\beta(U) \approx 3.28 \cdot 10^{5}\ U$ $\gamma \approx 182.77\,\mu\mathrm{m}$	

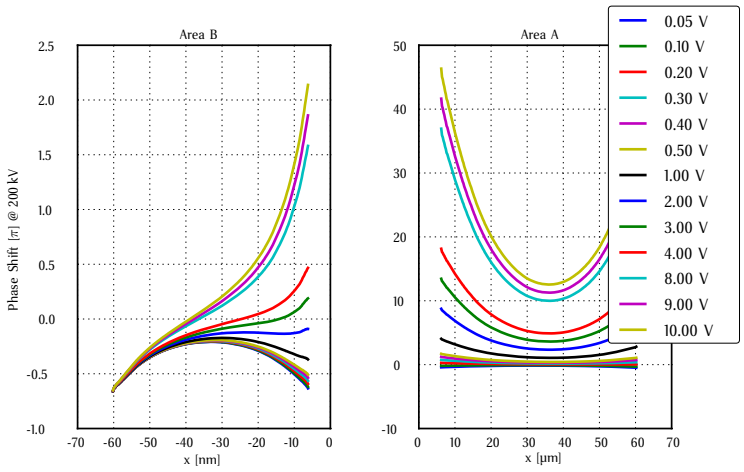

Figure A.3.: Cross section along x axis showing phase shift for 200 keV electrons for different applied potentials. See Sec. 4.3.4.3.

A.4. Electron Optical Numerical Calculations

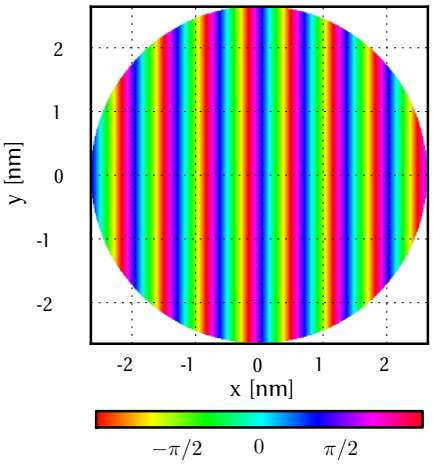

(a) Analytical model, aberration-free

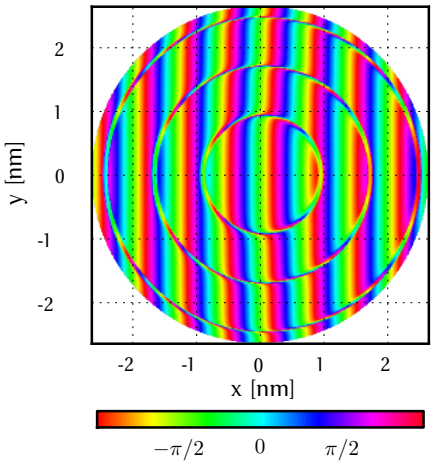

(b) Hyperbolic cosine model, aberration-free

Figure A.4.: Phase difference $\Delta\phi$ between the two incident waves for the analytical (see Sec. 5.2.1) and numerical hyperbolic cosine (see Sec. 5.2.2) models in 2D. Line scans along these images are shown in Figs. 5.5 and 5.10, respectively.

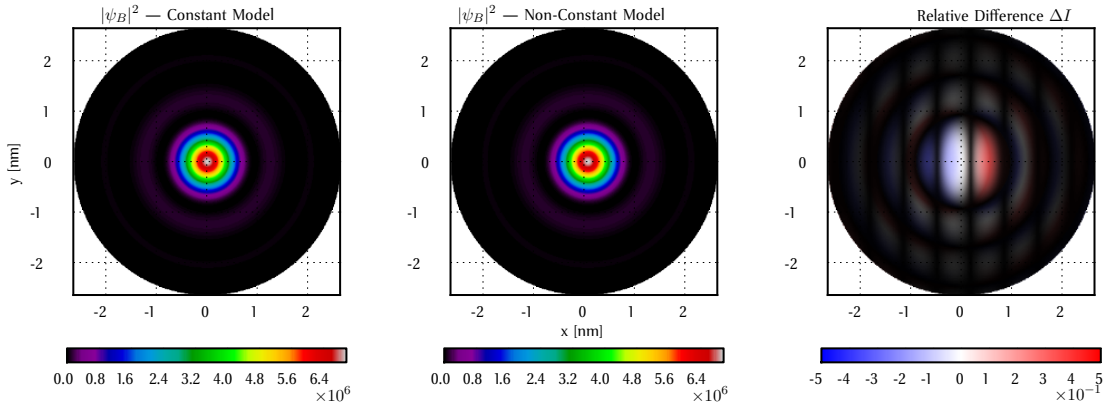

Figure A.5.: Comparison between the intensity distributions of the beams originating from *Area B* for the analytical (see Sec. 5.2.1) and numerical model (see Secs. 5.2.2.1 and 4.3.3). The filter is scaled with a square root function, while the colorbar has been limited to the range [-50%, 50%]. Compare to Fig. 5.8, which shows the comparison for the entire wave function.

In Sec. 5.2.2 we have presented numerical calculations based on the model `twin_ap_2D_X5_5`, which regards the most free space above and below the twin aperture and thus represents a best case scenario. Neglecting the model `twin_ap_2D_X1` based on the thin twin aperture one can e.g. refer to model `twin_ap_2D_X5`, which is identical to `twin_ap_2D_X5_5` except that it regards less free space, as a worst case scenario.

The following figures show similar plots as the figures in Sec. 5.2.2, except that they are based on the model `twin_ap_2D_X5`.

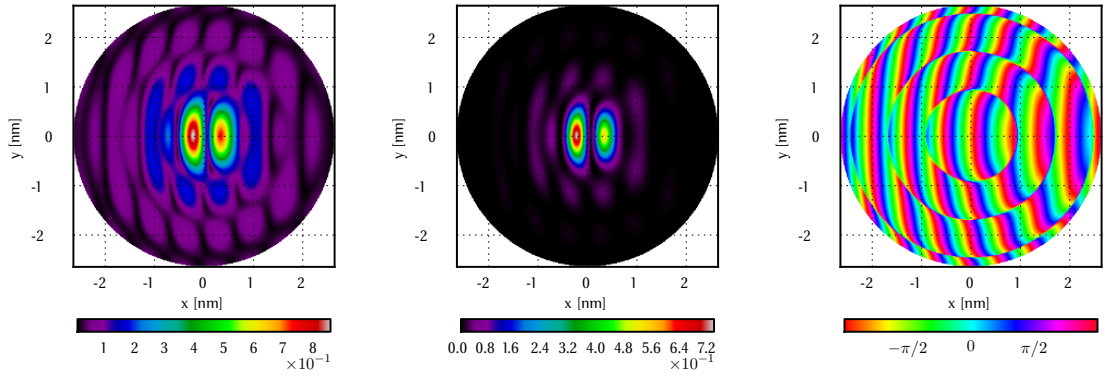

(a) Amplitude (b) Intensity (c) Phase Difference

Figure A.6.: Amplitude, Intensity and Phase Difference for two incident convergent beams by twin aperture calculated with model `twin_ap_2D_X5` in absence of aberrations. For details refer to Sec. 5.2.2.1.

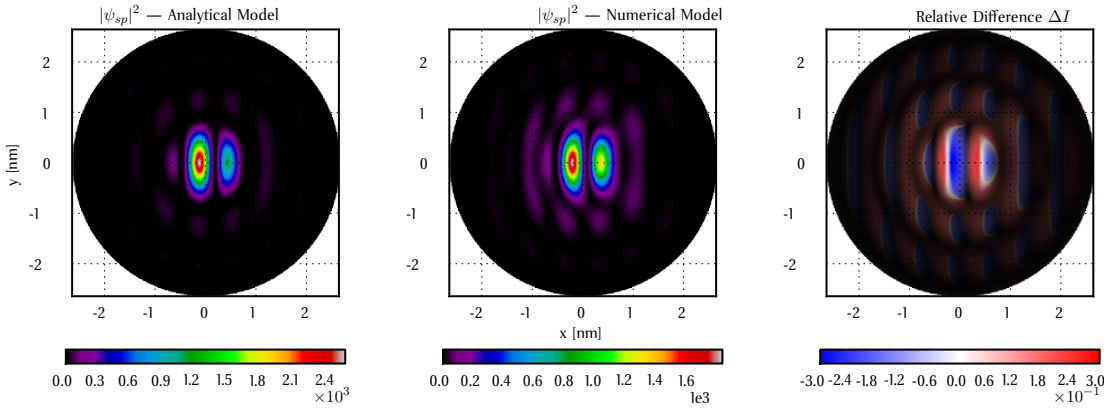

Figure A.7.: Calculated intensities for constant phase shift model and model `twin_ap_2D_X5`. The difference image (right) has been overlaid with a black alpha filter, which was scaled by a square root.

(a) Phase Front, ψ_B.

(b) Phase Front, ψ_A.

Figure A.8.: Phase fronts of the waves ψ_A and ψ_B with phase shifts $\varphi_{U,i}$ according to model `twin_ap_2D_X5`.

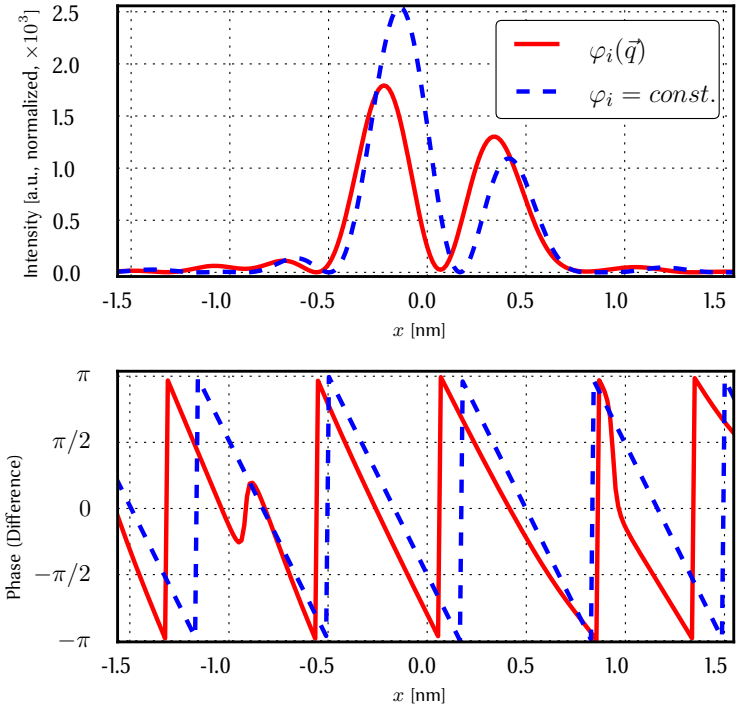

Figure A.9.: Line scans along the $y = 0$ axis of the intensity distributions of Fig. A.7 (**Upper** box) and phase difference (**Lower** box) between the incident beams for both cases.

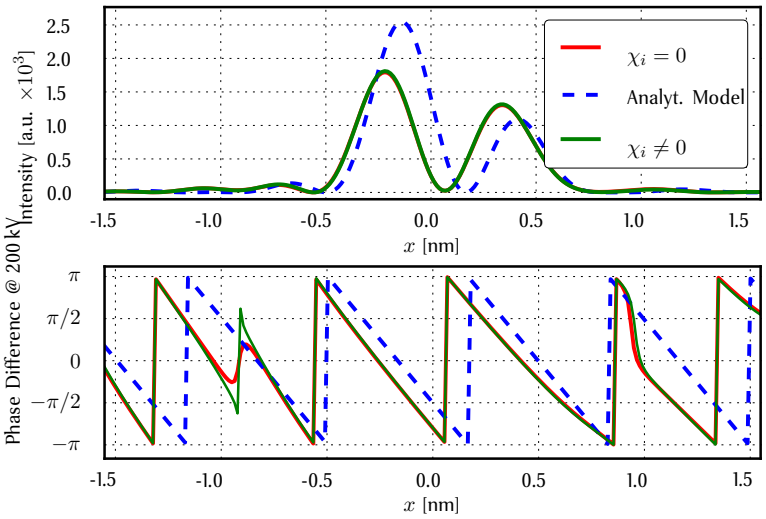

Figure A.10.: Line scans along the $y = 0$ axis of the intensity distributions of three different cases: Aberration-free hyperbolic phase shift, constant phase shift and aberration-afflicted hyperbolic phase shift (**Upper** box) and phase difference (**Lower** box) between the incident beams for all cases.

A.5. Dynamical Diffraction Simulations by J. Rusz

The simulation presented in this section were performed by Jan Rusz and have been submitted to Ultramicroscopy[7] for publication. For explanations of the figures refer to Sec. 5.4.

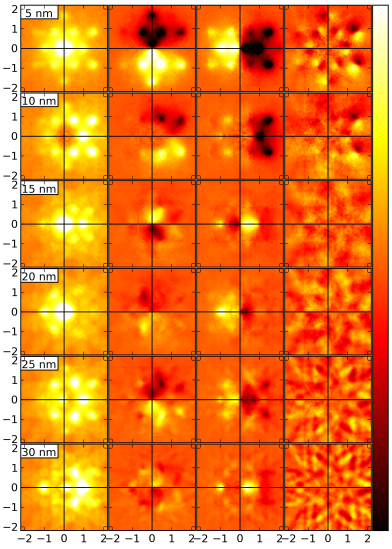

(a) *Direct term* contributions. Refer to Fig. 5.19a for more information.

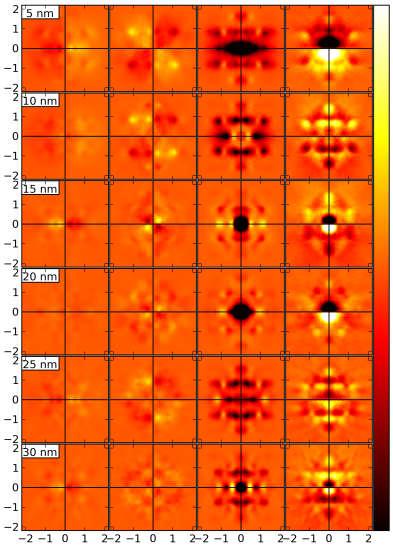

(b) *Interference term* contributions. Refer to Fig. 5.19b for more information.

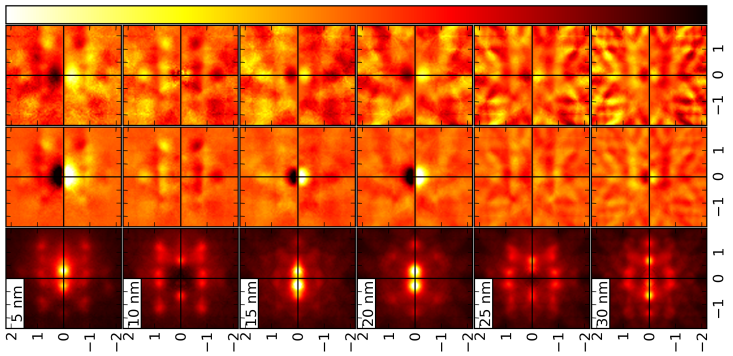

(c) Sum of direct and interference terms. Pleaser refer to Fig. 5.19d for more information.

Figure A.11.: (Non-)Mangetic signal for different thicknesses. Pleaser refer to Fig. 5.19. for more information.

A.6. DPC Measurements

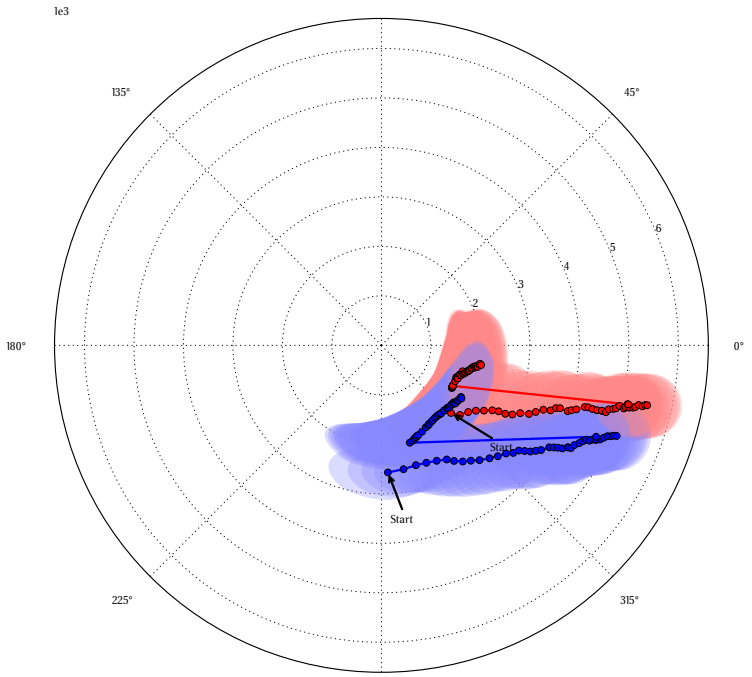

Figure A.12.: Time dependent mean beam deflection for beams passing through both holes of the twin aperture. Standard deviation has been used as a basis for the generation of error ellipsoids. A plot of only the radial component is shown in Fig. 7.6. For details see Sec. 7.2.1.

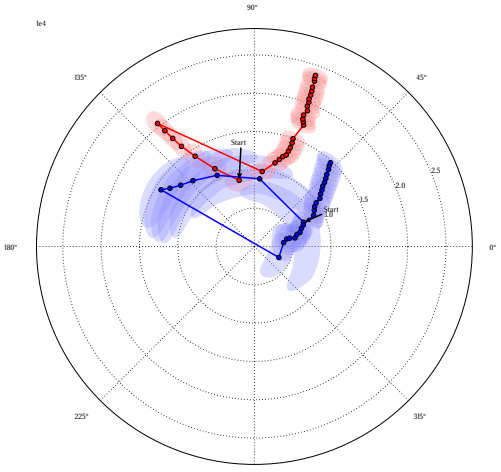

(a) Thin twin aperture.

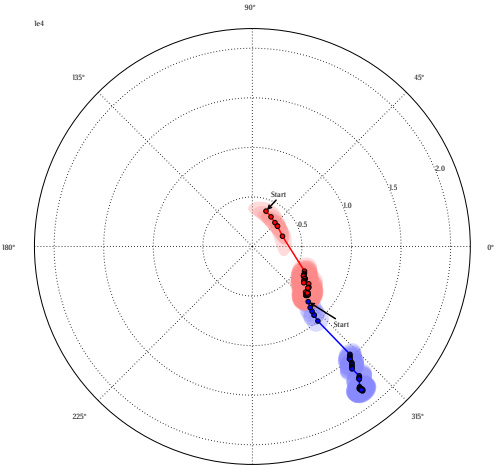

(b) Pt-foil based twin aperture.

Figure A.13.: Two further examples of DPC time series.

A.7. EDX Mappings

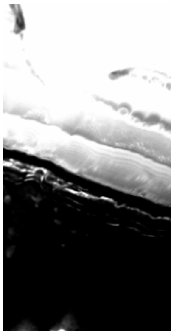

(a) Bright Field image

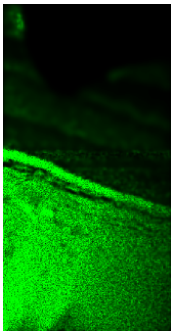

(b) Au map

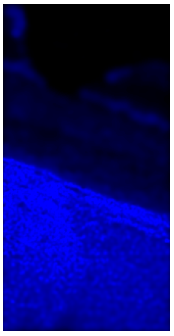

(c) Co map

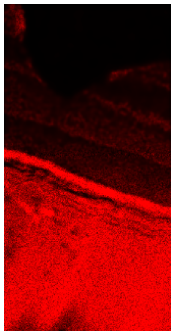

(d) Cu map

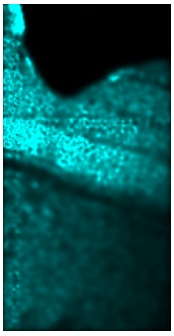

(e) Si map

Figure A.14.: EDX mappings without scale bar of **right** hand side TEM lamella in Fig. 7.11. For scale bar see Fig. 7.11.

(a) Bright Field image

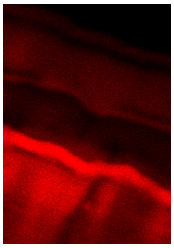

(b) Au map

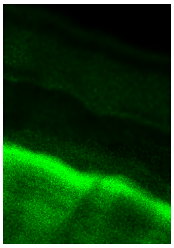

(c) Co map

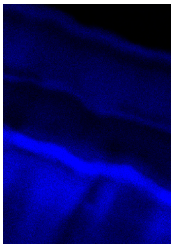

(d) Cu map

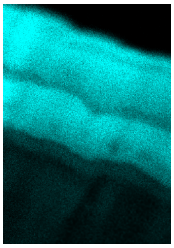

(e) Si map

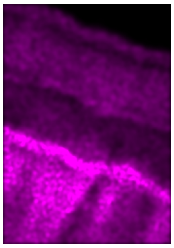

(f) N map

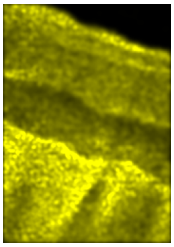

(g) O map

Figure A.15.: EDX mappings without scale bar of **left** hand side TEM lamella in Fig. 7.11. For scale bar see Fig. 7.11.

A.8. Focal Series

Line scan No.	A [nm]	x_0 [nm]	y_0	w [nm]
7.16, 1	$(8.58 \pm 0.05) \cdot 10^4$	23.64 ± 0.01	-219 ± 9	4.38 ± 0.03
7.16, 2	$(8.61 \pm 0.06) \cdot 10^4$	26.11 ± 0.02	-230 ± 10	4.46 ± 0.03
7.16, 3	$(8.80 \pm 0.06) \cdot 10^4$	21.60 ± 0.02	-200 ± 10	4.58 ± 0.03
A.18a, 1	$(6.52 \pm 0.08) \cdot 10^4$	11.53 ± 0.02	-70 ± 30	2.42 ± 0.03
A.18a, 2	$(7.11 \pm 0.02) \cdot 10^4$	21.94 ± 0.006	-136 ± 6	2.74 ± 0.01

Table A.2.: Fit parameters of line scans (Fig. A.18a and A.16f) for a 200 kV cross-over. See Sec. 7.4.1 for details.

Line scan No.	A [nm]	x_0 [nm]	y_0	w [nm]
A.20a, 1	$(9.9 \pm 0.1) \cdot 10^3$	12.6 ± 0.02	-69 ± 4	2.46 ± 0.03
A.20a, 2	$(9.7 \pm 0.1) \cdot 10^3$	14.68 ± 0.02	-52 ± 3	2.44 ± 0.03
A.20a, 3	$(9.4 \pm 0.1) \cdot 10^3$	13.28 ± 0.01	-67 ± 4	2.34 ± 0.03
A.20b, 4	$(1.49 \pm 0.01) \cdot 10^4$	10.789 ± 0.008	-125 ± 8	1.03 ± 0.01
A.20b, 5	$(1.56 \pm 0.01) \cdot 10^4$	13.722 ± 0.008	-121 ± 8	1.10 ± 0.01

Table A.3.: Fit parameters of line scans (Fig. A.20) for a 200 kV cross-over with standard 100 µm aperture. See Sec. 7.4.1 for details.

Line scan No.	A [nm]	x_0 [nm]	y_0	w [nm]
7.17, 1	$(4.60 \pm 0.03) \cdot 10^3$	$10.88 \pm 6 \cdot 10^{-3}$	-14 ± 2	1.05 ± 0.01
7.17, 2	$(3.92 \pm 0.01) \cdot 10^3$	$11.88 \pm 2 \cdot 10^{-3}$	-2.8 ± 0.7	0.842 ± 0.003
7.17, 3	$(3.96 \pm 0.02) \cdot 10^3$	$6.48 \pm 3 \cdot 10^{-3}$	6 ± 2	0.866 ± 0.006

Table A.4.: Fit parameters of line scans for a 300 kV cross-over. See Sec. 7.4.1 for details.

Line scan No.	A [nm]	x_0 [nm]	y_0	w [nm]
7.18, 1	$(1.99 \pm 0.02) \cdot 10^3$	$7.815 \pm 8 \cdot 10^{-3}$	-22 ± 2	0.76 ± 0.01
7.18, 2	$(2.37 \pm 0.03) \cdot 10^3$	$6.711 \pm 8 \cdot 10^{-3}$	-37 ± 2	0.95 ± 0.01
7.18, 3	$2.30 \pm 0.03) \cdot 10^3$	$7.551 \pm 1 \cdot 10^{-2}$	-28 ± 2	0.96 ± 0.02
EFTEM	$(2.74 \pm 0.03) \cdot 10^4$	$12.842 \pm 6 \cdot 10^{-3}$	-200 ± 20	0.629 ± 0.009

Table A.5.: Fit parameters of line scans (Fig. 7.18) of cross-over for 300 kV and standard 100 µm aperture. See Sec. 7.4.1 for details.

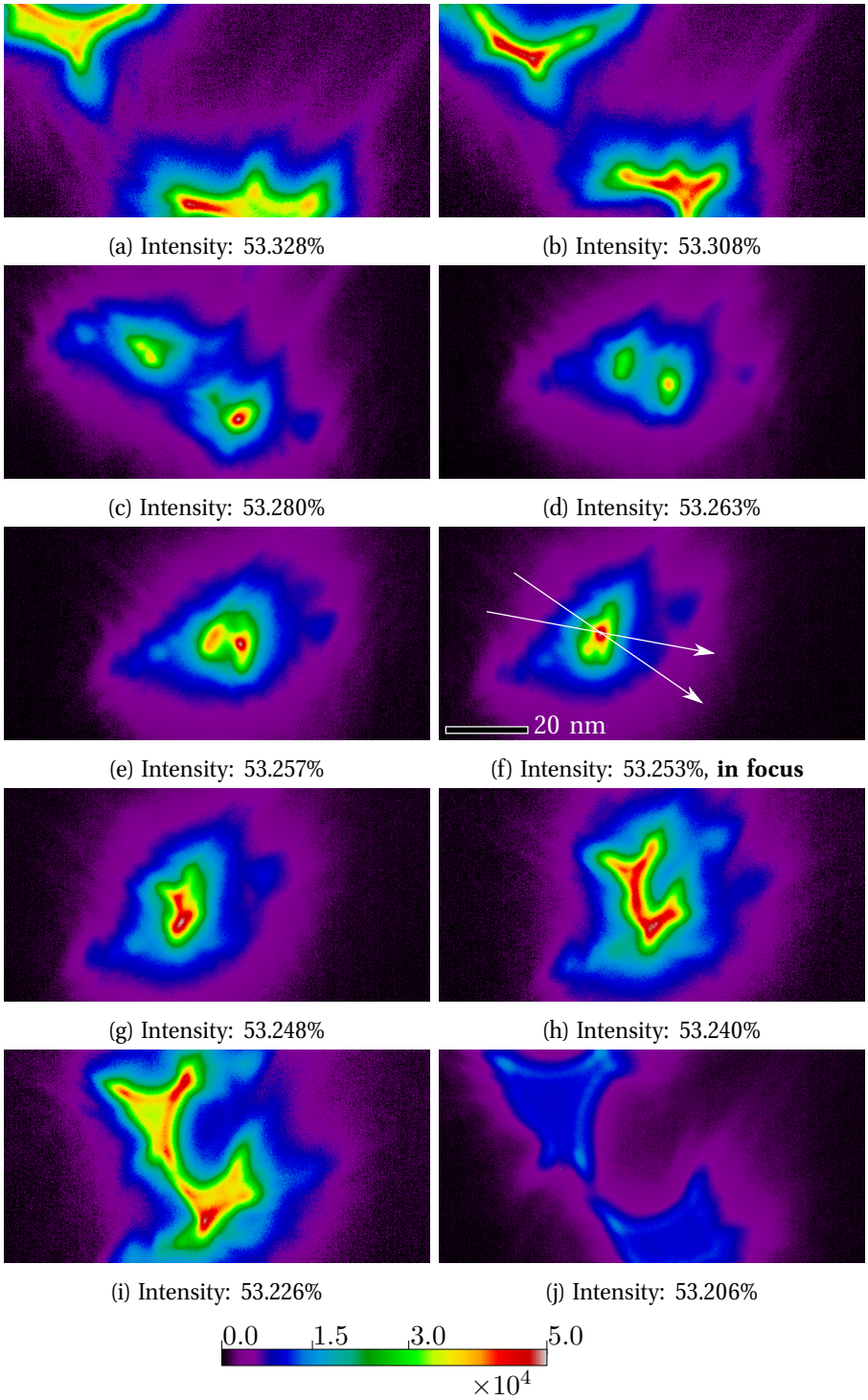

(a) Intensity: 53.328%
(b) Intensity: 53.308%
(c) Intensity: 53.280%
(d) Intensity: 53.263%
(e) Intensity: 53.257%
(f) Intensity: 53.253%, **in focus**
(g) Intensity: 53.248%
(h) Intensity: 53.240%
(i) Intensity: 53.226%
(j) Intensity: 53.206%

Figure A.16.: Focal series acquired with Gatan CCD camera. C2 lens excitation is called "Intensity" on FEI microscopes. HWHM: 6 ± 1 nm (see Sec. 7.4.1).Microscope settings: TEM µProbe, guns lens 5, spot size 5, high tension 200 kV, magnification 145 kx. All subfigures share the same scale bar shown in Fig. A.16f.

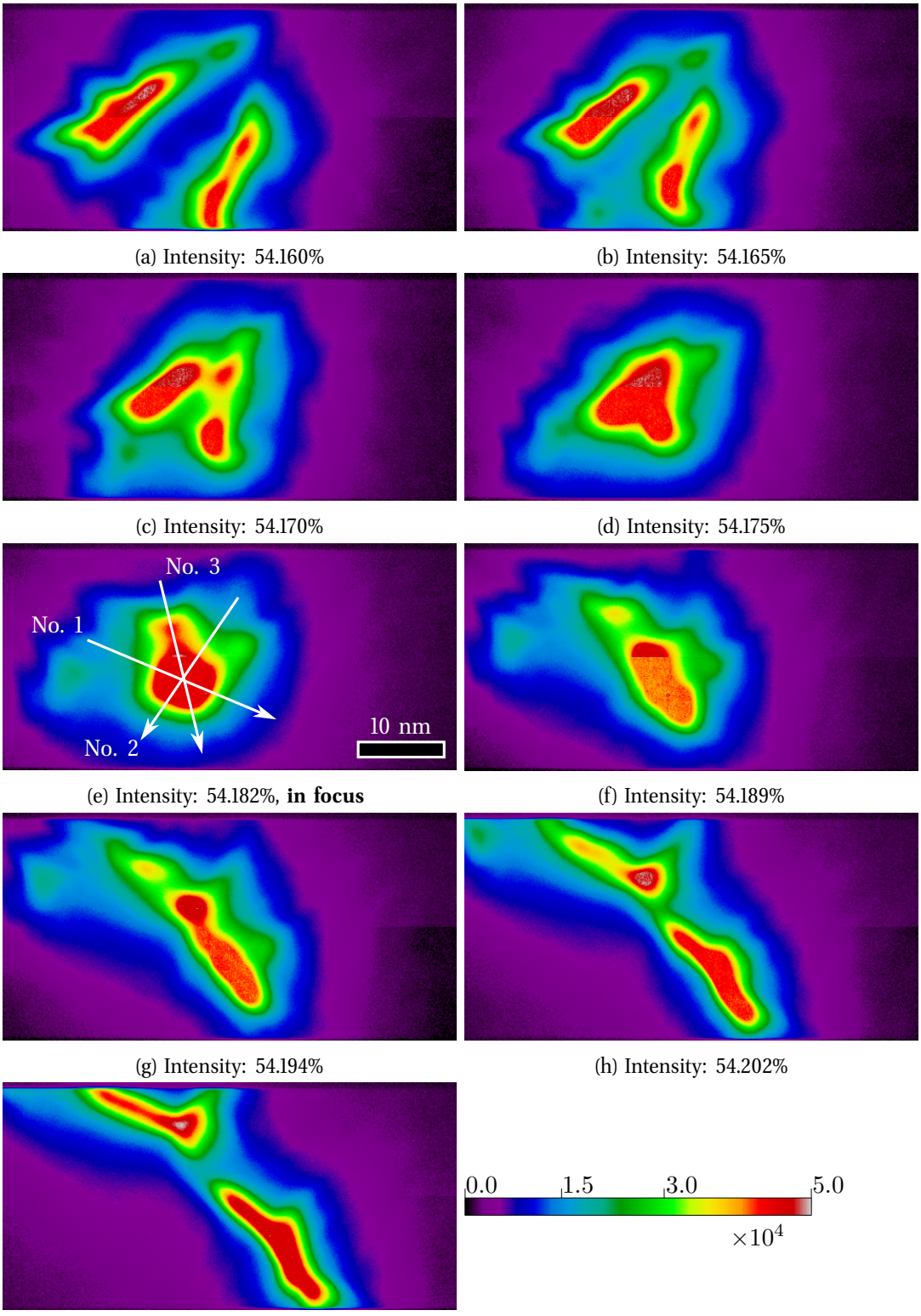

(a) Intensity: 54.160%

(b) Intensity: 54.165%

(c) Intensity: 54.170%

(d) Intensity: 54.175%

(e) Intensity: 54.182%, **in focus**

(f) Intensity: 54.189%

(g) Intensity: 54.194%

(h) Intensity: 54.202%

(i) Intensity: 54.208%

Figure A.17.: Focal series acquired with Gatan GIF Tridiem. C2 lens excitation is called "Intensity" on FEI microscopes. Spot diameter: $\leq 7.3 \pm 2\,\mathrm{nm}$. Microscope settings: EFTEM µProbe, guns lens 5, spot size 3, high tension 300 kV, magnification $8 \cdot 10^5$ x. All subfigures share the same scale bar shown in Fig. A.17e.

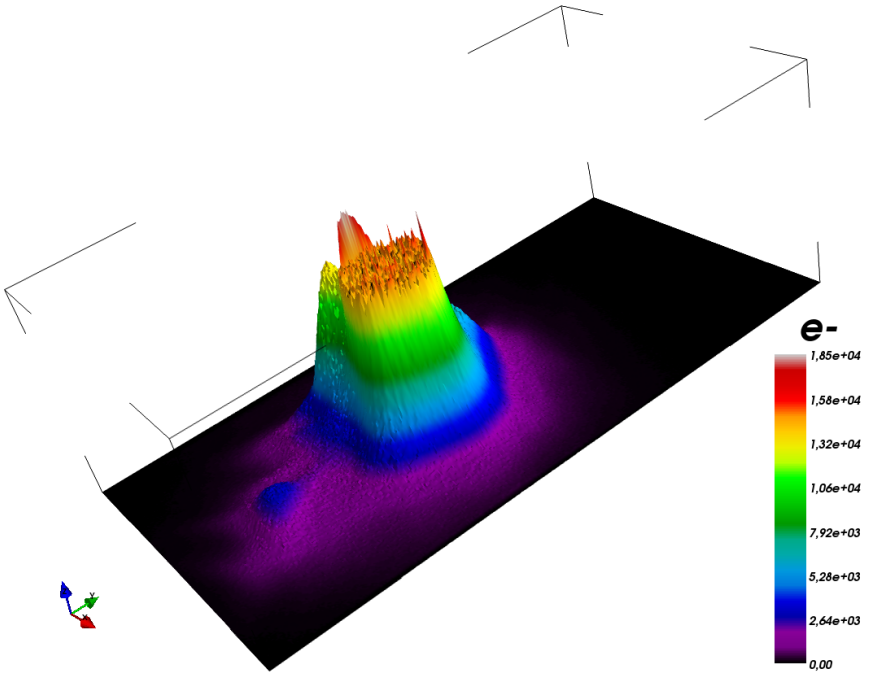

Figure A.18.: Three dimensional representation of measured intensity (counts) on the CCD camera from a focus spot in EFTEM mode. This image shows the same data as Fig. A.17e.

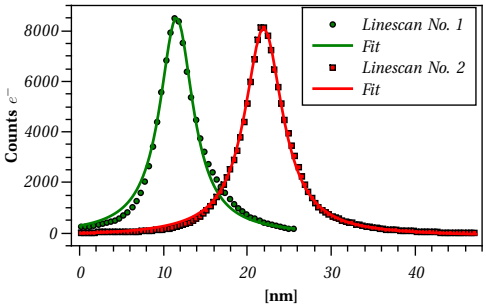

(a) Lin scan of Fig. A.16f.

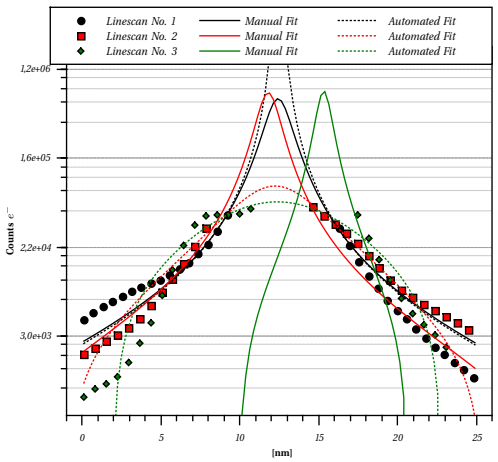

(b) Line scan of Fig. A.17e.

Figure A.19.: Line scans of focused spots. For results see Sec. 7.4.1 and Tables A.2 and A.4.

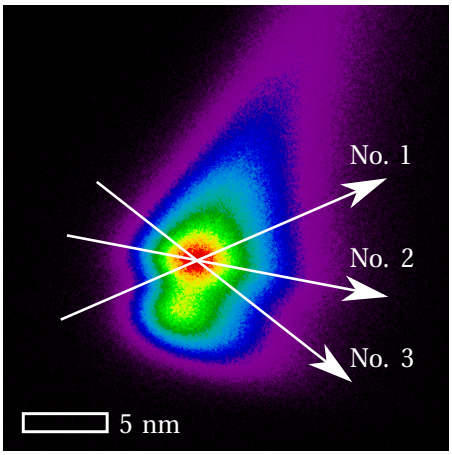

(a) Alignment used for all images.

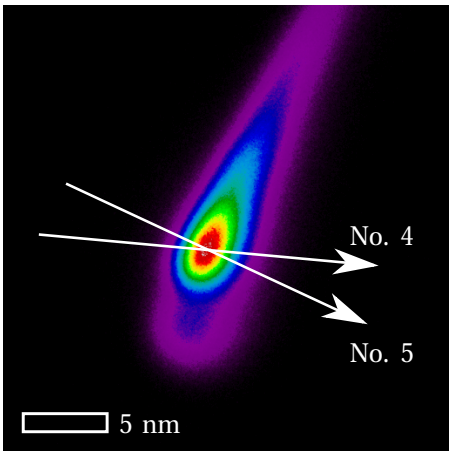

(b) Different Alignment.

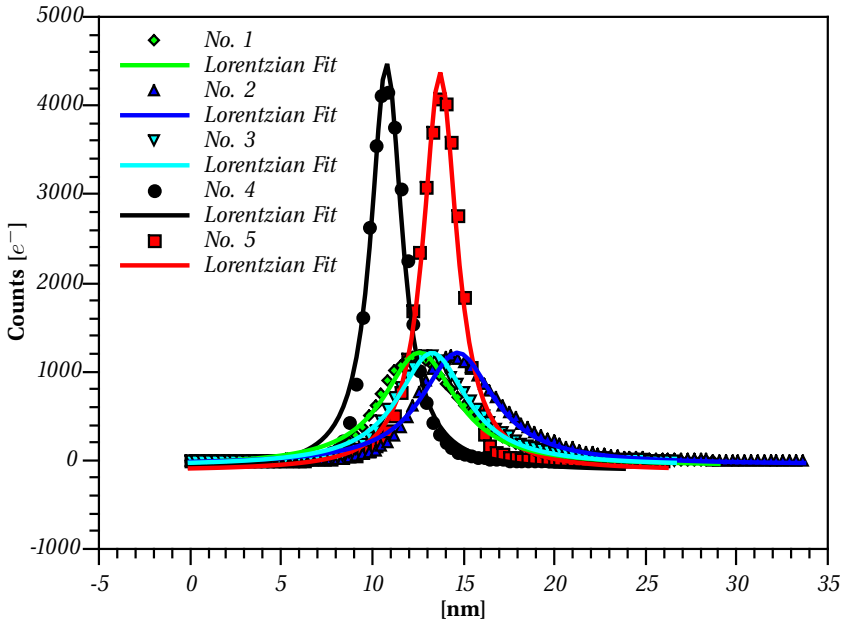

(c) Line scans across focused spot in TEM images as indicated by white arrows.

Figure A.20.: TEM image of focused spot acquired at 200 kV with standard 100 µm aperture with two different alignments.

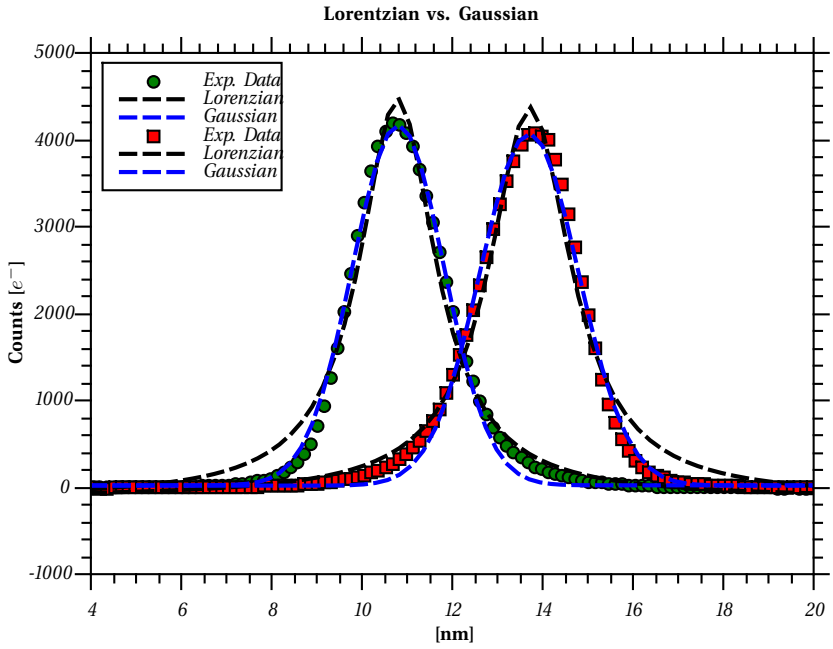

Figure A.21.: Comparison between Lorentzian and Gaussian fit of data shown in Fig. A.20b. Due to good acquisition conditions the Gaussian fits the data best, but data recorded with the twin aperture suffers distortions, which are conveniently covered by a Lorentzian.

A.9. Theory of Aberrations

Peter Tiemeijer has performed a series of wave aberration calculations based on the formalism described in Ref. [174]. Using the derivative of the wave aberration function one can calculate the displacement of rays in the image plane due to aberrations. For the problem encountered in Sec. 7.2 one would start with a number of ray positions describing the outline of two incident beams (two adjacent circles). These are then transformed using the derivative Δw of the wave aberration function

$$\Delta w(\omega) \propto C_{1,0}\omega + C_{0,1}\overline{\omega} + C_{0,2}\overline{\omega}^2 + \dots \tag{A.1}$$

$$\omega = \lambda \cdot q, \tag{A.2}$$

where ω is the complex scattering angle and $\overline{\omega}$ its complex conjugate, λ the electron wavelength and q the Fourier space coordinate of the aperture. $C_{1,0}$ is the defocus, $C_{0,1}$ the twofold astigmatism and $C_{0,2}$ is the threefold astigmatism.

Fig. A.22 shows the results of calculations regarding only threefold astigmatism and defocus. These results agree very well with the observations in Sec. 7.2.

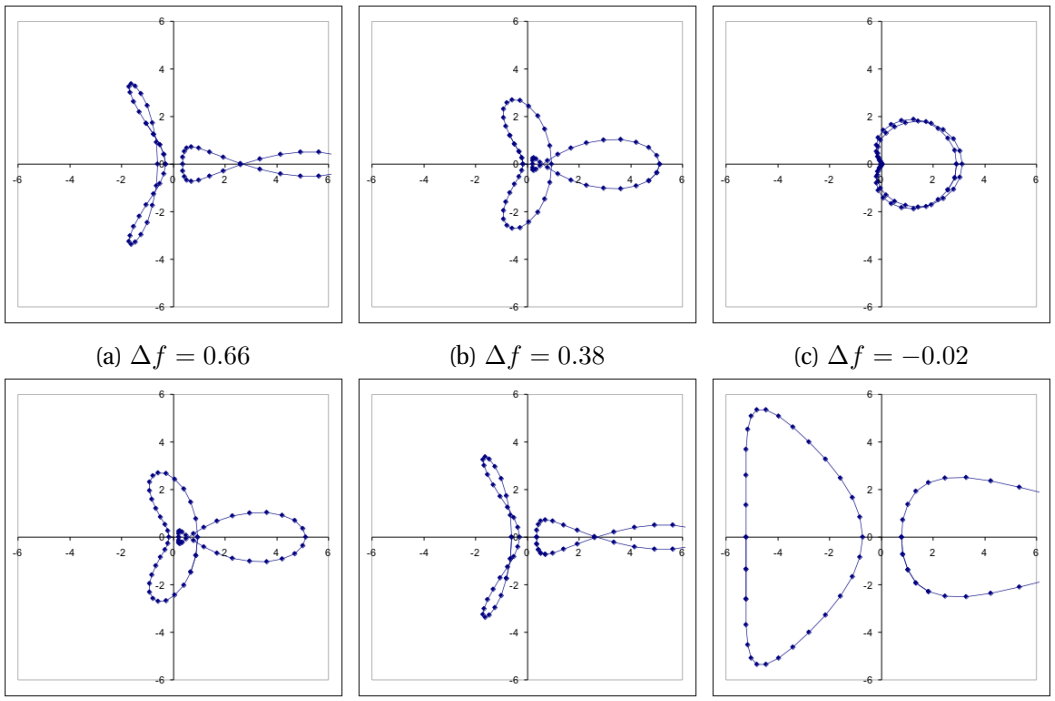

(a) $\Delta f = 0.66$ (b) $\Delta f = 0.38$ (c) $\Delta f = -0.02$

(d) $\Delta f = -0.38$ (e) $\Delta f = -0.66$ (f) $\Delta f = -1.5$

Figure A.22.: Dimensionless simulation by Peter Tiemeijer (FEI) of the cross over caused by a twin aperture based on experimentally encountered strong three-fold astigmatism.

Publications

1. A. Hasenkopf, “Entwicklung von Komponenten für einen ChiralSTEM-Modus”, Diploma Thesis (Universität Regensburg, 2008), https://em.ur.de/manuals/thesis/2008_Hasenkopf_Diplom.pdf

2. A. Hasenkopf and J. Zweck, “Development of components for a ChiralSTEM mode”, in 14^{th} European Microscopy Congress (2008), https://em.ur.de/wiki/media/uploads/posters/hasenkopf_a_2008_emc_aachen.pdf

3. A. Hasenkopf et al., “Investigation of the effect of ring electrodes on the electron beam in the TEM”, in Proceedings of IMC 2010, Rio de Janeiro, Brazil (2010), http://em.ur.de/media/uploads/posters/hasenkopf_a_2010_imc_riodejaneiro.pdf

4. A. Hasenkopf and J. Zweck, “A software tool for evaluating and enhancing the quality of EELS spectra for EMCD”, in Proceedings of the Microscopy Congress, Kiel, German (2011), https://www-elektronenmikroskopie.uni-regensburg.de/wiki/media/uploads/posters/hasenkopf_a_2011_mc_kiel.pdf

5. J. Zweck et al., “Quantitative calibration of a differential phase contrast detector for electric field measurement”, in EMC2012 Proceddings (2012), http://www.emc2012.org.uk/documents/Abstracts/Abstracts/EMC2012_0340.pdf

6. A. Pritschet et al., “Simulations of the Boersch phase plate EMCD experiment”, Ultramicroscopy, submitted (2012)

7. J. Zweck et al., “Probing electron density distributions on a 0.1 nm scale in GaN crystals by differential phase contrast”, Science, submitted (2013)

8. J. Zweck et al., “Charge density within unit cell of GaN images with sub-ngström resolution by differential phase contrast microscopy”, in Proceedings of MC 2013, Regensburg, Germany (2013)

9. A. Pritschet and J. Zweck, “Fabrication and investigation of electrostatic condenser twin aperture and holder therefor for EMCD experiments”, in Proceedings of MC 2013, Regensburg, Germany (2013)

Bibliography

[1] C. Hébert and P. Schattschneider, "A proposal for dichroic experiments in the electron microscope", Ultramicroscopy **96**, 463–468, 10.1016/S0304-3991(03)00108-6, (2003).

[2] L. Calmels and J. Rusz, "Momentum-resolved EELS and EMCD spectra from the atomic multiplet theory: Application to magnetite", Ultramicroscopy **110**, 1042 –1045, 10.1016/j.ultramic.2010.04.015, (2010).

[3] M. Stöger-Pollach, C. D. Treiber, G. P. Resch, D. A. Keays, and I. Ennen, "EMCD real space maps of Magnetospirillum magnetotacticum", Micron **42**, 456 –460, 10.1016/j.micron.2011.01.003, (2011).

[4] J. Verbeeck, H. Tian, and P. Schattschneider, "Production and application of electron vortex beams", Nature **467**, 301–304, 10.1038/nature09366 (2010).

[5] T. Matsumoto and A. Tonomura, "The phase constancy of electron waves traveling through Boersch's electrostatic phase plate", Ultramicroscopy **63**, 5–10, 10.1016/0304-3991(96)00033-2, (1996).

[6] P. Schattschneider, S. Rubino, C. Hébert, J. Rusz, J. Kunes, P. Novák, E. Carlino, M. Fabrizioli, G. Panaccione, and G. Rossi, "Detection of magnetic circular dichroism using a transmission electron microscope", Nature **441**, 486–488, 10.1038/nature04778 (2006).

[7] A. Pritschet, J. Rusz, and J. Zweck, "Simulations of the Boersch phase plate EMCD experiment", Ultramicroscopy, submitted (2012).

[8] S. Rubino, "Magnetic Circular Dichroism in the Transmission Electron Microscope", PhD thesis (TU Wien, 2007).

[9] B. Warot-Fonrose, F. Houdellier, M. Hÿtch, L. Calmels, V. Serin, and E. Snoeck, "Mapping inelastic intensities in diffraction patterns of magnetic samples using the energy spectrum imaging technique", Ultramicroscopy **108**, 393 –398, 10.1016/j.ultramic.2007.05.013, (2008).

[10] P. Schattschneider, C. Hébert, S. Rubino, M. Stöger-Pollach, J. Rusz, and P. Novák, "Magnetic circular dichroism in EELS: Towards 10nm resolution", Ultramicroscopy **108**, 433–438, 10.1016/j.ultramic.2007.07.002, (2008).

[11] P. Schattschneider, M. Stöger-Pollach, S. Rubino, M. Sperl, C. Hurm, J. Zweck, and J. Rusz, "Detection of magnetic circular dichroism on the two-nanometer scale", Phys. Rev. B **78**, 104413, 10.1103/PhysRevB.78.104413, (2008).

[12] J. Rusz, S. Rubino, and P. Schattschneider, "First-principles theory of chiral dichroism in electron microscopy applied to 3d ferromagnets", Physical Review Letters **B 75**, 214425, 10.1103/PhysRevB.75.214425, (2007).

[13]J. Verbeeck, C. Hébert, S. Rubino, P. Novák, J. Rusz, F. Houdellier, C. Gatel, and P. Schattschneider, "Optimal aperture sizes and positions for EMCD experiments", Ultramicroscopy **108**, 865–872, 10.1016/j.ultramic.2008.02.007, (2008).

[14]J. Rusz, O. Eriksson, P. Novák, and P. M. Oppeneer, "Sum rules for electron energy loss near edge spectra", Phys. Rev. B **76**, 060408, 10.1103/PhysRevB.76.060408, (2007).

[15]L. Calmels, F. Houdellier, B. Warot-Fonrose, C. Gatel, M. J. Hÿtch., V. Serin, E. Snoeck, and P. Schattschneider, "Experimental application of sum rules for electron energy loss magnetic chiral dichroism", Phys. Rev. B **76**, 060409, 10.1103/PhysRevB.76.060409, (2007).

[16]J. Rusz, H. Lidbaum, S. Rubino, B. Hjörvarsson, P. M. Oppeneer, O. Eriksson, and K. Leifer, "Influence of plural scattering on the quantitative determination of spin and orbital moments in electron magnetic chiral dichroism measurements", Phys. Rev. B **83**, 132402, 10.1103/PhysRevB.83.132402, (2011).

[17]J. Rusz, S. Rubino, O. Eriksson, P. M. Oppeneer, and K. Leifer, "Local electronic structure information contained in energy-filtered diffraction patterns", Phys. Rev. B **84**, 064444, 10.1103/PhysRevB.84.064444, (2011).

[18]H. Lidbaum, J. Rusz, A. Liebig, B. Hjörvarsson, P. M. Oppeneer, E. Coronel, O. Eriksson, and K. Leifer, "Quantitative Magnetic Information from Reciprocal Space Maps in Transmission Electron Microscopy", Phys. Rev. Lett. **102**, 037201, 10.1103/PhysRevLett.102.037201, (2009).

[19]P. Schattschneider, S. Rubino, M. Stoeger-Pollach, C. Hebert, J. Rusz, L. Calmels, and E. Snoeck, "Energy loss magnetic chiral dichroism: A new technique for the study of magnetic properties in the electron microscope (invited)", Journal of Applied Physics **103**, 07D931 –07D931–6, 10.1063/1.2836680 (2008).

[20]B. Warot-Fonrose, C. Gatel, L. Calmels, V. Serin, and P. Schattschneider, "Effect of spatial and energy distortions on energy-loss magnetic chiral dichroism measurements: Application to an iron thin film", Ultramicroscopy **110**, 1033 –1037, 10.1016/j.ultramic.2009.12.011, (2010).

[21]Z. H. Zhang, X. Wang, J. B. Xu, S. Muller, C. Ronning, and Q. Li, "Evidence of intrinsic ferromagnetism in individual dilute magnetic semiconducting nanostructures", Nature Nanotechnology **4**, 523 –527, 10.1038/nnano.2009.181, (2009).

[22]R. F. Klie, T. Yuan, M. Tanase, G. Yang, and Q. Ramasse, "Direct measurement of ferromagnetic ordering in biaxially strained $LaCoO_3$ thin films", Applied Physics Letters **96**, 082510 –082510–3, 10.1063/1.3336010 (2010).

[23]Z. H. Zhang, H. L. Tao, M. He, and Q. Li, "Origination of electron magnetic chiral dichroism in cobalt-doped ZnO dilute magnetic semiconductors", Scripta Materialia **65**, 367 –370, 10.1016/j.scriptamat.2011.05.013, (2011).

[24]J. Salafranca, J. Gazquez, N. Pérez, A. Labarta, S. T. Pantelides, S. J. Pennycook, X. Batlle, and M. Varela, "Surfactant Organic Molecules Restore Magnetism in Metal-Oxide Nanoparticle Surfaces", Nano Letters **12**, 2499 –2503, 10.1021/nl300665z, (2012).

[25]B. Loukya, X. Zhang, A. Gupta, and R. Datta, "Electron magnetic chiral dichroism in CrO_2 thin films using monochromatic probe illumination in a transmission electron microscope", Journal of Magnetism and Magnetic Materials **324**, 3754 –3761, 10.1016/j.jmmm.2012.06.012, (2012).

[26]J. Rusz, S. Muto, and K. Tatsumi, "New algorithm for efficient Bloch-waves calculations of orientation-sensitive ELNES", Ultramicroscopy **125**, 81 –88, 10.1016/j.ultramic.2012.09.009, (2013).

[27]S. Muto, K. Tatsumi, and J. Rusz, "Parameter-free extraction of EMCD from an energy-filtered diffraction datacube using multivariate curve resolution", Ultramicroscopy **125**, 89 –96, 10.1016/j.ultramic.2012.09.008, (2013).

[28]P. Schattschneider, *Linear and Chiral Dichroism in the Electron Microscope* (2012).

[29]Wikipedia, *Magneto-optic Kerr effect – Wikipedia, The Free Encyclopedia*, 2013, http://en.wikipedia.org/w/index.php?title=Magneto-optic_Kerr_effect&oldid=545053700.

[30]Z. Q. Qiu and S. D. Bader, "Surface magneto-optic Kerr effect", Review of Scientific Instruments **71**, 1243, 10.1063/1.1150496, (2000).

[31]C. Hurm, "Electron Magnetic Chiral Dichroism in a Transmission Electron Microscope", PhD thesis (U Regensburg, 2008).

[32]F. Schwabl, *Quantenmechanik*, 6th ed. (Springer, 2002).

[33]H. Lidbaum, "Transmission Electron Microscopy for Characterization of Structures, Interfaces and Magnetic Moments in Magnetic Thin Films and Multilayers", PhD thesis (Uppsala Universitet, 2009).

[34]A. Hasenkopf, "Entwicklung von Komponenten für einen ChiralSTEM-Modus", Diploma Thesis (Universität Regensburg, 2008), https://em.ur.de/manuals/thesis/2008_Hasenkopf_Diplom.pdf.

[35]M. Nelhiebel, N. Luchier, P. Schorsch, P. Schattschneider, and B. Jouffrey, "The mixed dynamic form factor for atomic core-level excitations in interferometric electron-energy-loss experiments", Philosophical Magazine Part B **79**, 941 –953, 10.1080/13642819908214851, (1999).

[36]J. Rusz, P. Novak, S. Rubino, C. Hebert, and P. Schattschneider, "Magnetic Circular Dichroism in Electron Microscopy", Acta Physica Polonica A **113**, 599 –604, http://przyrbwn.icm.edu.pl/APP/PDF/113/a113z1146.pdf (2008).

[37]P. Schattschneider, M. Nelhiebel, H. Souchay, and B. Jouffrey, "The physical significance of the mixed dynamic form factor", Micron **31**, 333–345, 10.1016/S0968-4328(99)00112-2, (2000).

[38]H. Lidbaum, J. Rusz, S. Rubino, A. Liebig, B. Hjörvarsson, P. M. Oppeneer, O. Eriksson, and K. Leifer, "Reciprocal and real space maps for EMCD experiments", Ultramicroscopy **110**, 1380 –1389, 10.1016/j.ultramic.2010.07.004, (2010).

[39]J. Verbeeck, C. Hébert, S. Rubino, P. Novák, J. Rusz, F. Houdellier, C. Gatel, and P. Schattschneider, "Optimal aperture sizes and positions for EMCD experiments", in 14^{th} European Microscopy Congress, Vol. 1 (2008), pp. 453–454.

[40]P. Schattschneider, J. Verbeeck, and A. Hamon, "Real space maps of atomic transitions", Ultramicroscopy **109**, 781 –787, 10.1016/j.ultramic.2009.01.016, (2009).

[41]P. Schattschneider, I. Ennen, M. Stöger-Pollach, J. Verbeeck, V. Mauchamp, and M. Jaouen, "Real space maps of magnetic moments on the atomic scale: Theory and feasibility", Ultramicroscopy **110**, 1038 –1041, 10.1016/j.ultramic.2009.11.020, (2010).

[42]L. Reimer, *Transmission Electron Microscopy* (Springer, 1984).

[43]M. Uchida and A. Tonomura, "Generation of electron beams carrying orbital angular momentum", Nature **464**, 737–739, 10.1038/nature08904 (2010).

[44]A. G. Peele, P. J. McMahon, D. Paterson, C. Q. Tran, A. P. Mancuso, K. A. Nugent, J. P. Hayes, E. Harvey, B. Lai, and I. McNulty, "Observation of an x-ray vortex", Opt. Lett. **27**, 1752–1754, 10.1364/OL.27.001752, (2002).

[45]Q. Zhan, "Properties of circularly polarized vortex beams", Opt. Lett. **31**, 867–869, 10.1364/OL.31.000867, (2006).

[46]L. Allen, M. W. Beijersbergen, R. J. C. Spreeuw, and J. P. Woerdman, "Orbital angular momentum of light and the transformation of Laguerre-Gaussian laser modes", Phys. Rev. A **45**, 8185 –8189, 10.1103/PhysRevA.45.8185, (1992).

[47]B. J. McMorran, A. Agrawal, I. M. Anderson, A. A. Herzing, H. J. Lezec, J. J. McClelland, and J. Unguris, "Electron Vortex Beams with High Quanta of Orbital Angular Momentum", Science **331**, 192–195, 10.1126/science.1198804 (2011).

[48]J. C. Idrobo and S. J. Pennycook, "Vortex beams for atomic resolution dichroism", Journal of Electron Microscopy **60**, 295–300, 10.1093/jmicro/dfr069 (2011).

[49]P. Schattschneider, M. Stöger-Pollach, S. Löffler, A. Steiger-Thirsfeld, J. Hell, and J. Verbeeck, "Sub-nanometer free electrons with topological charge", Ultramicroscopy, 21 –25, 10.1016/j.ultramic.2012.01.010, (2012).

[50]R. A. Herring, "A New Twist for Electron Beams", Science **331**, 155–156, 10.1126/science.1200643 (2011).

[51]S. Findlay, P. Schattschneider, and L. Allen, "Imaging using inelastically scattered electrons in CTEM and STEM geometry", Ultramicroscopy **108**, 58 –67, 10.1016/j.ultramic.2007.03.003, (2007).

[52]H. Boersch, "Über die Kontraste von Atomen im Elektronenmikroskop", Z. Naturforsch. **2a**, 615ff (1947).

[53]Wikipedia, *Waveplate – Wikipedia, The Free Encyclopedia*, 2013, http://en.wikipedia.org/w/index.php?title=Waveplate&oldid=541342905.

[54]E. Hecht, *Optics* (2001).

[55]D. B. Williams and C. B. Carter, *Transmission electron microscopy: A Textbook for Materials Science* (Springer, 1996).

[56]C. R. Burch and J. P. P. Stock, "Phase-Contrast Microscopy", Journal of Scientific Instruments **19**, 71, 10.1088/0950-7671/19/5/302, (1942).

[57]D. F. Parsons and H. M. Johnson, "Possibility of a phase contrast electron microscope", Appl. Opt. **11**, 2840–2843, 10.1364/AO.11.002840, (1972).

[58]T. Matsumoto, N. Osakabe, and A. Tonomura, "Phase-contrast electron microscope and phase plate therefor", pat. US 5814815 (Hitachi, 1998), http://www.google.com/patents/US5814815.

[59]K. Nagayama, "Another 60 years in electron microscopy: development of phase-plate electron microscopy and biological applications", Journal of Electron Microscopy **60**, S43–S62, 10.1093/jmicro/dfr037, (2011).

[60]C. J. Edgcombe and J. A. C. Bland, "A Phase Plate for Electron Microscopy using the Aharonov-Bohm effect", in 14^{th} European Microscopy Congress – Late Breaking Posters, P802 (2008).

[61]K. Schultheiß, "Entwicklung und Anwendung elektrostatischer Phasenplatten in der Transmissionselektronenmikroskopie", PhD thesis (Institut für Technologie, Karlsruhe, 2010), http://digbib.ubka.uni-karlsruhe.de/volltexte/documents/1296554.

[62]A. Walter, H. Muzik, H. Vieker, A. Turchanin, A. Beyer, A. Gölzhäuser, M. Lacher, S. Steltenkamp, S. Schmitz, P. Holik, W. Kühlbrandt, and D. Rhinow, "Practical aspects of Boersch phase contrast electron microscopy of biological specimens", Ultramicroscopy **116**, 62–72, 10.1016/j.ultramic.2012.03.009, (2012).

[63]R. Danev and K. Nagayama, "Complex Observation in Electron Microscopy: IV. Reconstruction of Complex Object Wave from Conventional and Half Plane Phase Plate Image Pair", Journal of the Physical Society of Japan **73**, 2718 –2724, 10.1143/JPSJ.73.2718, (2004).

[64]M. Dries, B. Gamm, S. Hettler, E. Müller, W. Send, D. Gerthsen, and A. Rosenauer, "A nanocrystalline Hilbert-phase plate for phase-contrast transmission electron microscopy of amorphous objects", in The Proceedings of EMC2012 (2012), http://www.emc2012.org.uk//documents/Abstracts/Abstracts/EMC2012_0106.pdf.

[65]K. Atsuzawa, N. Usuda, A. Nakazawa, M. Fukasawa, R. Danev, S. Sugitani, and K. Nagayama, "High-contrast imaging of plastic-embedded tissues by phase contrast electron microscopy", Journal of Electron Microscopy **58**, 35 –45, 10.1093/jmicro/dfp004, (2009).

[66]E. Majorovits, B. Barton, K. Schultheiß, F. Perez-Willard, D. Gerthsen, and R. R. Schröder, "Optimizing phase contrast in transmission electron microscopy with an electrostatic (Boersch) phase plate", Ultramicroscopy **107**, 213–226, 10.1016/j.ultramic.2006.07.006, (2007).

[67]J. Shiue, C.-S. Chang, S.-H. Huang, C.-H. Hsu, J.-S. Tsai, W.-H. Chang, Y.-M. Wu, Y.-C. Lin, P.-C. Kuo, Y.-S. Huang, Y. Hwu, J.-J. Kai, F.-G. Tseng, and F.-R. Chen, "Phase TEM for biological imaging utilizing a Boersch electrostatic phase plate: theory and practice", Journal of Electron Microscopy **58**, 137–145, 10.1093/jmicro/dfp006, (2009).

[68]J. Zach, "Phase plate, imaging method and electron microscope", pat. US7928379B2 (C. C. E. O. S. GmbH, 2011), http://www.google.com/patents/US7928379.

[69]N. Frindt, S. Hettler, M. Oster, B. Gamm, M. Dries, K. Schultheiss, D. Gerthsen, and R. Schröder, "Electrostatic Zach phase plate imaging with invertible phase contrast of frozen-hydrated biological samples", in Proceddings of EMC2012 (2012), http://www.emc2012.org.uk//documents/Abstracts/Abstracts/EMC2012_0382.pdf.

[70]S. Hettler, M. Dries, B. Gamm, K. Schultheiss, N. Frindt, R. Schröder, J. Zach, and D. Gerthsen, "Electrostatic Zach phase plates: optimization of properties and applications", Microscopy and Microanalysis **18**, 466 –467, 10.1017/S1431927612004187, (2012).

[71]R. R. Schröder, B. Barton, H. Rose, and G. Benner, "Contrast Enhancement by Anamorphotic Phase Plates in an Aberration Corrected TEM", Microscopy and Microanalysis **13**, 8 –9, 10.1017/S143192760708004X, (2007).

[72]H. H. Rose, "Future trends in aberration-corrected electron microscopy", Philosophical Transactions of the Royal Society A: Mathematical, Physical and Engineering Sciences **367**, 3809 –3823, 10.1098/rsta.2009.0062, (2009).

[73]N. Frindt, K. Schultheiss, B. Gamm, M. Dries, J. Zach, D. Gerthsen, and R. Schröder, "The Way to an Ideal Matter-free Zernike and Hilbert TEM Phase Plate: Anamorphotic Design and First Experimental Verification in Isotropic Optics", Microscopy and Microanalysis **16**, 518 –519, 10.1017/S1431927610056436, (2010).

[74]Excillum AB, *Phase contrast image of a wasp*, 2011, http://www.mynewsdesk.com/view/image/phase-contrast-image-of-a-wasp-83186.

[75]V. S. Machavariani, "Quarter-Wave Plate in Near-Edge Soft X-Ray Region Based on the Total External Reflection Principle", Phys. Rev. Lett. **80**, 1541 –1543, 10.1103/PhysRevLett.80.1541, (1998).

[76]S. Pizzini, M. Bonfim, F. Baudelet, H. Tolentino, A. S. Miguel, K. Mackay, C. Malgrange, M. Hagelstein, and A. Fontaine, "Quarter-Wave Plates and X-ray Magnetic Circular Dichroism on ID24 at the ESRF", Journal of Synchrotron Radiation **5**, 1298 –1303, 10.1107/S0909049598004154, (1998).

[77]J. Chapman, R. Ploessl, and D. Donnet, "Differential phase contrast microscopy of magnetic materials", Ultramicroscopy **47**, 331 –338, 10.1016/0304-3991(92)90162-D, (1992).

[78]T. Uhlig and J. Zweck, "Recording of single-particle hysteresis loops with differential phase contrast microscopy", Ultramicroscopy **99**, 137 –142, 10.1016/j.ultramic.2003.12.002, (2004).

[79]M. Lohr, R. Schregle, M. Jetter, C. Wächter, T. Wunderer, F. Scholz, and J. Zweck, "Differential phase contrast 2.0 – Opening new "fields" for an established technique", Ultramicroscopy **117**, 7 –14, 10.1016/j.ultramic.2012.03.020, (2012).

[80]J. Zweck, S. Lazar, B. Freitag, M. Lohr, B. Bauer, J. Thalmair, A. Pritschet, and M. Vogel, "Probing electron density distributions on a 0.1 nm scale in GaN crystals by differential phase contrast", Science, submitted (2013).

[81]M. Lohr, "Quantitative Bestimmung innerer elektrischer Felder mit Hilfe von Differentieller Phasenkontrastmikroskopie", PhD thesis (Universität Regensburg, 2013).

[82]Wikipedia, *Partial differential equation – Wikipedia, The Free Encyclopedia*, 2013, http://en.wikipedia.org/w/index.php?title=Partial_differential_equation&oldid=542987847.

[83]P. Solin, *Partial Differential Equations and the Finite Element Method* (Wiley, 2006).

[84]A. O'Brien, *A Simple Introduction to Finite Element Analysis*, http://einstein.drexel.edu/~bob/TermPapers/OBrien_QuantumPaper.pdf.

[85]C. A. Felippa, "A compendium of FEM integration formulas for symbolic work", Engineering Computations **21**, 867–890, 10.1108/02644400410554362, (2004).

[86]C. Geuzaine and J.-F. Remacle, "Gmsh: a three-dimensional finite element mesh generator with built-in pre- and post-processing facilities", Int. J. Numer. Meth. Engng **79**, 1309–1331, 10.1002/nme.2579, (2009).

[87]K. Erleben, *Finite Element Method – A short Introduction to Principles and Ideas*, 2010, http://image.diku.dk/kenny/download/vriphys10_course/fem.pdf.

[88]J. E. Guyer, D. Wheeler, and J. A. Warren, "FiPy: Partial Differential Equations with Python", Computing in Science & Engineering **11**, 6 –15, 10.1109/MCSE.2009.52, (2009).

[89]E. W. Weisstein, *Green's Function, From MathWorld – A Wolfram Web Resource*, 2004, http://mathworld.wolfram.com/GreensFunction.html.

[90]Wikipedia, *Fourier optics – Wikipedia, The Free Encyclopedia*, 2013, http://en.wikipedia.org/w/index.php?title=Fourier_optics&oldid=540442149.

[91]J. C. H. Spence, *High-Resolution Electron Microscopy*, 3rd ed. (Oxford University Press, 2003).

[92]Wikipedia, *Convolution — Wikipedia, The Free Encyclopedia*, 2013, http://en.wikipedia.org/w/index.php?title=Convolution&oldid=554564678.

[93]J. W. Goodman, *Introduction to Fourier Optics*, 3rd (Roberts and Company Publishers, 2004).

[94]S. J. Penyncook and P. D. Nellist, *Scanning Transmission Electron Microscopy, Imaging and Analysis* (2011), 10.1007/978-1-4419-7200-2.

[95]D. Kammler, *A First Course in Fourier Analysis* (2000).

[96]N. Baddour, *2D Fourier Transforms in Polar Coordinates* (2010), http://issuu.com/nbaddour/docs/2d-fourier-polar-chapter.

[97]M. F. Guasti and M. D. L. C. Heredia, "Diffraction Pattern of a Circle/square Aperture", Journal of Modern Optics **40**, 1073 –1080, 10.1080/09500349314551141, (1993).

[98]Bergmann and Schaefer, eds., *Optik – Wellen- und Teilchenoptik* (de Gruyter, 2004).

[99]Wikipedia, *Fourier transform — Wikipedia, The Free Encyclopedia*, 2013, http://en.wikipedia.org/w/index.php?title=Fourier_transform&oldid=550845886.

[100]A. Hasenkopf and J. Zweck, "Development of components for a ChiralSTEM mode", in 14^{th} European Microscopy Congress (2008), https://em.ur.de/wiki/media/uploads/posters/hasenkopf_a_2008_emc_aachen.pdf.

[101]P. L. Fejes, "Approximations for the calculation of high-resolution electron-microscope images of thin films", Acta Crystallographica **A33**, 109 –113, 10.1107/S0567739477000230, (1977).

[102] I. de Jong, *Pyro - Python Remote Objects*, 2013, http://pythonhosted.org/Pyro4/.

[103] Wikipedia, *Monte Carlo method – Wikipedia, The Free Encyclopedia*, 2013, http://en.wikipedia.org/w/index.php?title=Monte_Carlo_method&oldid=545034153.

[104] D. Drouin, A. R. Couture, D. Joly, X. Tastet, V. Aimez, and R. Gauvin, "CASINO V2.42 – A Fast and Easy-to-use Modeling Tool for Scanning Electron Microscopy and Microanalysis Users", Scanning **29**, 92 –101, 10.1002/sca.20000 (2007).

[105] P. Hovington, D. Drouin, and R. Gauvin, "CASINO: A new monte carlo code in C language for electron beam interaction – part I: Description of the program", Scanning **19**, 1 –14, 10.1002/sca.4950190101, (1997).

[106] D. Drouin, P. Hovington, and R. Gauvin, "CASINO: A new monte carlo code in C language for electron beam interactions – part II: Tabulated values of the mott cross section", Scanning **19**, 20 –28, 10.1002/sca.4950190103 (1997).

[107] P. Hovington, D. Drouin, R. Gauvin, D. C. Joy, and N. Evans, "CASINO: A new monte Carlo code in C language for electron beam interactions – part III: Stopping power at low energies", Scanning **19**, 29 –35, 10.1002/sca.4950190104 (1997).

[108] D. Drouin, *monte CArlo SImulation of electroN trajectory in sOlids*, 2011, http://www.gel.usherbrooke.ca/casino/.

[109] Z. Czyzewski, D. O. MacCallum, A. Romig, and D. C. Joy, "Calculations of Mott scattering cross section", Journal of Applied Physics **68**, 3066 –3072, 10.1063/1.346400 (1990).

[110] N. F. Mott and H. S. W. Massey, "The theory of atomic collisions", The theory of atomic collisions, by Mott, NF; Massey, Harrie Stewart Wilson. Oxford, Clarendon Press, 1949. (1949).

[111] P. Schattschneider and W. S. M. Werner, "Coherence in electron energy loss spectrometry", Journal of Electron Spectroscopy and Related Phenomena **143**, 81–95, 10.1016/j.elspec.2004.09.029, (2005).

[112] K. Leifer, S. Rubino, J. Rusz, H. Lidbaum, B. Hjörvarsson, P. Oppeneer, and O. Eriksson, "Reciprocal space signals arising from interference of core-loss electrons in the EMCD geometry", in Proceedings of the MC2011 (2011).

[113] M. Knoll and E. Ruska, "Das Elektronenmikroskop", Zeitschrift **78**, 318 –339, 10.1007/BF01342199, (1932).

[114] A. Prebus and J. Hillier, "THE CONSTRUCTION OF A MAGNETIC ELECTRON MICROSCOPE OF HIGH RESOLVING POWER", Canadian Journal of Research **17a**, 49–65, 10.1139/cjr39a-004, (1939).

[115] L. Marton, "A New Electron Microscope", Physical Review **58**, 57 –60, 10.1103/PhysRev.58.57, (1940).

[116] L. Reimer and G. Pfefferkorn, *Rasterelektronenmikroskopie*, 2nd ed. (Springer, 1977).

[117] *Tecnai on-line help manual – Working with a FEG*, FEI (2002), https://em.ur.de/manuals/tecnai/user_manual/FEG_A4.pdf.

[118] *Tecnai on-line help manual – Alignments*, FEI (2002), https://em.ur.de/manuals/tecnai/user_manual/Align_F2030_A4.pdf.

[119] A. Crewe, M. Isaacson, and D. Johnson, "A Simple Scanning Electron Microscope", Review of Scientific Instruments **40**, 241–246, 10.1063/1.1683910 (1969).

[120] H. Voges and G. Ruthemann, "Steigerung des Auflösungsvermögens der magnetischen Halbkreismethode zur Geschwindigkeitsanalyse von Kathodenstrahlen", Zeits. für Physik **114**, 709–718 (1939).

[121] J. Hillier, "On microanalysis by electrons", Phys. Rev. **64**, 318 (1943).

[122] J. Hillier and R. F. Baker, "Microanalysis by means of electrons", Journal of Applied Physics **15**, 663 (1944).

[123] J. Hyun, *Fast simultaneous acquisition of low- and core-loss regions in the EELS spectrum from catalyst particles containing the heavy metals Au and Pd using the GIF Quantum*, tech. rep. (Gatan, 2011), http://www.gatan.com/products/analytical_tem/products/gif_quantum.php.

[124] Wikipedia, *Energy-dispersive X-ray spectroscopy – Wikipedia, The Free Encyclopedia*, 2013, http://en.wikipedia.org/w/index.php?title=Energy-dispersive_X-ray_spectroscopy&oldid=540439898.

[125] J. Goldstein, *Scanning Electron Microscopy and X-Ray Microanalysis* (2012).

[126] B. Corporation, ed., *Functional Principle of Silicon Drift Chamber*, http://www.bruker.com/en/products/x-ray-diffraction-and-elemental-analysis/components/x-ray-components/x-ray-detectors/xflashr-sd/sdd-functional-principle.html.

[127] L. Strüder, N. Meidinger, D. Stotter, J. Kemmer, P. Lechner, P. Leutenegger, H. Soltau, F. Eggert, M. Rohde, and T. Schulein, "High-Resolution X-ray Spectroscopy Close to Room Temperature", Microscopy and Microanalysis **4**, 622 –631, 10.1017/S1431927698980606, (1998).

[128] E. Gatti and P. Rehak, "Semiconductor drift chamber – An application of a novel charge transport scheme", Nuclear Instruments and Methods in Physics Research **225**, 608 –614, 10.1016/0167-5087(84)90113-3, (1984).

[129] *STATE-OF-THE-ART SILICON DETECTORS FOR X-RAY SPECTROSCOPY*, Denver X-ray Conferences, Vol. 47 (2004), http://www.icdd.com/resources/axa/VOL47/V47_06.pdf.

[130] *SILICON DRIFT DETECTORS FOR HIGH RESOLUTION, HIGH COUNT RATE X-RAY SPECTROSCOPY AT ROOM TEMPERATURE*, Denver X-ray Conferences, Vol. 47 (2004), pp. 53 – 58, http://www.icdd.com/resources/axa/VOL47/V47_07.pdf.

[131] N. H. Dekkers and H. D. Long, "Differential phase contrast in a STEM", Optik **41**, 452 –456 (1974).

[132] H. Rose, "Phase-contrast in scanning transmission electron microscopy", Optik **39**, 416 –436 (1974).

[133] H. Rose, "Nonstandard imaging methods in electron microscopy", Ultramicroscopy **2**, 251 – 267, 10.1016/S0304-3991(76)91538-2, (1977).

[134] J. Zweck, R. Schregle, A. Hasenkopf, and M. Lohr, "Quantitative calibration of a differential phase contrast detector for electric field measurement", in EMC2012 Proceddings (2012), http://www.emc2012.org.uk/documents/Abstracts/Abstracts/EMC2012_0340.pdf.

[135]T. Uhlig, "Differentielle Phasenkontrastmikroskopie an magnetischen Ringstrukturen", PhD thesis (Universität Regensburg, 2004).

[136]J. Cowley, "Adjustment of a STEM instrument by use of shadow images", Ultramicroscopy **4**, 413 –418, 10.1016/S0304-3991(79)80018-2, (1979).

[137]E. James and N. Browning, "Practical aspects of atomic resolution imaging and analysis in STEM", Ultramicroscopy **78**, 125 –139, 10.1016/S0304-3991(99)00018-2, (1999).

[138]R. F. W. Pease, "Electron beam lithography", Contemporary Physics **22**, 265–290, 10.1080/00107518108231531, (1981).

[139]C. Vieu, F. Carcenac, A. Pépin, Y. Chen, M. Mejias, A. Lebib, L. Manin-Ferlazzo, L. Couraud, and H. Launois, "Electron beam lithography: resolution limits and applications", Applied Surface Science **164**, 111 –117, 10.1016/S0169-4332(00)00352-4, (2000).

[140]G. H. Bernstein and D. A. Hill, "On the attainment of optimum developer parameters for PMMA resist", Superlattices and Microstructures **11**, 237 –240, 10.1016/0749-6036(92)90260-C, (1992).

[141]V. Dixit, H. Davis, and M. Clark, "Wire Bonding Considerations", Solid State Technology **15**, http://www.electroiq.com/articles/ap/print/volume-15/issue-7/features/the-back-end-process/wire-bonding-considerations.html (2006).

[142]T. Haug, "Simultaneous Transport Measurements and Highly Resolved Domain Observation of Ferromagnetic Nanostructures", PhD thesis (Universität Regensburg, 2006).

[143]D. Sigg, *Printed Circuit Boards for Ultra High Vacuum*, tech. rep. LIGO-T060280-00 - D (California Institute of Technology, 2006), http://ific.uv.es/elec/files/PCB-UHV.pdf.

[144]N. Kanopoulos, N. Vasanthavada, and R. L. Baker, "Design of an image edge detection filter using the Sobel operator", Solid-State Circuits, IEEE Journal of **23**, 358 –367, 10.1109/4.996 (1988).

[145]Wikipedia, *Sobel operator – Wikipedia, The Free Encyclopedia*, 2013, http://en.wikipedia.org/w/index.php?title=Sobel_operator&oldid=543128275.

[146]R. Schregle, "Kalibrierung eines DPC-Detektors mit Hilfe eines speziell erstellten Probenhalters", Diploma thesis (Universität Regensburg, 2011), https://em.ur.de/manuals/thesis/2011_Schregle_Diplom.pdf.

[147]*Glanzgoldplattierbad 750 (SN, SC, SI, SCI, FeIn)*, tech. rep. (WIELAND Edelmetalle GmbH).

[148]K. G. Fertitta, A. L. Holmes, J. G. Neff, F. J. Ciuba, and R. D. Dupuis, "High quality GaN heteroepitaxial films grown by metalorganic chemical vapor deposition", Applied Physics Letters **65**, 1823 –1825, 10.1063/1.112855 (1994).

[149]L. Wang, X. Liu, Y. Zan, J. Wang, D. Wang, D. cheng Lu, and Z. Wang, "Wurtzite GaN epitaxial growth on a Si(001) substrate using gamma-Al_2O_3 as an intermediate layer", Applied Physics Letters **72**, 109 –111, 10.1063/1.120660, (1998).

[150]Y. Huang, D. J. H. Cockayne, C. Marsh, J. M. Titchmarsh, and A. K. Petford-Long, "Self-organized amorphous material in silicon (001) by focused ion beam (FIB) system", Applied Surface Science **252**, 1954 –1958, 10.1016/j.apsusc.2005.03.175, (2005).

[151]A. Harsanyi, *Glanzgoldplattierbad 750*, Wieland Edelmetalle (Wieland Edelmetalle, 2007), http://www.wieland-edelmetalle.de/uploads/tx_pxwldownloads/wdt_ind_Glanzgoldplattierbaeder-750S_eng.pdf.

[152]W. J. Basirun and D. Pletcher, "Studies of platinum electroplating baths Part VI: Influence of some experimental parameters on deposit quality", Journal of Applied Electrochemistry **28**, 167 –172, http://www.ingentaconnect.com/content/klu/jach/1997/00000028/00000002/00172007 (1997).

[153]Y. Wu, A. Suzuki, H. Murakami, and S. Kuroda, "Characterization of Electroplated Platinum-Iridium Alloys on the Nickel-Base Single Crystal Superalloy", Materials Transactions **46**, 2176 –2179, http://www.jim.or.jp/journal/e/46/10/2176.html (2005).

[154]C. Sill, "Elektronenstrahlinduzierte in-situ Abscheidung von metallischen und magnetischen Nanostrukturen", Diploma thesis (Universität Regensburg, 2009), https://em.ur.de/manuals/thesis/2009_Sill_Diplom.pdf.

[155]O. Krivanek and P. Mooney, "Applications of slow-scan CCD cameras in transmission electron microscopy", Ultramicroscopy **49**, 95 –108, 10.1016/0304-3991(93)90216-K, (1993).

[156]Wikipedia, *Cauchy distribution – Wikipedia, The Free Encyclopedia*, 2013, http://en.wikipedia.org/w/index.php?title=Cauchy_distribution&oldid=545946020.

[157]A. Papoulis, *Probability, Random Variables, and Stochastic Processes*, 2nd ed. (1984).

[158]M. R. Spiegel, *Theory and Problems of Probability and Statistics* (1992).

[159]E. W. Weisstein, *Cauchy Distribution, From MathWorld – A Wolfram Web Resource.* 2005, http://mathworld.wolfram.com/CauchyDistribution.html.

[160]J. Hren, "Barriers of AEM: contamination and etchin", in B. Jouffrey and C. Colliex, *Electron Microscopy* (1994).

[161]M. Tanaka, M. Shimojo, K. Mitsuishi, and K. Furuya, "The size dependence of the nano-dots formed by electron-beam-induced deposition on the partial pressure of the precursor", Applied Physics A: Materials Science & Processing, 10.1007/s00339-003-2394-z (2004).

[162]N. Silvis-Cividjian, C. W. Hagen, and P. Kruit, "Spatial resolution limits in electron-beam-induced deposition", Journal Of Applied Physics **98**, 10.1063/1.2085307 (2005).

[163]M. Takeguchi, M. Shimojo, R. Che, and K. Furuya, "Fabrication of a nano-magnet on a piezo-driven tip in a TEM sample holder", Journal of Materials Science, 10.1007/s10853-006-7825-8 (2006).

[164]M. Gavagnin, H. D. Wanzenboeck, D. Belić, and E. Bertagnolli, "Synthesis of Individually Tuned Nanomagnets for Nanomagnet Logic by Direct Write Focused Electron Beam Induced Deposition", ACS Nano **7**, 777–784, 10.1021/nn305079a, (2013).

[165]R. Grothausmann, "In-Situ Elektronenstrahldeposition von Leiterbahnen im Transmissionselektronenmikroskop", Diploma thesis (Universität Regensburg, 2007).

[166]M. G. Lassiter, "Electron Beam Induced Etching", PhD thesis (University of Tennessee, Knoxville, 2009), http://trace.tennessee.edu/cgi/viewcontent.cgi?article=1089&context=utk_graddiss.

[167] M. G. Lassiter and P. D. Rack, "Nanoscale electron beam induced etching: a continuum model that correlates the etch profile to the experimental parameters", Nanotechnology **19**, 455306, 10.1088/0957-4484/19/45/455306, (2008).

[168] S. J. Randolph, J. D. Fowlkes, and P. D. Rack, "Focused, Nanoscale Electron-Beam-Induced Deposition and Etching", Critical Reviews in Solid State and Materials Sciences **31**, 55 –89, 10.1080/10408430600930438, (2006).

[169] A. Ganczarczyk, M. Geller, and A. Lorke, "XeF_2 gas-assisted focused-electron-beam-induced etching of GaAs with 30 nm resolution", Nanotechnology **22**, 045301, 10.1088/0957-4484/22/4/045301, (2011).

[170] G. Love, V. Scott, N. Dennis, and L. Laurenson, "Sources of contaminants in electron optical equipment", Scanning **4**, 10.1002/sca.4950040105 (1981).

[171] A. C. F. Hoole, M. E. Welland, and A. N. Broers, "Negative PMMA as a high-resolution resist – the limits and possibilities", Semicond. Sci. Technol. **12**, 10.1088/0268-1242/12/9/017 (1997).

[172] M. Heumann, "Elektronenholografie an magnetischen Nanostrukturen", PhD thesis (Universität Regensburg, 2005).

[173] A. Hasenkopf and J. Zweck, "A software tool for evaluating and enhancing the quality of EELS spectra for EMCD", in Proceedings of the Microscopy Congress, Kiel, German (2011), https://www-elektronenmikroskopie.uni-regensburg.de/wiki/media/uploads/posters/hasenkopf_a_2011_mc_kiel.pdf.

[174] S. Uhlemann and M. Haider, "Residual wave aberrations in the first spherical aberration corrected transmission electron microscope", Ultramicroscopy **72**, 109 –119, 10.1016/S0304-3991(97)00102-2, (1998).

[175] A. Hasenkopf, J. Thalmair, M. Lohr, and J. Zweck, "Investigation of the effect of ring electrodes on the electron beam in the TEM", in Proceedings of IMC 2010, Rio de Janeiro, Brazil (2010), http://em.ur.de/media/uploads/posters/hasenkopf_a_2010_imc_riodejaneiro.pdf.

[176] J. Zweck, S. Lazar, B. Freitag, M. C. S. Vogel, C. K. A. Mewes, M. Lohr, B. Bauer, J. Thalmair, and A. Pritschet, "Charge density within unit cell of GaN images with sub-ngström resolution by differential phase contrast microscopy", in Proceedings of MC 2013, Regensburg, Germany (2013).

[177] A. Pritschet and J. Zweck, "Fabrication and investigation of electrostatic condenser twin aperture and holder therefor for EMCD experiments", in Proceedings of MC 2013, Regensburg, Germany (2013).

List of Figures

2.1. Schematic setup for the intrinsic method 4
2.2. Schematic setup for vortex beam method 6
2.3. Schematic setups for twin aperture EMCD experiments 7

3.1. Schematics of different phase plates 10
3.2. Anamorphotic phase plate 12
3.3. Phase contrast image of a wasp 13
3.4. Schematics of twin aperture designs 14

4.1. Simple boundary conditions 17
4.2. Cell shapes 17
4.3. Shape function 19
4.4. Solution of Laplace equation 22
4.5. Potential barrier 24
4.6. Boersch phase plate: Phase shift 27
4.7. Boersch phase plate: Fit parameters 27
4.8. Twin aperture: Phase shift 30
4.9. Twin aperture: Fit parameters 30
4.10. Phase shift for the different designs `twin_ap_2D_Xi` 32
4.11. Twin aperture variations 34
4.12. Trapped electrons in twin aperture 36
4.13. Phase shift by twin aperture with charging effects 36

5.1. Ray diagram: cross over of wave 40
5.2. Definition of convergence and incidence angles 42
5.3. Analytical calculation without phase shifts 44
5.4. Analytical simulation with phase shift $\pi/2$ 44
5.5. Line scans 44
5.6. Linear translation in polar coordinates 47
5.7. Numerical wave function 49
5.8. Comparison between analytical and numerical expressions 49
5.9. Phase fronts of incident waves 51
5.10. Line scans 51
5.11. Numerical calculation with potential reversal 53
5.12. Line scans: Effect of aberrations 55
5.13. Line scans comparing all three investigated cases 55
5.14. Numerical calculation with aberrations and potential reversal 57

5.15. Line scan . . . 57
5.16. Electron penetration depth in platinum at 200 kV . . . 59
5.17. Electron penetration depth . . . 59
5.18. Propagation plot of analytical model . . . 61
5.19. Simulated diffraction patterns by J. Rusz . . . 63

6.1. Schematics of Tecnai F30 lens systems . . . 67
6.2. Schematics of GIF Tridiem . . . 67
6.3. Schematic of SDD . . . 68
6.4. Working principle of DPC . . . 69
6.5. Ray diagram illustrating underfocus . . . 70
6.6. Formation of shadow image . . . 72
6.7. TEM images: shadow image . . . 72
6.8. Twin aperture production . . . 74
6.9. SEM images: twin aperture . . . 75
6.10. Wire bonding problem . . . 76
6.11. Aperture holder . . . 77

7.1. TEM image with contour of twin aperture . . . 80
7.2. Ray diagram: CBED pattern . . . 81
7.3. TEM image of CBED pattern . . . 81
7.4. Convergence angle from CBED pattern . . . 81
7.5. Focal series in TEM µProbe mode . . . 83
7.6. Statistical evaluation of a DPC measurement . . . 84
7.7. DPC time series (radial component only) . . . 85
7.8. DPC time series . . . 85
7.9. Thought experiment: twin aperture — FET . . . 87
7.10. Resistance measurement . . . 88
7.11. TEM lamella cut from twin aperture . . . 90
7.12. EDX line scan on lamella . . . 90
7.13. Redeposition during FIB milling . . . 91
7.14. EDX elemental map . . . 92
7.15. EDX elemental map . . . 92
7.16. Focused spot on CCD camera at 200 kV . . . 96
7.17. Focused spot on CCD camera at 300 kV . . . 96
7.18. Focused spot on CCD camera at 300 kV; standard aperture . . . 96
7.19. Contamination on SiN membrane in TEM . . . 99
7.20. Contamination spot/hole analysis in TEM image . . . 100

A.1. Aperture holder . . . 104
A.2. PCBs . . . 105
A.3. Phase shift for charges in twin aperture . . . 108
A.4. Phase difference: analytical vs. numerical model . . . 108
A.5. Comparison between analytical and numerical expressions . . . 109

A.6. Wave function for model `twin_ap_2D_X5` 109
A.7. Analytical vs. numerical model – intensity 110
A.8. Phase fronts of incident waves 110
A.9. Line scans: intensity for analytical and numerical model 111
A.10. Line scans 111
A.11. (Non-)Mangetic signal for different thicknesses. 112
A.12. DPC time series 113
A.13. DPC time series – other measurements 113
A.14. BF signal and EDX elemental maps 114
A.15. BF signal and EDX elemental maps 114
A.16. Focal series with twin aperture 116
A.17. Focal series with twin aperture 117
A.18. Surf plot of overexposed image 118
A.19. Line scans across focused spot in overexposed image 118
A.20. TEM image of focused spot with standard aperture 119
A.21. Comparison between Lorentzian and Gaussian 120
A.22. Effects of aberration on probe formation. Calculation by P. Tiemeijer 121

Acknowledgment

I would like to acknowledge my former collegues *Christian Dietrich* for the introductions given in the clean room environment and *Christian Hurm* for the introductions to EMCD experiments.

For their very helpful remarks and calculations I am very thankful to *Jan Rusz* and *Peter Tiemeijer*.

I also acknowledge the efforts by the customer service department at FEI to locate and fix truly weird errors on the microscope.

Finally I'd like to thank the work group of *Josef Zweck* and the chair's staff for their helpful remarks and loan collection during the construction of the aperture holder and repairs of the microscope. Special thanks goes to *Walter Wendt* who managed to perform said construction within specified accuracies.

Assertion — Eidesstattliche Erklärung

Ich erkläre hiermit an Eides statt, dass ich die vorliegende Arbeit ohne unzulässige Hilfe Dritter und ohne Benutzung anderer als der angegebenen Hilfsmittel angefertigt habe; die aus anderen Quellen direkt oder indirekt übernommenen Daten und Konzepte sind unter Angabe des Literaturzitats gekennzeichnet.

Bei der Auswahl und Auswertung folgenden Materials haben mir die nachstehend aufgeführten Personen in der jeweils beschriebenen Weise entgeltlich/unentgeltlich geholfen:

- Jan Rusz, Ångström Universiteit, Uppsala, Schweden (siehe Abschnitt 5.4, unentgeltlich)
- Peter Tiemeijer, FEI, Eindhoven, Niederlande (siehe Anhang A.9, unentgeltlich)

Weitere Personen waren an der inhaltlich-materiellen Herstellung der vorliegenden Arbeit nicht beteiligt. Insbesondere habe ich hierfür nicht die entgeltliche Hilfe eines Promotionsberaters oder anderer Personen in Anspruch genommen. Niemand hat von mir weder unmittelbar noch mittelbar geldwerte Leistungen für Arbeiten erhalten, die im Zusammenhang mit dem Inhalt der vorgelegten Dissertation stehen.

Die Arbeit wurde bisher weder im In- noch im Ausland in gleicher oder ähnlicher Form einer anderen Prüfungsbehörde vorgelegt.

Lappersdorf, 25.06.2013

(Ort, Datum)	(Unterschrift)